12-2013

Study on Electromagnetic Scattering of Cylinders Buried in a Half Space with Random Rough Surfaces of Finite/Infinite Length

Yueyang Dai
Clemson University, ydai@clemson.edu

STUDY ON ELECTROMAGNETIC SCATTERING OF CYLINDERS BURIED IN A HALF SPACE WITH RANDOM ROUGH SURFACES OF FINITE/INFINITE LENGTH

A Dissertation
Presented to
the Graduate School of
Clemson University

In Partial Fulfillment
of the Requirements for the Degree
Doctor of Philosophy
Electrical Engineering

---

by
Yueyang Dai
December 2013

Accepted by:
Dr. Xiao-Bang Xu, Committee Chair
Dr. Anthony Q. Martin
Dr. Pingshan Wang
Dr. Vincent J. Ervin

ABSTRACT

Analysis of electromagnetic scattering of buried objects is a subject of great interest due to its practical importance in both military and civil applications, such as subsurface investigation and target detection. In reality, the earth is of layered structure of random rough interfaces, which leads to a greatly increased complexity of the analysis. However, it is necessary to incorporate the nature of random rough surface and the layered structure because they both have substantial impact on the scattered signature and hence affect the study of inverse scattering and detection of buried objects.

In this dissertation, a Monte-Carlo multidomain pseudospectral time domain (MPSTD) method is developed for investigating the scattering from cylinders buried below a random rough surface separating two half spaces under various conditions. As a prelude, the formulation of multidomain PSTD algorithm is presented. Then, this formulation is extended and combined with the Monte-Carlo approach to analyze the scattering of an object buried below a random rough surface of finite length. In the analysis, special attention is paid to the treatments of the random rough surface including its profile generation, matching with CGL points, and subdomain patching. Next, the scattering of a cylinder buried below a random rough surface of infinite length is studied and a two-step computation model based on the Monte-Carlo MPSTD method is developed. Further, in order to better simulate the real situation, the analysis is then extended to study the scattering from one or more cylinders embedded in a layered half space with random rough surfaces. Finally, a near-zone field to far-zone field transformation technique is developed and presented. Sample numerical results under different conditions, involving random rough surface of various roughness, lower half

space with different permittivities, and cylinders of circular and rectangular shapes are presented, validated, and analyzed. Throughout this research, a numerical technique based on Monte-Carlo method and MPSTD approach has been developed and validated for investigating cylinders buried in a half space with random rough surfaces. It is observed that the roughness of the random rough surface and the electromagnetic properties of the lower half space can significantly affect the scattered signature of the buried object.

DEDICATION

To my parents, my husband, my parents in law and my grandmother

for their endless love and support.

ACKNOWLEDGMENTS

I would like to express my sincere gratitude to my advisor Professor Xiao-Bang Xu for his constant mentoring, patience, understanding, and support throughout my Ph.D. studies at Clemson University. Professor Xu has provided invaluable vision and a wealth of technical instructions to my research and has always provided guidance and assistance both on study and on life at Clemson. He helped me quickly adapt to a foreign environment and always encouraged me during difficult periods as an elder friend. I have learned a lot from his unique technique expertise and deeply admired his commitment to academic excellence and dedication to the academic community and the society. I consider it a true privilege to work with him in the areas of applied electromagnetics. My gratitude is extended to him and his wife auntie Yi-Hong for caring for my growth and life through these years.

I also wish to thank Professor L. Wilson Pearson, Professor Anthony Q. Martin, Professor Pingshan Wang and Professor Vincent J. Ervin for serving on my committee board, sharing their knowledge and for their valuable advice and continuous support. Additionally, I am truly grateful to Professor Chalmers M. Butler for the excellent courses that he taught.

I would also like to thank all my friends, near and distant, whose names I know so well but are too many to be listed here. They have been a constant source of support and strength.

Finally, I am infinitely grateful to my beloved parents for their unfailing support, boundless love, and undoubted confidence in me and to my husband who lived each moment of this experience with me. Their enthusiasm in moments of breakthrough, their

encouragements and comfort in moments of doubts made me go on. None of this work would have been possible without them. Thank you.

TABLE OF CONTENTS

Page

Table of Contents (Continued)

Page

LIST OF FIGURES

List of Figures (Continued)

Figure Page

List of Figures (Continued)

Figure Page

List of Figures (Continued)

Figure Page

CHAPTER ONE

INTRODUCTION

In the Ph.D. dissertation research, an effective numerical technique is developed for the investigation of electromagnetic scattering by objects buried in a layered half space with random rough surfaces.

Over the last few decades, significant research has been undertaken on the analysis of electromagnetic scattering of buried object for its practical importance in both military and civil applications, such as subsurface investigation, target detection, and remote sensing. In reality, the earth is of multi-layered structure with random rough surfaces, which leads to a greatly increased complexity of the analysis. However, it is necessary to incorporate the layered structure and the interface roughness in the electromagnetic scattering study as they can significantly influence the scattered signature. A number of frequency domain numerical methods have been published dealing with the scattered signature of objects near a random rough surface. These methods include the Forward-backward method (FBM) [1], generalized FBM (GFBM) [2], [3], FBM-spectrum accelerate algorithm (FBM/SAA) [4], and finite element method (FEM) [5], [6]. And surface integral equations have been formulated and solved by the method of moments (MoM) [7-10]. The integral equation formulation has also been employed together with a steepest descent fast multipole method (SDFMM) for shallow objects buried under random rough surface [11-14]. In [14], the scattering from two-layered random rough surfaces with and without buried objects has been studied using SDFMM. However, this analysis was limited to the case that the depth of the

underground interface must be less than one free-space wavelength to satisfy the quasi-planar structure constraint of the SDFMM.

An effective numerical technique for determining the scattering of an object near a random rough surface is the Monte-Carlo finite-difference time-domain (FDTD) technique. The FDTD method has been employed for studying the scattering by a random rough surface (without buried objects) [15] , from an object above a random rough surface [16] and a two-dimensional (2D) PEC cylinder above two-layered 1D random rough surface [17]. The FDTD algorithm can obtain direct solutions of the Maxwell's equations in differential form, which avoids the complexity of solving large linear equations generally required by MoM. As indicated in [15], in contrast to the surface integral equation formulation, the FDTD approach is more effective for modeling inhomogeneous objects and complex geometries. And either pulsed or continuous wave (CW) illumination can be used, propagation of both the total and scattered fields can be observed in the time domain. However, the FDTD method has major drawbacks. As pointed out in [18] and [19], the FDTD approach based on the classical Yee scheme with quadratic cell mapping in space gives the modeled structures a "staircase nature" and requires a number of grids per wavelength. Numerous numerical examples reported in the literature have verified that a fine discretization of 10-20 cells per minimum wavelength is required to obtain acceptable accuracy of solutions. Furthermore, the classical FDTD approach is ill-suited for arbitrary geometries with multiple materials as the electromagnetic boundary conditions are not automatically nor exactly imposed and satisfied at these boundaries.

In recent years, the pseudospectral time-domain (PSTD) method [20] has been developed and successfully applied to solve various problems of practical interest, including electromagnetic scattering problems. There are two types of PSTD approaches, the Fourier and Chebyshev PSTD algorithm. The Fourier PSTD algorithm is easy to implement and requires only two points per minimum wavelength, but its accuracy is lower when applied to curved boundaries, perfect conductors, and discontinuous material distributions. The Chebyshev PSTD, using Chebyshev collocation methods to approximate spatial derivatives, has shown a spectral accuracy for discontinuous materials but with slightly increased computational burden of π cells per minimum wavelength.

Although both Fourier and Chebyshev PSTD method demonstrate a remarkable improvement in accuracy and efficiency over FDTD method, they suffer from intensive computation burden when solving problems with strong internal inhomogeneity. To overcome this difficulty, the multidomain PSTD method is a suitable alternative, in which the field components are evaluated locally within a series of non-overlapping subdomains. The multidomain scheme can greatly reduce the cost in the evaluation of spatial derivatives, and can well resolve the strong local inhomogeneity since the subdomain curvature can be made conformal to the problem geometry. The multidomain PSTD has been used for determining the electromagnetic scattering by objects placed in an open space [21] – [28] and for investigating the scattering of 2D cylinders buried in a half space with a planar or an undulating surface [19]. Being compared with the FDTD method, the PSTD method requires significantly less CPU time and core memory for the same or even higher accuracy, as illustrated by a number of numerical experiment results

reported in the literature [19], [24] and [29]. Moreover, the spatial grid is not staggered like the grid used in the classical FDTD Yee scheme, so that the programming is simpler and representation of materials is straightforward. Also, as indicated in [19], in contrast to the classical FDTD Yee scheme that gives "staircase nature", the multidomain PSTD approach can deal with complex geometry with a great flexibility. This nature warrants a high potential of application of the multidomain PSTD method in the analysis of scattering involving random rough surfaces, the geometry of which is apparently complex and needs special attention.

To the best of the author's knowledge, the PSTD method that is more effective than the classic FDTD approach, has not been applied in combination with the Monte-Carlo method for determining the scattering of objects buried below a random rough surface, which can better simulate the real situation and is of practical interest. Therefore, in the dissertation research, a Monte-Carlo multidomain PSTD algorithm is to be developed for investigating the scattering from a 2D object embedded in a layered half space with random rough surfaces.

The rest of the dissertation is organized as the follows. In Chapter 2, the multidomain PSTD algorithm is formulated and then validated for studying the scattering of a cylinder in free space. In Chapter 3, this formulation is extended and combined with the Monte-Carlo approach to analyze the scattering of an object buried below a random rough surface of finite length. In the analysis, special attention is paid to the treatment of the random rough surface. In Chapter 4, the scattering of a cylinder buried below a random periodic rough surface of infinite length is studied and a two-step computation model is developed. Then, the analysis of scattering from cylinders embedded in a

layered structure with random rough surfaces is presented in Chapter 5. Finally, in Chapter 6, the near-zone field to far-zone field transformation technique is discussed.

CHAPTER TWO

FORMULATION AND IMPLEMENTATION OF MULTIDOMAIN PSTD ALGORITHM FOR THE SOLUTION OF 2D SCATTERING PROBLEMS IN FREE SPACE

As a prelude of the execution of the dissertation proposed in Chapter 1, in this chapter, a multidomain Chybeshev PSTD algorithm is formulated and implemented for the solution of scattering of a 2D cylinder located in free space. Sample numerical results are presented to validate the accuracy, flexibility, and efficiency of the algorithm.

2.1 Strategy of the Multidomain PSTD (MPSTD) Algorithm [20]

1) The computational domain is decomposed into a series of non-overlapping subdomains. Each subdomain is then mapped to a unit square by coordinate transformation.
2) The electromagnetic fields are calculated independently within each subdomain at each time step.
3) Patching conditions are applied to pass information between the adjacent subdomains to recover the global solution at one time step.
4) A Runge-Kutta method is utilized to advance the solution to the next time step.

2.2 Formulation of the Multidomain PSTD Algorithm

(1) Division of the Computation Domain and Subdomain Mapping

As the first step of the formulation of the multidomain PSTD algorithm, the computation domain is divided into a number of quadrilateral non-overlapping

subdomains that are naturally conformal with the problem geometry and material distribution as shown in Fig. 2.1. For a general inhomogeneous medium each subdomain contains only smoothly varying materials.

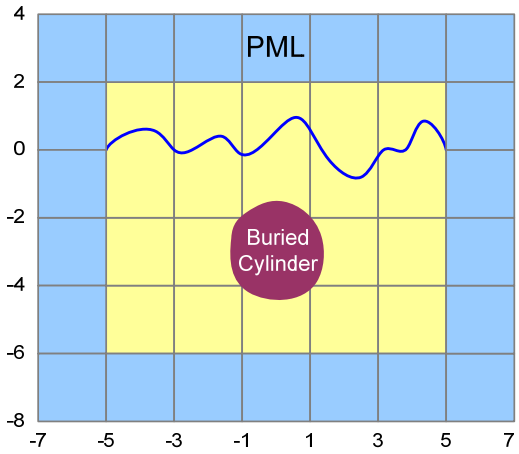

Fig. 2.1 Division of the computation domain into non-overlapping subdomains.

Then, each subdomain, which is in general a curved quadrilateral in (x, y) coordinates, is mapped into a unit square ([-1, 1] x [-1, 1]) in (ξ, η) coordinates by means of the coordinate transformation as illustrated in Fig. 2.2.

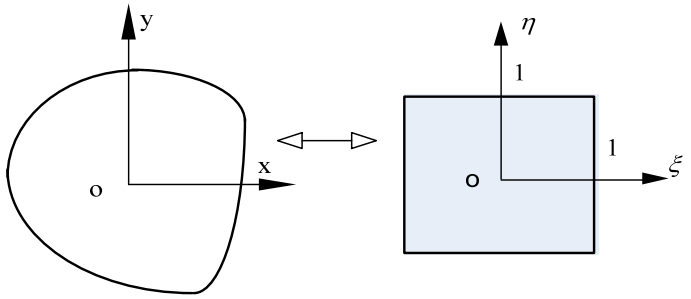

Fig. 2.2 Subdomain mapping from a curved quadrilateral to a unit square.

For a subdomain of rectangular shape, we employ a linear transformation making use of the maxima and minima of x and y as

$$x_i = 0.5\left(x_{\max} - x_{\min}\right)\xi_i + 0.5\left(x_{\max} + x_{\min}\right),$$
$$y_i = 0.5\left(y_{\max} - y_{\min}\right)\eta_j + 0.5\left(y_{\max} + y_{\min}\right). \tag{2.1}$$

And for a curved quadrilateral, a curvilinear transformation, in terms of Lagrange polynomials based on knowledge of the anchor points, is used. If we denote these anchor points as (x_{pq}, y_{pq}) for $(0 \le p \le P,\ 0 \le q \le Q)$, then

$$x = \sum_{p=0}^{P}\sum_{q=0}^{Q} x_{pq} f_p^P(\xi) f_q^Q(\eta),$$
$$y = \sum_{p=0}^{P}\sum_{q=0}^{Q} y_{pq} \phi_p^P(\xi) \phi_q^Q(\eta). \tag{2.2}$$

Next, making use of the coordinate transformation $\xi = \xi(x, y), \quad \eta = \eta(x, y),$ the 2-D Maxwell's equations for *TM*$_z$ polarization in the (*x, y*) coordinates

$$\frac{\partial H_x}{\partial t} = -\frac{1}{\mu}\frac{\partial E_z}{\partial y},$$
$$\frac{\partial H_y}{\partial t} = \frac{1}{\mu}\frac{\partial E_z}{\partial x}, \tag{2.3}$$
$$\frac{\partial E_z}{\partial t} = \frac{1}{\varepsilon}\frac{\partial E_z}{\partial y}\left(\frac{\partial H_y}{\partial x} - \frac{\partial H_x}{\partial y}\right) - \frac{\sigma}{\varepsilon}E_z,$$

can be rewritten in the (ξ, η) coordinate system in matrix form as

$$\frac{\partial q}{\partial t} + A\frac{\partial q}{\partial \xi} + B\frac{\partial q}{\partial \eta} + Cq = 0 \tag{2.4}$$

where $q = (H_x,\ H_y,\ E_z)^T$, *A*, *B*, and *C* are the coefficient matrices given in [19] and [20].

(2) Chebyshev Spectral Collocation Procedure

After the coordinate mapping, the Chebyshev spectral collocation procedure [20], [30]-[32] is performed for treating the electromagnetic field quantities and their spatial derivatives in the transformed (ξ, η) coordinate. First, the grid points in the transformed coordinates are taken at the Chebyshev-Gauss-Lobatto (CGL) points,

$$\begin{aligned} \xi_i &= -\cos(\frac{i\pi}{N}), \quad i = 0,1,...N \\ \eta_j &= -\cos(\frac{j\pi}{M}), \quad j = 0,1,...M. \end{aligned} \tag{2.5}$$

Then, the electromagnetic field components $q(\xi,\eta)$ are interpolated by the tensor-product Chebyshev-Lagarange polynomial as

$$q(\xi,\eta) = \sum_{i=0}^{N}\sum_{j=0}^{M} q(\xi_i,\eta_j)\, g_i(\xi) g_j(\eta) \tag{2.6}$$

where the Lagrange interpolation polynomials are defined by

$$\mathrm{g}_i(\alpha) = \frac{(1-\alpha^2)T'_N(\alpha)(-1)^{i+N+1}}{c_i N^2(\alpha-\alpha_i)} \tag{2.7}$$

in which $\alpha = (\xi,\eta)$, $c_i = 1+\delta_{i0}+\delta_{iN}$, and $T_N(x)$ is the N^{th}-order Chebyshev polynomial $T_N(x) = \cos(N\cos^{-1}x)$. Finally, with the interpolation in (2.7), the spatial derivatives of the field quantities $q(\xi,\eta)$ with respect to ξ and η are expressed as

$$\begin{aligned} \frac{\partial q(\xi_i,\eta_j)}{\partial \xi} &= \sum_{k=0}^{N} D_{ik}^{\xi} q(\xi_k,\eta_j) \\ \frac{\partial q(\xi_i,\eta_j)}{\partial \eta} &= \sum_{k=0}^{M} D_{jk}^{\eta} q(\xi_i,\eta_k) \end{aligned} \tag{2.8}$$

where the differentiation matrix D_{ik}^{α} is given by

$$\mathrm{D}_{ik}^{\alpha}=\begin{cases}-\dfrac{c_i}{c_k}\dfrac{(-1)^{i+k}}{\alpha_k-\alpha_i} & i\neq k,\\ -\dfrac{\alpha_k}{2\left(1-\alpha_k^2\right)} & 1\le i=k\le N\text{-}1,\\ -\dfrac{2N^2+1}{6} & i=k=0,\\ \dfrac{2N^2+1}{6} & i=k=N.\end{cases} \tag{2.9}$$

(3) Implementation of Well-Posed PML

In order to truncate the unbounded medium and confine the solution in a finite computational domain, an absorbing boundary condition (ABC) is introduced, by implementing a well-posed perfectly matched layer (PML) [33] - [37] surrounding the "regular" region. In the PML, the complex coordinate-stretching variables

$$\partial x \Rightarrow \left[1+\frac{i\omega_x(x)}{\omega}\right]\partial x,\quad \partial y \Rightarrow \left[1+\frac{i\omega_y(y)}{\omega}\right]\partial y, \tag{2.10}$$

are used to rewrite the Maxwell's equations for the electromagnetic field in the PML region. Defining new field variables for the PML region,

$$\hat{H}_x = H_x + \omega_x Q_x,\quad \hat{H}_y = H_y + \omega_y Q_y \tag{2.11}$$

the Maxwell's equation in PML region can be written as

$$
\begin{aligned}
\frac{\partial \hat{H}_x}{\partial t} &= -\frac{1}{\mu}\frac{\partial E_z}{\partial y} + \left(\omega_x - \omega_y\right)(\hat{H}_x - \omega_x Q_x) \\
\frac{\partial \hat{H}_y}{\partial t} &= \frac{1}{\mu}\frac{\partial E_z}{\partial x} + \left(\omega_y - \omega_x\right)(\hat{H}_y - \omega_y Q_y) \\
\frac{\partial E_z}{\partial t} &= \frac{1}{\varepsilon}\left(\frac{\partial \hat{H}_y}{\partial x} - \frac{\partial \hat{H}_x}{\partial y}\right) - \frac{\sigma}{\varepsilon}E_z - \left(\omega_x + \omega_y\right)E_z \\
&- \left[\frac{\sigma}{\varepsilon}\left(\omega_x + \omega_y\right) + \omega_x\omega_y\right]P_z - \frac{\sigma}{\varepsilon}\omega_x\omega_y K_z
\end{aligned}
\tag{2.12}
$$

where

$$
\frac{\partial Q_x}{\partial t} = \hat{H}_x - \omega_x Q_x \ , \quad \frac{\partial Q_y}{\partial t} = \hat{H}_y - \omega_y Q_y \ , \quad \frac{\partial P_z}{\partial t} = E_z \ , \quad \frac{\partial K_z}{\partial t} = P_z \ . \tag{2.13}
$$

The appropriate profiles of ω_x and ω_y are selected for the complex coordinate-stretching variables to adjust the attenuation in the PML region.

(4) Subdomain Patching

In the multidomain PSTD algorithm, after the solution in each individual subdomain, the fields at the interfaces between adjacent subdomains do not naturally satisfy the boundary conditions. And we need to exchange information between the subdomains to obtain the global solutions. This is done by means of the subdomain patching [19], [20], [24], that is, at an interface separating two subdomains, we enforce the physical boundary conditions that require continuity of the tangential components of the electric and magnetic field at a dielectric interface; and zero tangential electric field component and normal magnetic field component on a perfect electric conductor (PEC) surface.

(5) Plane Wave Excitation and TF/SF Formulation

In the past, the total field/scattered field (TF/SF) formulation [19], [20], [38] and the pure scattered field method [39], [40] have both been employed to implement a plane wave incidence in the PSTD algorithm for the solution of scattering problems. However, as pointed out in [20], the pure scattered field method is potentially complicated if a complex surface shape is involved. Therefore, in the dissertation research, we employ the TF/SF formulation to enforce the plane wave excitation. The total field is calculated in the interior region and the scattered field is computed in the exterior region. Then, the boundary condition requirements of continuity of the tangential components of the electric and magnetic field are enforced at the interface between the TF and SF regions.

(6) Time Stepping

The 2-D Maxwell's equation (2.4), formulated in the (ξ, η) coordinates contains both spatial derivatives and time derivatives. The spatial derivatives of the fields at the grid points are obtained by the Chebyshev spectral collocation procedure presented above. To take care of the time derivatives, we use a fourth order, five-stage Runge-Kutta method [41] – [43] for the time integration to advance the solution to the next time step.

(7) Application of Filtering Technique

As pointed in [20], numerical oscillations may appear when pseudospectral methods are applied. These oscillations are directly caused by the solution discontinuities, and have a high-frequency character. For the multidomain PSTD scheme, such discontinuities can arise from edges and corners at subdomain interfaces, potentially

causing late-time instability. The instability would be severe due to edges and corners on a random rough surface as a subdomain interface.

The filtering technique [20] is an effective way to overcome this difficulty. By multiplying the Chebyshev coefficients with a gradually decreasing function σ_n, it can reduce the high-frequency components and thus improve the stability of the MPSTD solutions. Moreover, with the utilization of the filtering technique, larger time step may be used, which can greatly reduce the computation time. The filtering is implemented after the fields are updated in the whole computational domain. The filtering function σ_n is selected to be an exponential cut-off function [44], [45] for this research.

2.3 Numerical Results and Discussion

The MPSTD algorithm formulated above is implemented to determine the scattering of a 2D cylinder located in free space. Sample numerical results are presented and validated in this section. For the numerical results presented, the excitation is taken to be a normal TM_z plane wave incidence, the time domain function of which is the first derivative of Blackmann-Harris window function,

$$W_{bhw1^{st}}(t) = \begin{cases} -\sum_{n=1}^{3} \frac{n\pi}{T} a_n \sin\left(\frac{2n\pi t}{T}\right), & 0 < t < T \\ 0, & otherwise \end{cases} \tag{2.14}$$

where a_1=-0.488, a_2=0.145, a_3=-0.01022222 and T=1.55/f, f is the central frequency, which is taken to be 100MHz.

(1) Plane Wave Propagation in Free Space

To validate the MPSTD algorithm, first, we employ it to compute the total field of a plane wave propagating in -y direction in an open space, in absence of scatterer. The computation domain is illustrated in Fig. 2.3(a), in which a grid with 14×14 cells is used for each subdomain. The computed total electric field $E_{z,total}$ is compared with the incident field $E_{z,inc}$. From the comparison shown in Fig. 2.3 (b) one observes that the two curves fall on top of each other as expected.

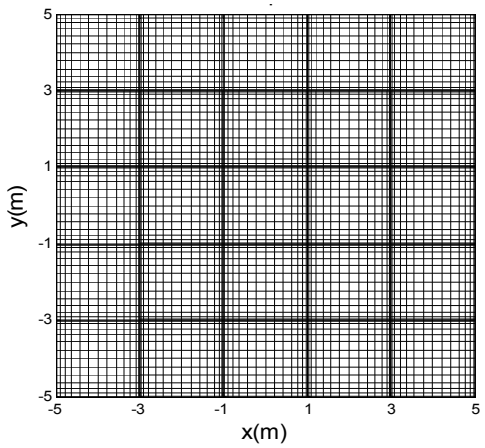

(a)

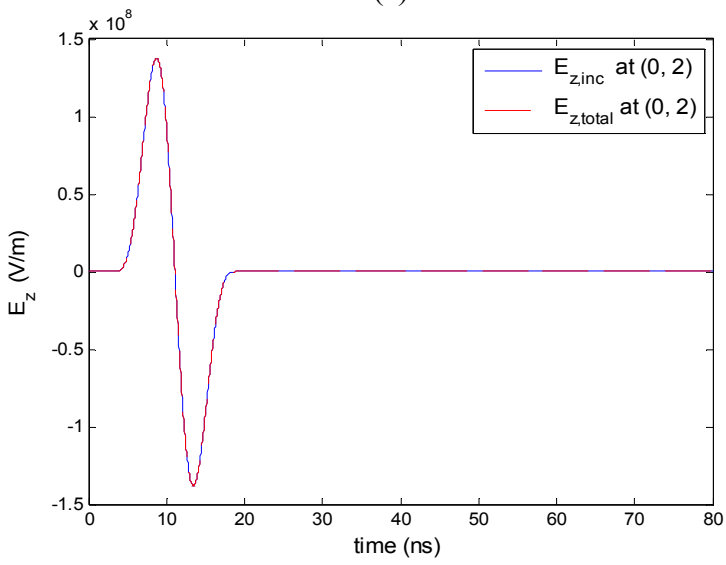

(b)

Fig. 2.3 Plane wave propagation in free space

(a) Geometry of the computation domain,

(b) Comparison between the total field and the incident field.

(2) Scattering from a Square PEC Cylinder in Free Space

In the second example, scattering of a square PEC cylinder with side length 2*m* under a normal plane wave incidence is presented. The geometry and the computation domain are depicted in Fig. 2.4(a). To check the result, we compare the tangential component of the total magnetic field at the center point on the illuminated side of the square PEC cylinder with that of the incident magnetic field. As shown in Fig. 2.4(b), the magnitude of the tangential component of the total magnetic field is about equal to that of the incident field doubled, as one would expect.

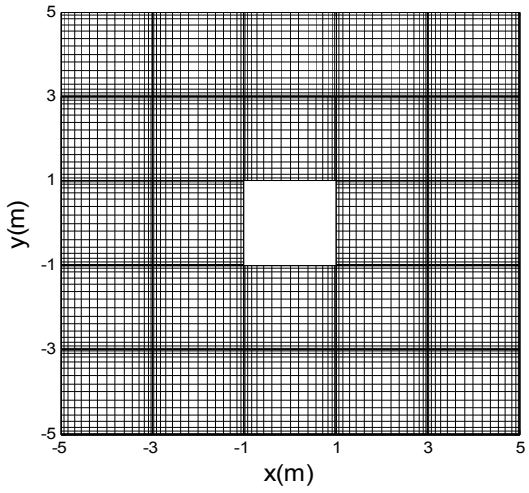

(a)

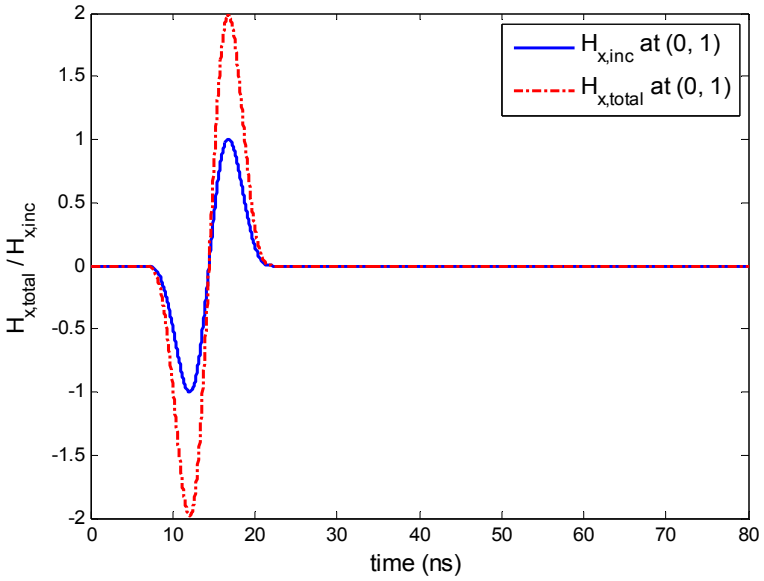

(b)

Fig. 2.4 Plane wave scattering from a PEC square cylinder in free space

(a) Computation domain, (b) Comparison of $H_{x,inc}$ and $H_{x,total}$ at (0, 1).

(3) Scattering from a Circular PEC Cylinder in Free Space

The third example considers the plane wave scattering from a PEC circular cylinder under normal incidence. The geometry and the grid points used are shown in Fig. 2.5(a). The radius of the circular cylinder is 2*m* and the observation point is located at (-2.1238, -1.9287). The MPSTD computation result is compared with the analytical solution [46] in Fig. 2.5(b), in which an excellent agreement is observed.

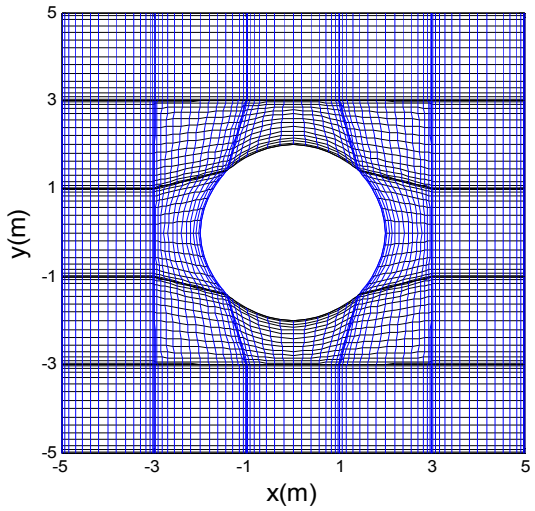

(a)

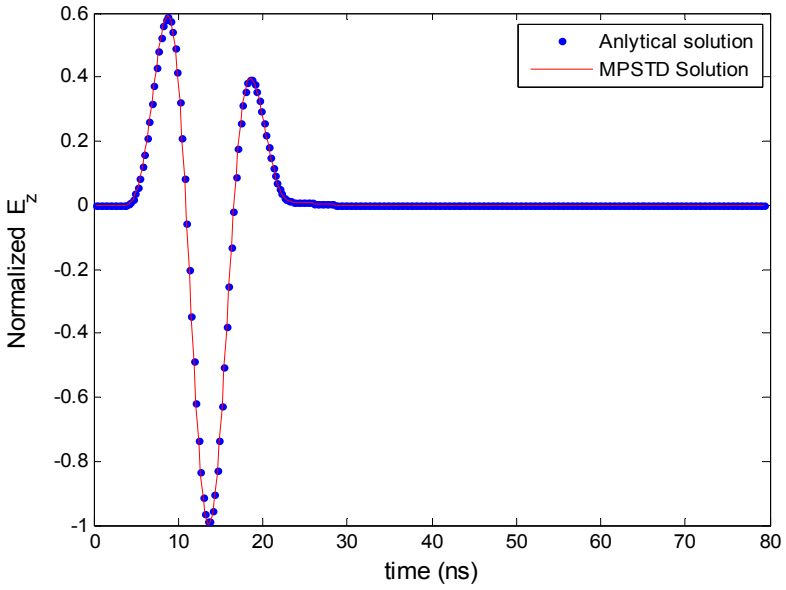

(b)

Fig. 2.5 Plane wave scattering from a PEC circular cylinder in free space

(a) Computation domain, (b) Comparison of the MPSTD results with analytical solution.

(4) Scattering from a Dielectric Circular Cylinder in Free Space

In the last example, we consider the scattering of a dielectric circular cylinder with radius of $2m$, $\varepsilon_r = 4$ and $\mu_r = 1$, centered at the origin. The geometry is illustrated in Fig. 2.6(a). The MPSTD computation result of the normalized scattered field observed at (-2.1036, -2.1036) is presented in Fig. 2.6(b), which agrees with the published data given in [19].

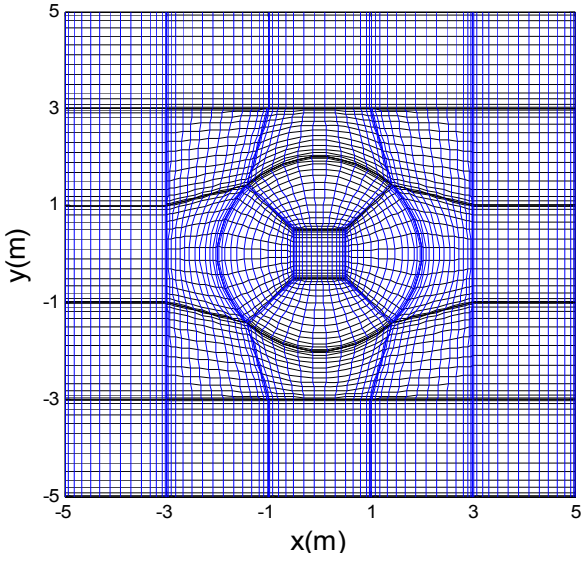

(a)

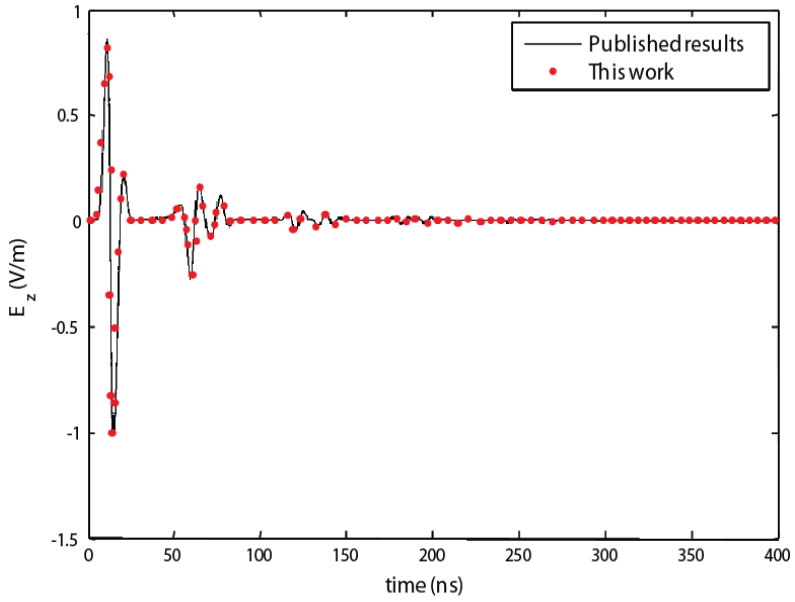

(b)

Fig. 2.6 Plane wave scattering from a dielectric cylinder in free space

(a) Geometry of the computation domain,

(b) Comparison of the MPSTD result with published data.

CHAPTER THREE

MONTE-CARLO MPSTD ANALYSIS OF SCATTERING OF CYLINDERS BURIED BELOW A RANDOM ROUGH SURFACE OF FINITE LENGTH

In this chapter, we present formulation of a Monte-Carlo MPSTD numerical technique for investigating the scattering from a cylinder buried below a random rough surface of finite length. In the formulation, special attention is paid to the treatment of the random rough surface. Sample numerical results of the scattering are presented, and analyzed. After validation of the formulation, it will be extended for the analysis of scattering of a cylinder buried below a periodic random rough surface of infinite length in the next chapter.

3.1 Treatment of the Random Rough Surface in the Monte-Carlo Multidomain PSTD (MPSTD) Algorithm Formulation

(1) Generation of Random Rough Surface Profile

Different from the previously published PSTD analysis of electromagnetic scattering problems, this research involves a random rough surface as shown in Fig. 3.1.

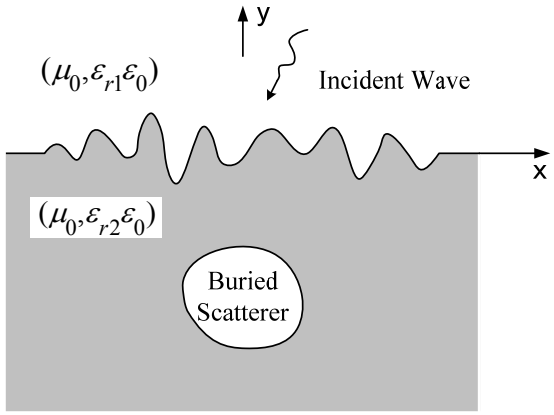

Fig. 3.1 Cylinder buried below a random rough surface of finite length.

A random rough surface with Gaussian spectrum profile $y = f(x)$ [47], [48] can be generated as the follows. First, a set of uniformly distributed sampling points is selected by

$$x_m = mL / N \tag{3.1}$$

where L is the length of the random rough surface, N is the number of the sample points. Then the rough surface profile can be obtained using the inverse Fourier transform

$$y = f(x_m) = \frac{1}{L} \sum_{n=-\frac{N}{2}+1}^{\frac{N}{2}} b_n \exp(i \frac{2\pi nm}{N}) \tag{3.2}$$

where the inverse Fourier transform coefficients are given by

$$b_n = \begin{cases} \sqrt{2\pi LW(0)} r_\alpha, n = 0; \\ \sqrt{2\pi LW(\frac{\pi N}{L})} r_\beta, n = \frac{N}{2}; \\ \sqrt{2\pi LW(|k_n|)} [\frac{1}{\sqrt{2}} (r_\sigma + i r_\zeta)], n = -\frac{N}{2} + 1, ..., -2, -1; \\ \{\sqrt{2\pi LW(|k_{-n}|)} [\frac{1}{\sqrt{2}} (r_\sigma + i r_\zeta)]\}^*, n = 1, 2, ..., \frac{N}{2} - 1; \end{cases} \tag{3.3}$$

in which r_σ and r_ζ are random numbers and

$$W(k_n) = \frac{h^2 l}{2\sqrt{\pi}} e^{-(\frac{\pi n}{L} l)^2} \tag{3.4}$$

where h and l are the *rms* height and the correlation length of the random rough surface. Such generated a sample random rough surface profile is shown in Fig. 3.2 in blue color.

(2) Random Rough Surface Profile Matching with CGL points

Note that the random rough surface profile $y = f(x_m)$ is generated as a function of x_m. But in a MPSTD subdomain that is partially bounded by the rough surface, the profile

y_{mapped} is a function of x_{mapped}. Both x_{mapped} and y_{mapped} are related to the CGL points in the (ξ, η) coordinate by the coordinate transformation. Since x_m are uniformly distributed but x_{mapped} are not, they are normally different; hence the two profiles of $y = f(x_m)$ and y_{mapped} in general do not coincide. However, for each point of x_{mapped}, we can find the points x_m adjacent to it, then employ an interpolation technique to match x_m with x_{mapped}; and subsequently $y = f(x_m)$ with y_{mapped}. After the matching making use of the interpolation, a comparison of the random rough surface profile with Gaussian spectrum and that obtained using the mapped CGL points is illustrated in Fig. 3.2, from which we observe that these two profiles fall on top of each other. Then, using the values of $y = f(x_m)$ (or equivalently y_{mapped}) on the random rough surface profile, the other grid points within a subdomain that is partially bounded by the random rough surface can be determined.

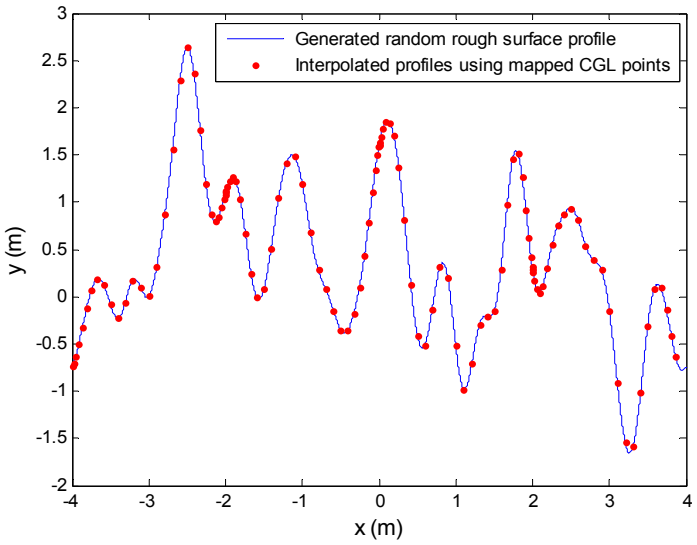

Fig. 3.2 Comparison of a random rough surface profile with Gaussian spectrum and that obtained using mapped CGL points.

(3) Subdomain Patching for Subdomains Separated by Random Rough Surface

As shown in Chapter 2, in the multidomain PSTD algorithm, after the solution in each individual subdomain, it is necessary to execute the subdomain patching by enforcing the physical boundary conditions on the subdomain interfaces. In particular, at a random rough surface separating two dielectric subdomains of different electromagnetic properties, we enforce the continuity of the tangential components of the fields, and the details are presented below. As shown in Fig. 3.3, at a grid point on the random rough surface, the unit vector normal to the surface can be found by

$$\hat{n} = \frac{-f'(x)\hat{x} + \hat{y}}{\sqrt{1 + f'(x)^2}}, \tag{3.5}$$

and the unit vector tangential to the surface is

$$\hat{l} = \frac{\hat{x} + f'(x)\hat{y}}{\sqrt{1 + f'(x)^2}}. \tag{3.6}$$

In equations (3.5) and (3.6), $f'(x)$ is the slope of the random rough surface at that point.

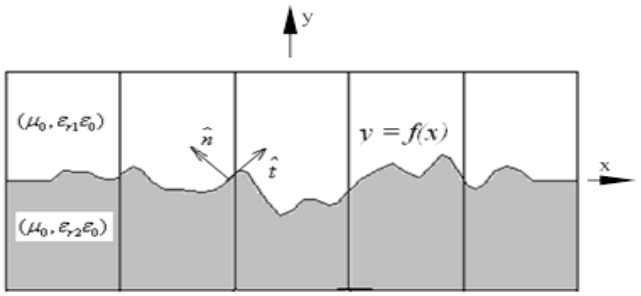

Fig. 3.3 Unit vectors tangential and normal to a random rough surface.

Using these two equations, we can extract the normal and tangential component of the fields by taking dot products of $\hat{n}$ or $\hat{l}$ with the corresponding field. Then, by enforcing the condition that the tangential components of the fields must be continuous and the normal components of the fields are left unchanged, the updated electric field for TM_z polarization can be determined by

$$E'_{z_{\frac{1}{2}}} = \frac{1}{2}(E_{z1} + E_{z2}), \tag{3.7}$$

and the updated magnetic field components are found to be

$$H_{x1}' = \frac{1}{2}\frac{1}{1+f'(x)^2}[H_{x1} + H_{x2} + f'(x)(H_{y1} + H_{y2})] - \frac{f'(x)}{1+f'(x)^2}[-f'(x)H_{x1} + H_{y1}], \tag{3.8a}$$

$$H_{y1}' = \frac{1}{2}\frac{f'(x)}{1+f'(x)^2}[H_{x1} + H_{x2} + f'(x)(H_{y1} + H_{y2})] + \frac{1}{1+f'(x)^2}[-f'(x)H_{x1} + H_{y1}], \tag{3.8b}$$

in region 1 and

$$H_{x2}' = \frac{1}{2}\frac{1}{1+f'(x)^2}[H_{x1} + H_{x2} + f'(x)(H_{y1} + H_{y2})] - \frac{f'(x)}{1+f'(x)^2}[-f'(x)H_{x2} + H_{y2}], \tag{3.9a}$$

$$H_{y2}' = \frac{1}{2}\frac{f'(x)}{1+f'(x)^2}[H_{x1} + H_{x2} + f'(x)(H_{y1} + H_{y2})] + \frac{1}{1+f'(x)^2}[-f'(x)H_{x2} + H_{y2}]. \tag{3.9b}$$

in region 2.

3.2 Determination of the Composite Fields and Its Implementation in the TF/SF Formulation

A buried cylinder shown in Fig. 3.1 is below a random rough surface separating two semi-infinite homogeneous spaces. A plane wave impinges at the rough surface and its time function may be a pulsed or continuous wave. The incident wave driving the scattering of a buried cylinder is different from that of an object in an open space. It should be determined by a "three-wave approach" that was used in FDTD analysis for the scattering of an object buried below a planar interface [49] – [51]. As pointed out in [49], the driving incident wave is the composite of the initial incident, reflected, and transmitted waves. In the upper half space, the driving composite field is the sum of the initial incident field plus the reflected field; and in the lower half space, the driving

composite field (the driving incident field to the buried cylinder) is the transmitted field. The initial incident field, the reflected and the transmitted filed can be calculated analytically in absence of the scatterer in time domain, taking into account the time delay for the fields to reach a point on the TF/SF interface. Such calculated driving composite field can be readily enforced on the TF/SF interface in the MPSTD algorithm.

The driving composite field determined from the "three-wave approach" for the scattering of a cylinder buried below a planar interface is extended in the dissertation research for the analysis of the scattering of a cylinder buried below a random rough surface. For the calculation of the driving composite field, a virtual planar interface is placed at $y = 0$ along the rough surface as shown in Fig. 3.4. The random rough surface just causes additional inhomogeneities above/below the virtual planar interface; and these inhomogeneities can be treated as "additional scatterers" touching the virtual planar surface, illuminated by the composite fields that can be determined by the three-wave approach.

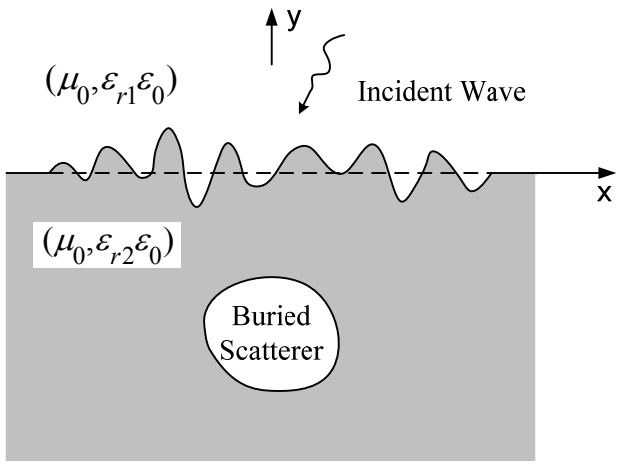

Fig. 3.4 A virtual planar interface for the calculation of composite driving fields.

3.3 Monte-Carlo Statistic Average

Since the rough surface involved in the dissertation research has a random nature, a statistic average of the scattering of the buried cylinder needs to be determined. As pointed in [52], the Monte-Carlo method (MCM) is also known as the method of statistical trials. This method has been used in the past together with an integral equation formulation in the frequency domain [12] and with FDTD method in the time domain [15], [16] for the analysis of electromagnetic scattering involving a random rough surface. In this research, the Monte-Carlo analysis is carried out by the following steps. First, a set of random rough surfaces with Gaussian spectrum is generated. Then, the multidomain PSTD algorithm formulated above is employed to determine the scattering of a buried object below each of the rough surfaces generated. And finally, the statistic average of the scattering is determined. To make sure that the Monte-Carlo statistic average results converge, a series of numerical tests is performed and presented in the next section.

3.4 Numerical Results and Discussion

(1) Covergence Test for the Monte-Carlo MPSTD Method

For the Monte-Carlo method as a method of statistical trials, its convergence is an important issue. To make sure that the numerical results of the Monte-Carlo MPSTD technique formulated above converges, a set of N random rough surfaces is generated and the multidomain PSTD numerical technique is employed N times corresponding to each of the random rough surfaces generated, and then the Monte-Carlo statistic average is obtained. For the numerical tests, the upper half space is taken to be air ($\varepsilon_{r1} = 1$) and the lower half space is characterized by $\varepsilon_{r2} = 3$. The random rough surface is of length

$L = 10m\ (3.33\lambda_0)$, correlation length $l_c = 0.5m\ (0.167\lambda_0)$, and the *rms* height $\sigma_{rms} = 0.3m\ (0.1\lambda_0)$.

In the first test, only the random rough surface, in absence of scatterer, is considered. The geometry and computation domain are illustrated in Fig. 3.5(a). The numerical results of electric field E_z obtained at an observation point (1, 2) corresponding to different number N are presented in Fig. 3.5(b). From the data shown in this figure, one notes that the numerical results have a significant change when N is increased from 2 to 8 and 8 to 14, but the change becomes very little when N is further increased from 14 to 18 and 22. In other words, the Monte-Carlo MPSTD results converge after it is executed 14 times for solving this problem.

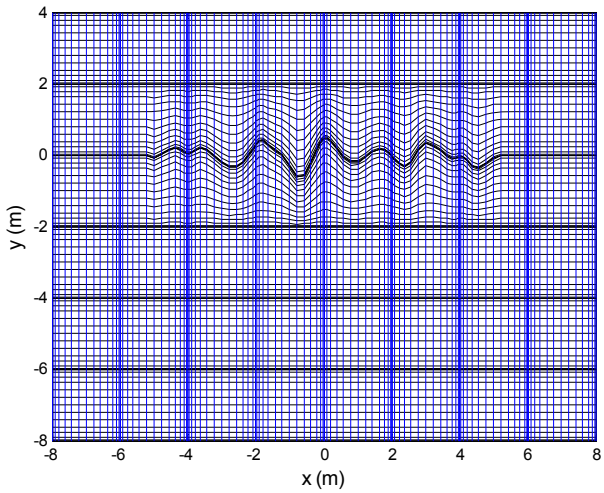

(a)

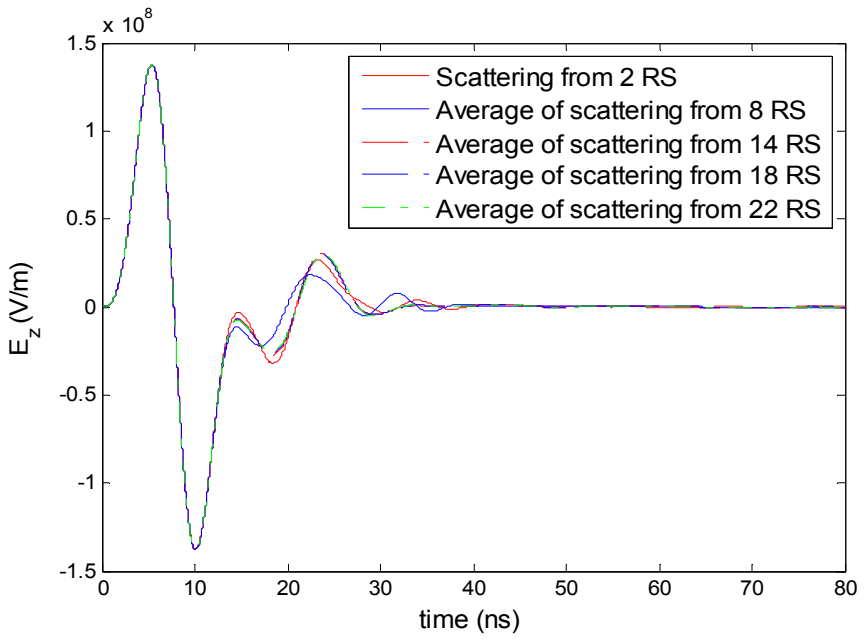

(b)

Fig. 3.5 Scattering of random rough surfaces

(a) Computational domain,

(b) Convergence test results for various numbers of random rough surfaces.

In the second numerical test, a rectangular lossy dielectric cylinder ($\varepsilon_r = 50$, $\mu_r = 1$, σ=0.01s/m) of dimension $2m \times 2m$ ($0.67\lambda_0 \times 0.67\lambda_0$) is placed in a homogeneous medium below the random rough surface as shown in Fig. 3.6(a). The parameters of lower half space are $\varepsilon_r = 3$, $\mu_r = 1$, σ=0 . The numerical results of E_z observed at (-1, 2) are presented in Figs. 3.6(b), from which one observes the convergence of the numerical results similar to that of the previous numerical test. In addition, the electric field spatial distribution at *t=15ns* and *t=30ns* are given in 3.6(c) and 3.6(d) respectively, where the shape of the rough surface and part of the lossy dielectric buried cylinder are illustrated.

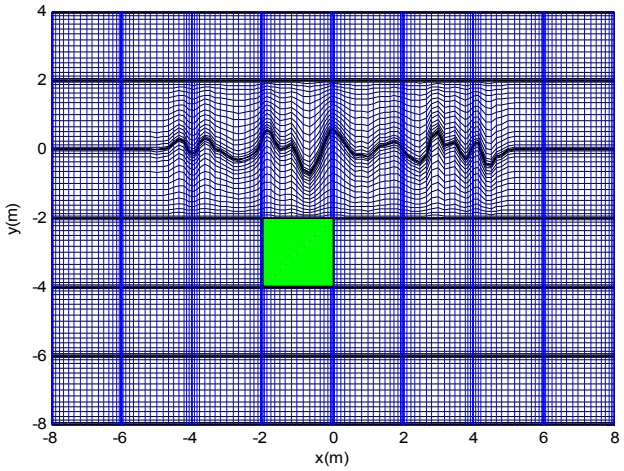
y(m)
x(m)
4
2
0
-2
-4
-6
-8
-8
-6
-4
-2
0
2
4
6
8

(a)

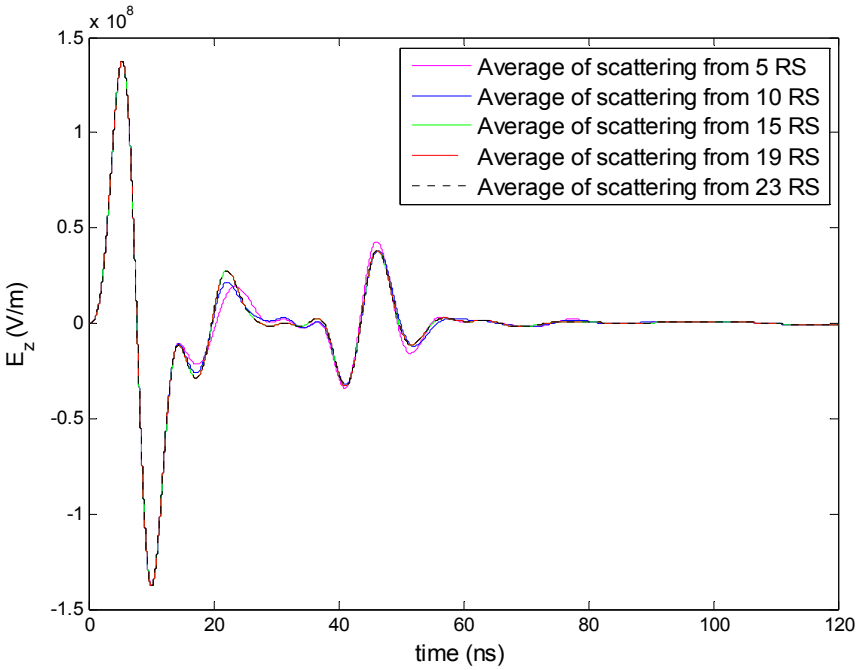
x 10^8
1.5
1
0.5
0
-0.5
-1
-1.5
E_z (V/m)
0
20
40
60
80
100
120
time (ns)
Average of scattering from 5 RS
Average of scattering from 10 RS
Average of scattering from 15 RS
Average of scattering from 19 RS
Average of scattering from 23 RS

(b)

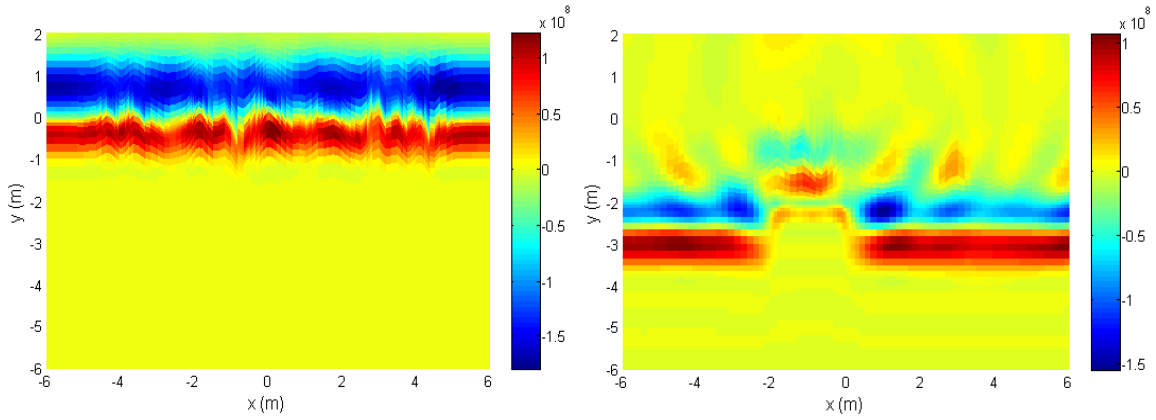

(c) (d)

Fig. 3.6 Scattering of a rectangular lossy dielectric cylinder buried below a random rough surface observed at (1, 2)

(a) Computational domain,

(b) Convergence test results for various numbers of random rough surfaces,

(c) Field distribution of E_z at *t=15ns*, (d) Field distribution of E_z at *t=30ns*.

(2) Validation of the Monte-Carlo MPSTD Algorithm

To validate the Monte-Carlo MPSTD algorithm formulated, next, we present numerical results of the scattering of a circular PEC cylinder of radius $r = 1.414m$ ($0.47\lambda_0$) buried below a random rough surface, which is of the same parameters given in the previous section. The computation domain with grids is depicted in Fig. 3.7(a). Fig. 3.7(b) shows the numerical results of E_z observed above the rough surface at (0, 2) with various lower half space relative permittivity ε_{r2}. From the data presented, one notes that as ε_{r2} changes from 3, to 2, and finally to 1, the results gradually reduce to that for the circular PEC cylinder located in free space, as expected. Moreover, one observes that as ε_{r2} = 1, the numerical result shown in this figure is exactly the same as the analytical

solution, as it should be. Also, it is of interest to note that there is a time delay of the scattered wave propagation as ε_{r2} increases. This is due to the fact that the scattered wave propagates in the lower half space at a slower speed corresponding to a larger relative permittivity there. In addition, the data presented shows how the electromagnetic property of the lower half space can affect the scattered signature. But as the relative permittivity of the lower half space becomes 1, the contribution from the random rough surface disappears, because the media interface does not exist anymore as the relative permittivities of the two half spaces become the same.

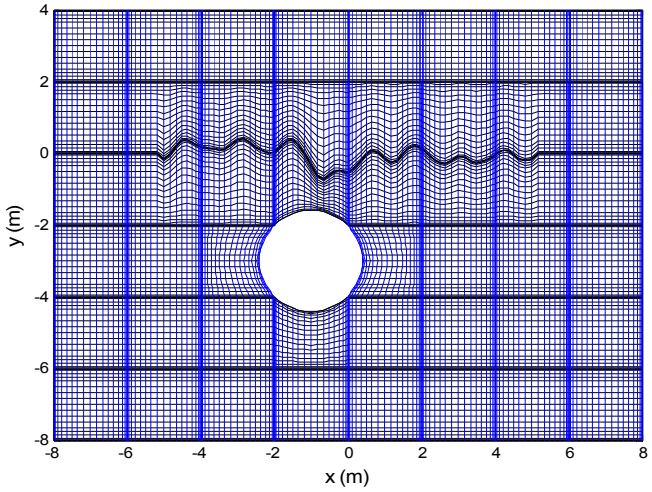

(a)

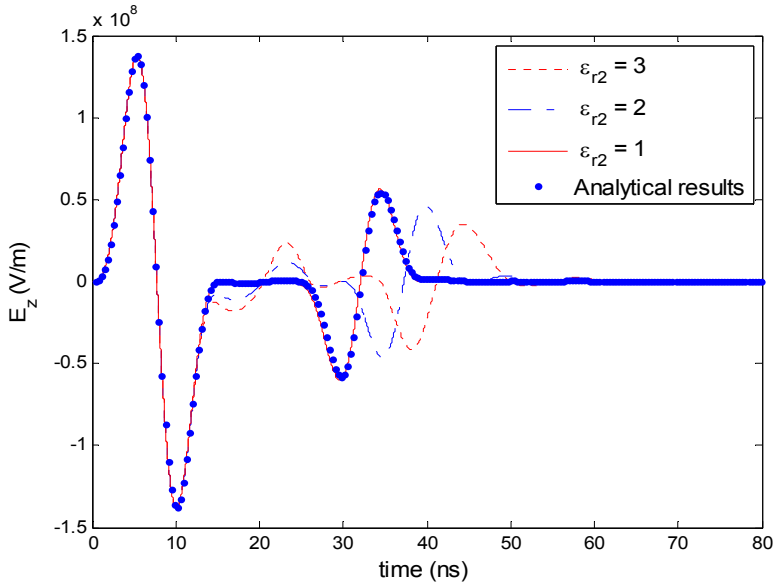

(b)

Fig. 3.7 Scattering of a circular PEC cylinder buried below a random rough surface (a) Geometry and the computation domain, (b) E_z observed at (0, 2) for various ε_{r2}.

(3) Effect of Roughness of Random Rough Surface

In the next two examples, we present the numerical results to illustrate the effect of roughness of a random rough surface on the scattering of normal plane wave incidence. The first one is for a random rough surface only; its geometry and computation domain remain to be the same as that illustrated previously in Fig. 3.5(a). The scattering of the random rough surface with various *rms* height σ_{rms}, observed at (1, 2), is shown in Fig. 3.8. As illustrated in this figure, the *rms* height of a random rough surface can significantly affect its scattering. It is of interest to observe that the scattering from a random rough surface is weaker than that by a flat surface, and when the roughness increases, the strength of the scattered field gets weaker. This is due to the fact that the scattered field by a flat surface under plane wave normal incidence is simply the reflected

wave. The waves reflected from all the points on the flat surface are in one single direction. But for a random rough surface, the waves scattered from different points would be in different directions and they may unconstructively interfere each other. Also, it is worth noting that as the *rms* height reduces from $0.3m\,(0.1\lambda_0)$ to $0.2m\,(0.067\lambda_0)$ and then $0.1m\,(0.033\lambda_0)$, the numerical results of the electric field E_z tend to gradually converge to the analytical result for a flat surface $(\sigma_{rms} = 0)$, as expected.

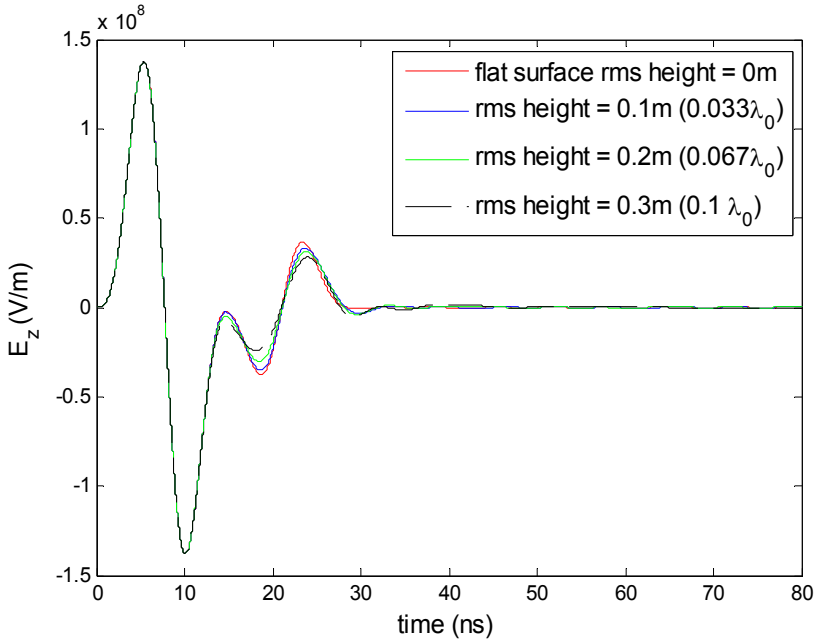

Fig. 3.8 Scattering of a random rough surface observed at (1, 2) for various σ_{rms}.

The next example is for the scattering of a circular PEC cylinder buried below the random rough surface studied in the previous example. The numerical results of E_z observed above the rough surface at (1, 2) for various *rms* height σ_{rms} is presented in Fig. 3.9, where a similar phenomenon is observed as seen in Fig. 3.8. As σ_{rms} reduces from $0.3m\,(0.1\lambda_0)$ to $0.2m\,(0.067\lambda_0)$ and then $0.1m\,(0.033\lambda_0)$, the numerical results of the electric field E_z tend to gradually converge to that for the circular cylinder buried below a

flat surface ($\sigma_{rms} = 0$), as expected. In addition, this figure shows that the roughness of the random rough surface has a significant influence on the scattering of the buried cylinder. By comparing Figs. 3.8 and 3.9, one notes a big difference between the fields presented in these two figures, which represents a strong scattered signature of the buried cylinder.

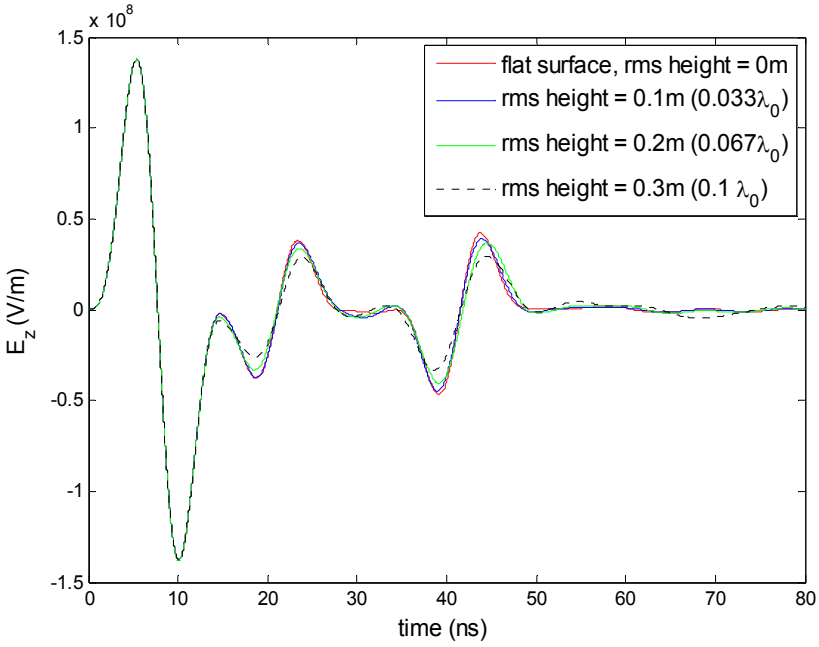

Fig. 3.9 Scattering of a circular PEC cylinder buried below a random rough surface observed at (1, 2) for various σ_{rms}.

CHAPTER FOUR

SCATTERING OF CYLINDERS BURIED BELOW A RANDOM PERIODIC ROUGH SURFACE OF INFINITE LENGTH

The scattering of cylinders buried below a random rough surface of finite length has been studied in the previous chapter. However, in reality, the random rough surface could be of large (or infinite) length, which can be viewed as an extensive periodic structure. To take care of this more realistic case, in this chapter, we develop a Monte-Carlo MPSTD numerical technique for investigating the scattering of a cylinder buried below a random periodic rough surface of infinite length. In the development, the periodic boundary condition (PBC) is enforced. The computation model is formulated by two steps as presented in details below. After the computation, sample numerical results are presented and analyzed to validate the numerical technique.

4.1 Computation Model for Scattering from a Random Periodic Rough Surface Alone

(1) Introduction to a Random Periodic Extensive Rough Surface

In the computation model for simulating the scattering of an infinite-long rough surface, the rough surface must be artificially truncated at the two ends of the computation domain that is of finite length. This truncation would force the current on the rough surface to be zero at the truncation edges. Subsequently, such an abrupt change of surface current would cause artificial reflection from the two edges. To prevent the current discontinuity, a taped incident wave has been introduced in spatial or spectral domain to make the excitation decay gradually and become negligible at the surface

edges [48]. But as the incident angle increases, especially at low grazing angles, the illuminated area becomes large, which would require huge memory and causes complexity, making the numerical simulation difficult.

In the dissertation research, we consider a random rough surface of infinite length as a periodic extensive structure as shown in Fig. 4.1, where L is the length of one period. To simulate the statistic characteristics of the roughness of a random rough surface, L should be greater than several correlation lengths l_c and in general it is taken to be [53]

$$L \geq 15 l_c \tag{4.1}$$

Then the diffraction from the truncated edges can be eliminated by enforcing a periodic boundary condition (PBC) there [48, 54-55]. According to the Floquet Theorem [56], by enforcing the PBC, the fields along an extensive periodic rough surface can be readily described by the fields in one period cell. The advantage of using the periodic extensive structure and the PBC is that only one period of rough surface needs to be included in the computation domain, which can significantly improve the computation efficiency.

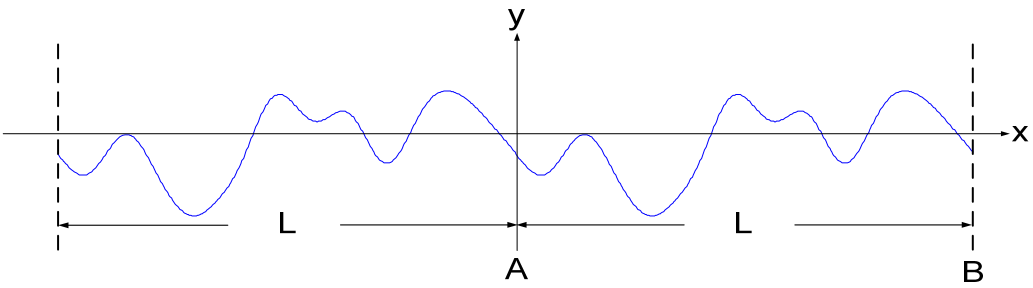

Fig. 4.1 A random periodic rough surface.

(2) Formulation of the Computation Model

The MPSTD computation domain for studying the scattering from a periodic random rough surface is depicted in Fig. 4.2. For simplicity, the PML regions

surrounding the 'regular' region are not included there. As shown in this figure, the computation domain is divided into two regions: the total field region and the scattered field region. In the total field region enclosed by *A'B'E'F'*, the field is the sum of the incident field to the rough surface, which is the driving composite field described in Chapter 3, and the field scattered by the rough surface. In the scattered field region enclosed by *C'D'F'E'*, only the field scattered by the rough surface exists. The incident fields are enforced at the four TF/SF interfaces *A'F'*, *F'E'*, *E'B'* and *B'A'*.

Also, as shown in Fig. 4.2, a period of rough surface is included in the computation domain. At its side boundaries *a'd'* and *b'c'*, the periodic boundary conditions, for E_z as an example, are enforced [57],

$$E_z(x_{b'c'}, y, t) = E_z(x_{a'd'}, y, t - L/v_x), \tag{4.2a}$$

$$E_z(x_{a'd'}, y, t) = E_z(x_{b'c'}, y, t + L/v_x), \tag{4.2b}$$

where $v_x = v/\sin\theta$ is the phase velocity in x direction, and θ is the incident angle. At normal incidence $\theta = 0$, we can simply set the nodal values of the fields on the periodic boundaries at left- and right-hand sides equal at every time step.

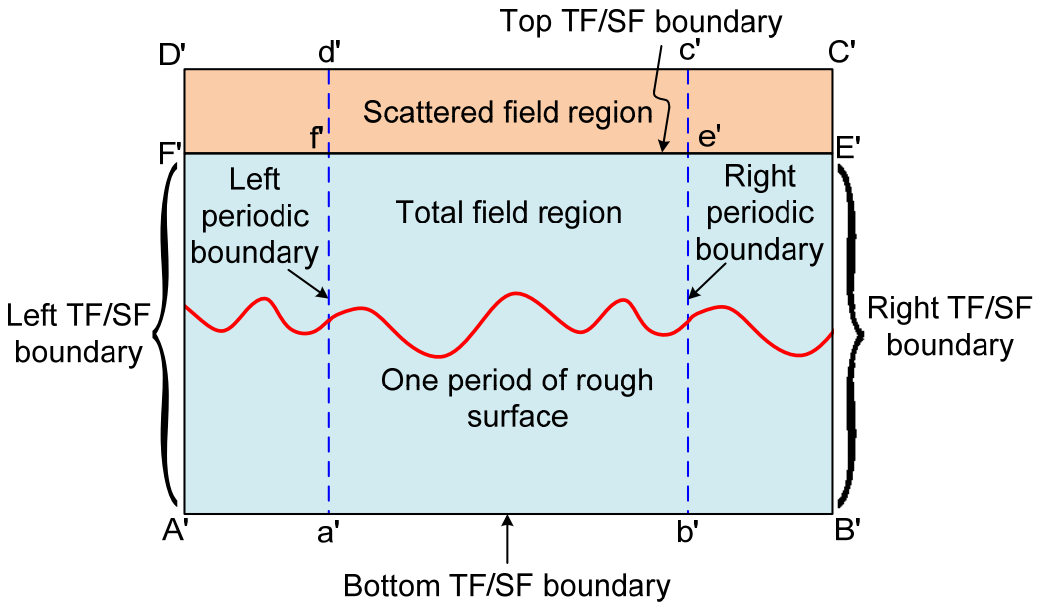

Fig. 4.2 The computation domain for a random periodic rough surface only (First step).

4.2 Computation Model for Scattering from Buried Cylinder below Random Periodic Rough Surface of Infinite Length

After placing a cylinder below a random periodic rough surface of infinite length, the structure is no longer periodic. Hence, the periodic boundary condition cannot be used anymore and the computation model must be modified. The new computation procedure is thus decomposed into two steps [16]. The key idea of the two-step approach is similar to that of a "three-wave" method presented in [58-60], which has been successfully used in the finite-difference time-domain (FDTD) analysis of scattering of an object buried below a planar media interface. As shown in [58], in such an FDTD analysis, first, the incident, reflected, and transmitted fields associated with the planar media interface are calculated in the absence of an object. Then, the calculated composite field (also called as the "three-wave" field), which is the sum of the incident and reflected

field in the upper half space and the transmitted field in the lower half space, is employed as the driving field of an object near the interface to determine the scattering of the object and interface combination. It is indicated in [58] that in principle, the interface involved in this approach that consists of two steps may be of any geometry; but one understands that if the media interface is a random rough surface instead of a planar surface, the scattered field by the rough surface, rather than the reflected and transmitted field associated with a planar interface, should be calculated first. Based on this key idea, the computation presented in this paper is performed in two steps. In the first step, the scattering of a random periodic rough surface is computed in the absence of an object so that the periodic boundary condition can still be used to confine the computation domain in a finite region. The computation domain for this step is the same as that depicted in Fig. 2, and the MPSTD algorithm is employed to compute the near-zone field, which is the sum of the incident field and the scattered field from the rough surface. In the second step, a cylinder is placed below the rough surface and the near-zone field obtained in the first step is used together with the incident field to excite the buried cylinder and the interaction between the buried cylinder and the rough surface is taken into account. In the first step, only the random rough surface is considered and the computation model is the same as that depicted in Fig. 4.2. The near-zone field obtained is the sum of the incident field and the scattered field due to the rough surface. In the second step, the buried cylinder is placed below the rough surface; and the computation domain is shown in Fig. 4.3, where the total field (TF) region is enclosed by *abef*, and the region outside *abef* is defined as the scattered field (SF) region. The dimensions of *abef* and *fecd* are the same

as that of $a'b'e'f'$ and $f'e'c'd'$ depicted in Fig. 4.2, respectively, and the boundaries *ad*, *bc* and *fe* correspond to $a'd'$, $b'c'$ and $f'e'$ used in Fig. 4.2.

Then, the near-zone field obtained in step 1 is used together with the incident field in the second step as the excitation source to the buried cylinder, which is injected on the TF/SF boundaries. The source introduced at the top and bottom TF/SF boundaries are the incident field used in step 1. However, the source enforced at the left and right boundaries are the near-zone field obtained in step 1. In this way, the near-zone field in the region enclosed by $a'b'c'd'$ from step1 can be transported to the region enclosed by *abcd* in step 2.

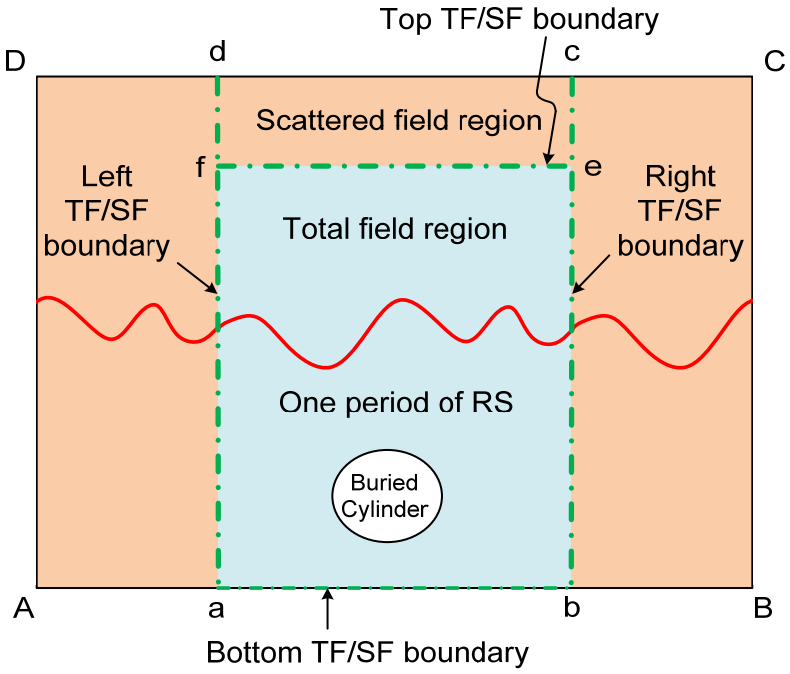

Fig. 4.3 The computation domain for cylinder buried below a random periodic rough surface (Second step).

As the buried cylinder is included, the incident field excites the random rough surface first, and the field scattered by the rough surface is calculated in step 1. Then, the cylinder is excited by the near-zone field obtained in step1. In turn, the field scattered by

the object will excite the rough surface and their interactions starts from there. The field in the total field region enclosed by *abef* is the sum of (a) the incident field, (b) the scattered field from rough surface alone excited by incident wave, (c) the scattering due to the buried cylinder excited by the near-zone field obtained in step1, and (d) the scattering due to the interaction between the cylinder and the rough surface. The fields existing in the total-field and scattered-field regions in steps 1 and 2 are illustrated in Figs. 4.4(a) and 4.4(b). One notes that among the three components of the scattered fields, part (b) - the scattered field from the random periodic rough surface alone is indeed from the *entire* periodic structure due to the application of PBC based on Floquet theorem; and hence part (c) - the scattering from the buried cylinder is due to the excitation from the *entire* random periodic rough surface. Only part (d) - the interaction between the buried cylinder and the random periodic rough surface is an approximation - it is taken to be for one period of the rough surface that is right above the buried cylinder only; the interaction between the buried cylinder and the other parts of the rough surface is neglected due to the requirement that the computation domain must be finite. Therefore, it is important to have the length L of one period of the random periodic rough surface to be sufficiently large compared with the size of the buried cylinder so that the interaction between the cylinder and the other periods of the rough surface, which are at larger distances away from the cylinder, is weaker; and hence can be neglected as a good approximation. This is to be demonstrated in a numerical example presented in Section 4.3. In addition, L must be much greater than the correlation length l_c to simulate the statistic characteristics of the roughness of a random rough surface as mentioned before.

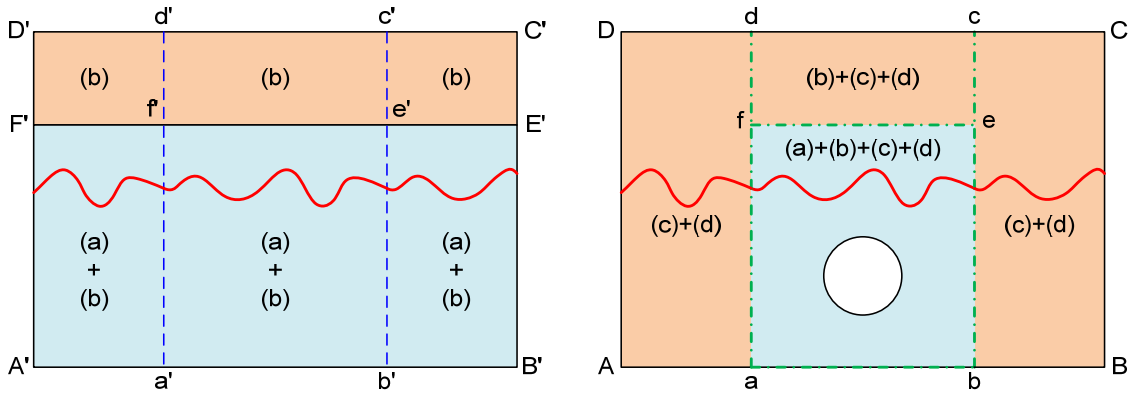

(a) (b)

Fig. 4.4 Illustration of the fields in the TF and SF regions

(a) Step 1, (b) Step 2.

4.3 Numerical Results and Discussion

Using the two-step approach formulated above, sample numerical results are presented and analyzed. For all the numerical results presented, the excitation is taken to be a normal TM_z plane wave incidence propagating along $-y$ direction, the time domain function of which is the first derivative of Blackmann-Harris window function with central frequency $f = 100MHz$. The random periodic rough surface is of period $L = 8m$ $(2.67\lambda_0)$ in parts (1) and (2) and of period $L = 10m$ $(3.33\lambda_0)$ in part (3), and the correlation length $l_c = 0.3m$ $(0.1\lambda_0)$, which satisfies the requirement $L \geq 15l_c$. It is of *rms* height $\sigma_{rms} = 0.3m$ $(0.1\lambda_0)$, unless otherwise specified. The medium above the rough surface is assumed to be free space and the medium below the rough surface is an isotropic, lossless medium with $\mu_r = 1$ and $\varepsilon_r = 3$, unless otherwise indicated. In all the computation domains presented in this section, the most outer subdomains are the PML regions. The statistic average of the scattering is taken for 15 – 18 realizations of the

random rough surface after a series of numerical tests as described in Chapter 3 to make sure that the results converge.

(1) Verification of the Periodic Boundary Condition and validation of the two-step approach

In the first numerical example, we consider a random periodic rough surface of infinite length alone. The computation domain is shown in Fig. 4.5(a), in which the total field region is the region $-6 \le x \le 6, -6 \le y \le 2$, and the scattered field exists in the region $-6 \le x \le 6, 2 \le y \le 4$. The left and right periodic boundaries are located at $x = -4$ and $x = 4$. Based on the Monte-Carlo statistic average of 15 rough surfaces, Fig. 4.5(b) shows the numerical results of the electric field observed at two different observation points $x = -4.2182$ and $x = 3.7818$ along y = 1, which are separated by a distance of the length of a period. From this figure, one sees that the fields at these two points are identical, which shows that the resulting fields are indeed periodic after applying the periodic boundary condition.

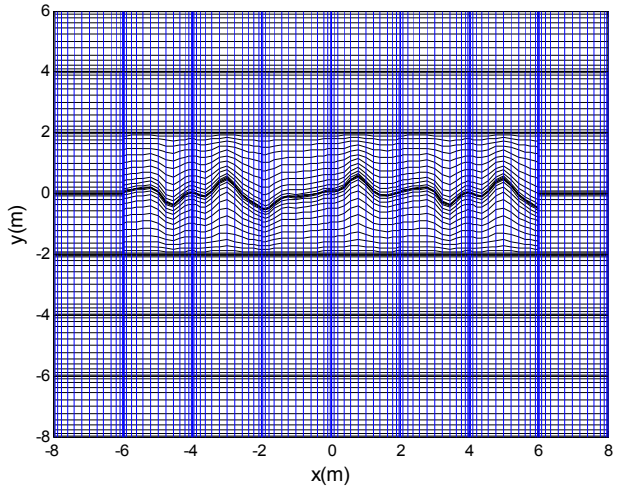

(a)

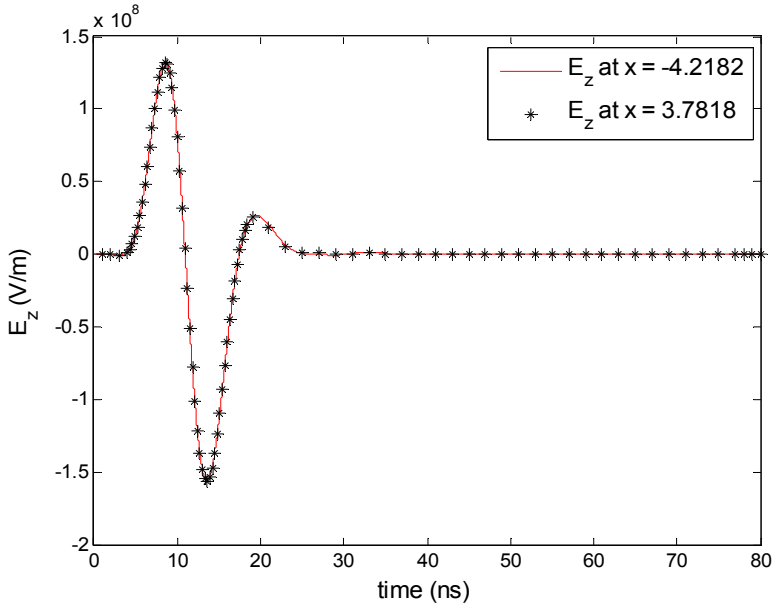

(b)

Fig. 4.5 Scattering from an infinite-long random periodic rough surface

(a) Computation domain,

(b) Fields observed at two points separated by a period of the rough surface.

The second example is devoted to validate the two-step MPSTD approach. Since there is not existing result in the literature for the same problem solved in this work, we employ the two-step approach to study a simpler geometry, which is a circular PEC cylinder buried below a random rough surface of finite length; and then compared the numerical results with published data. As shown in Fig. 4.6(a), the random rough surface exists in the region of $-4 \ll x \ll 4$, it becomes a flat interface for x<-4 and x>4. The numerical results of the electric field E_z obtained by employing the two-step approach is observed at (0, 2) and compared with the published data [61]. From the comparison illustrated in Fig. 4.6(b), one sees that the two sets of data fall on top of each other.

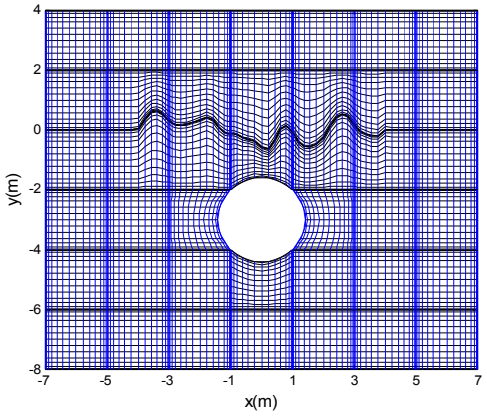

(a)

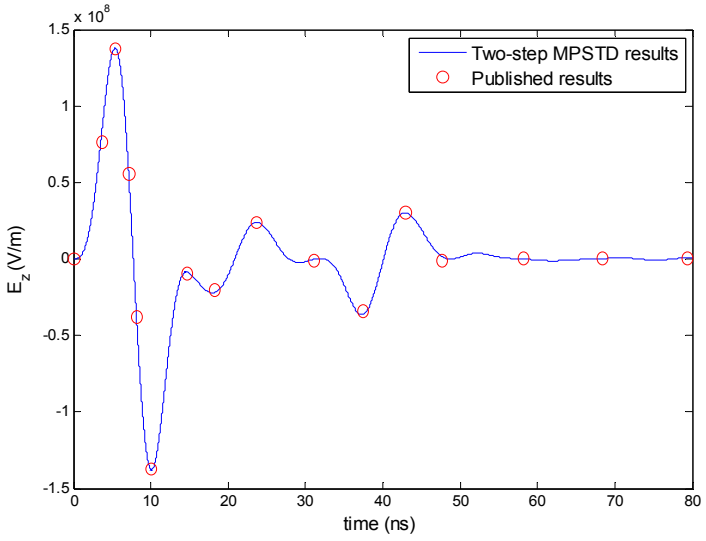

(b)

Fig. 4.6 Electric field at (0, 2) for a circular PEC cylinder buried below a random rough surface of *finite* length

(a) The computation domain,

(b) Comparison of the two-step MPSTD results with published data.

(2) Scattering from Random Periodic Rough Surface Alone

As a partial check of the two-step approach, in this section, we employ it to compute the fields due to a random periodic rough surface, in absence of the buried

cylinder, first. The geometry and the computation domain are the same as that illustrated previously in Fig. 4.5(a), hence is not repeated here. The periodic boundaries are enforced at $x=-4$ and $x=4$ in step 1 and the TF/SF boundaries are at $x=-4$ and $x=4$ in step 2. Since there is no buried cylinder, one would predict that the field in the total field region obtained in step 2 should be the same as that obtained in step 1; and no field should be found in the scattered field region in step 2 since there is no scatterer.

Numerical results of *spatial* distribution of the electric field obtained at a specific moment $t = 20ns$ in step1 and step 2 are shown in Figs. 4.7(a) and (b), respectively. The phenomena illustrated by the results shown are exactly as what is predicted above. The near zone field in step1 is successfully transferred to step 2 and no field exists in the scattered field region. In addition, it is of interest to note that the field distribution presented in both figures well represent the shape of the rough surface depicted in Fig. 4.5(a).

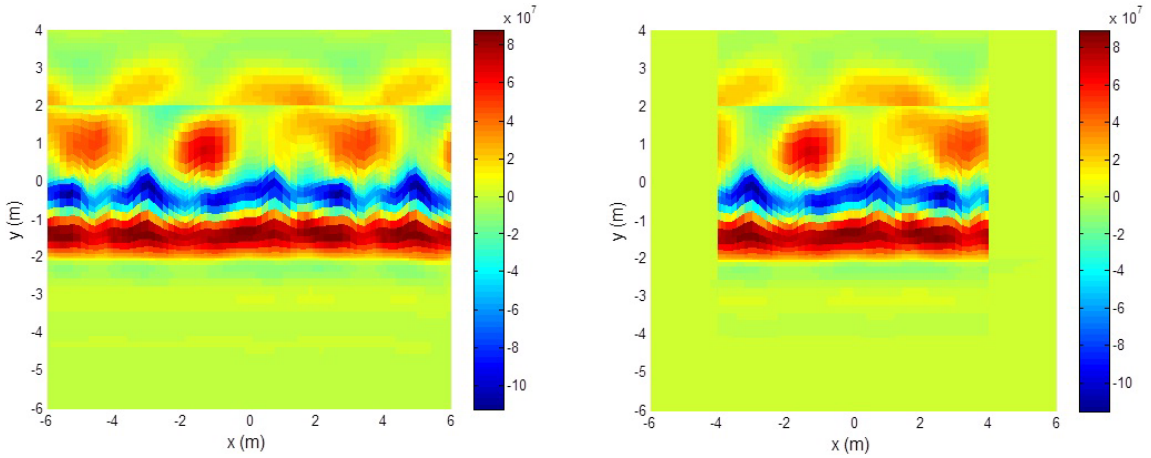

(a) (b)

Fig. 4.7 Spatial distribution of the electric field obtained at $t = 20ns$

(a) In step1, (b) In step2.

Then, in Fig. 4.8, we preset the same results but as a function of *time* observed at four observation points. At point (1, 1), which is in the total field region in both steps 1 and 2, the fields obtained in these two steps are exactly the same as expected. At (-1, 3) that is in the scattered field region in step 1 and is in the top scattered field region enclosed by *fecd* in step 2, the two sets of data also fall on top of each other as they are supposed to be. At points (-5, -5) and (5**,** 1), which are in the total field region in step 1 but in the left and right scattered field region in step 2, the scattered field obtained in step 2 is zero as expected since there is no scatterer. The observations made above can also serve as a partial check of the correctness of the numerical model developed.

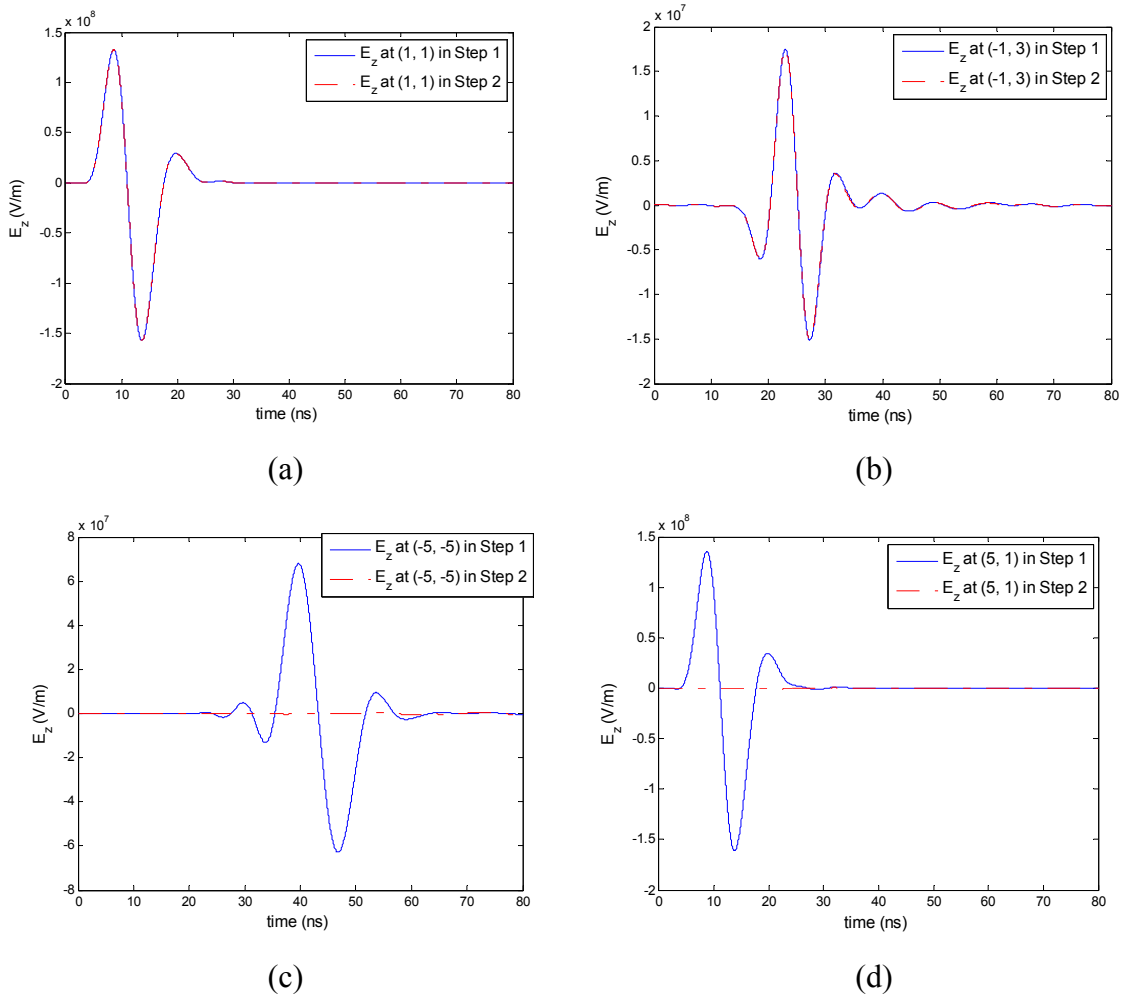

Fig. 4.8 Electric field as a function of time observed at different points in step1 and step 2.

Next, we present the numerical results corresponding to different lower medium ε_{r2} and various *rms* height σ_{rms}. The results shown in Fig. 4.9 are for the electric field fields observed at (0, 2) for $\varepsilon_{r2}=3$, $\varepsilon_{r2}=2$, and $\varepsilon_{r2}=1$. From the data presented, one notes that the electric filed gradually reduces to that in free space as ε_{r2} varies from 3, to 2, then 1; as expected.

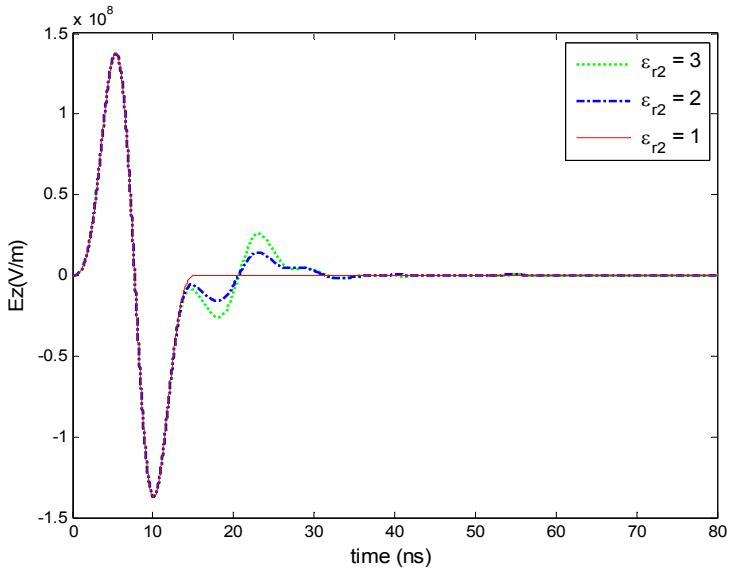

Fig. 4.9 Electric field at (0, 2) for different lower medium relative permittivities.

Fig. 4.10 illustrates the numerical results of the electric field observed at (0, 2) for various *rms* heights of the random rough surface, $0.3m\,(0.1\lambda_0)$, $0.2m\,(0.067\lambda_0)$, $0.1m$ $(0.033\lambda_0)$ and for a flat surface. From this figure, one sees that the result of the field gradually converges to the analytical result for a flat surface ($\sigma_{rms}=0$) as the *rms* height of the rough surface decreases from 0.3 to 0.2, to 0.1, and finally 0, as it is supposed to be. The observations made on the two examples above can serve as a partial check of the correctness of the numerical technique developed.

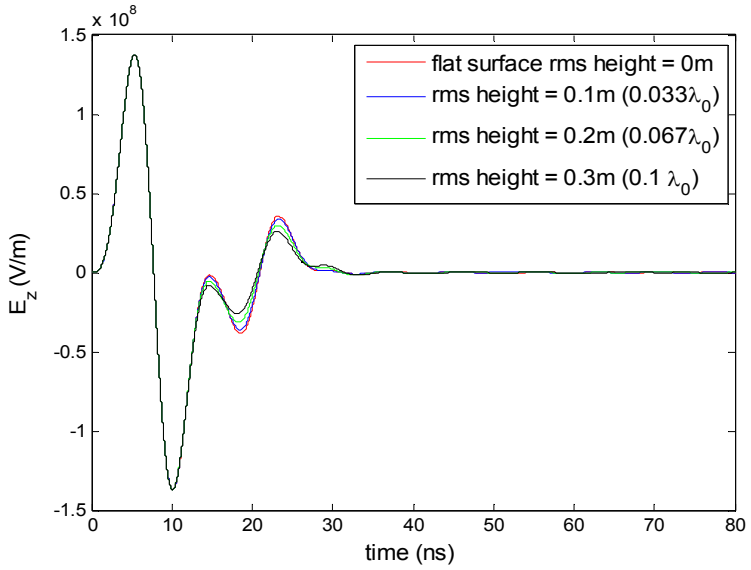

Fig. 4.10 Electric field at (0, 2) for various *rms* heights of the rough surface.

(3) Scattering from Buried Cylinder below a Random Periodic Rough Surface

In the next a few examples, we present the numerical results of the scattering of a circular PEC cylinder buried below a random periodic rough surface first. As indicated in the previous section, it is important to have the length L of one period of the random periodic rough surface to be sufficiently large compared with the size of the buried cylinder so that the interaction between the cylinder and the other periods of the rough surface, which are at larger distances away from the cylinder, is weaker; and hence can be neglected as a good approximation. This is demonstrated in a numerical example presented below. As illustrated in Figs. 4.11(a), 4.11(b), and 4.11(c), a period of the rough surface right above the buried cylinder is located in $-5 \le x \le 5$ and the length of a period $L = 10m$ remains unchanged; but the computation domain is taken to be of different lengths of 14m ($-7 \le x \le 7$), 18m ($-9 \le x \le 9$), and 22m ($-11 \le x \le 11$). The numerical results of the electric field observed at (0, 2), (-3, 2), and (-4, 2) are presented

in Figs. 4.11(d), 4.11(e), and 4.11(f), respectively; and in each of these three figures, the numerical results for the different computation domain lengths are compared with each other. The comparisons show that increasing the computation domain length beyond the period right above the buried cylinder has little effect on the numerical results. This demonstrates that the length of the period of the random periodic surface considered in the computation is sufficiently large so that the interaction between the buried cylinder and the other periods of the rough surface (x<-5 and x>5) can indeed be neglected and the total length of the rough surface included in the finite computation domain is adequate; hence verifies that the two-step MPSTD approach presented in Section 2 works effectively for a random periodic rough surface with a period of sufficiently large length.

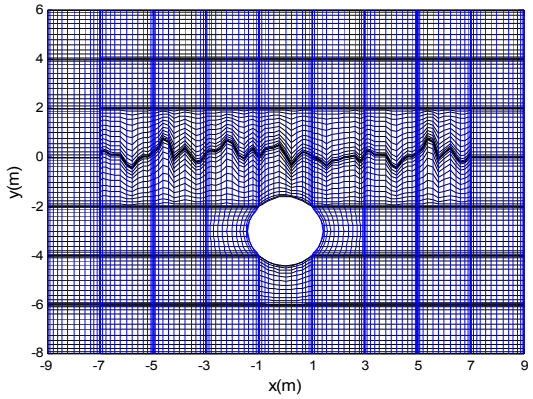

(a)

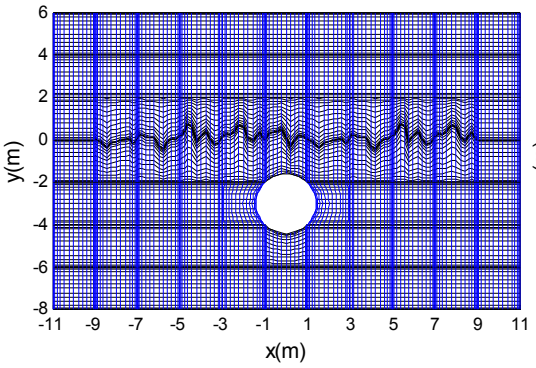

(b)

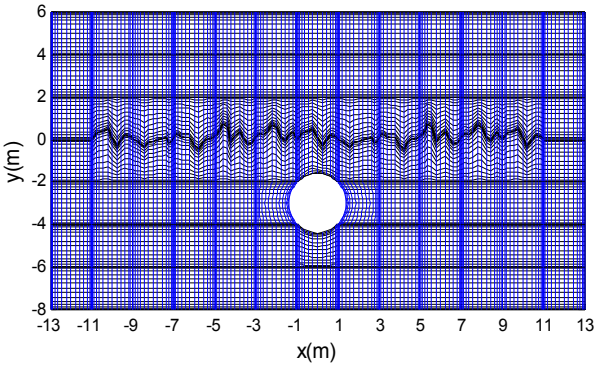

(c)

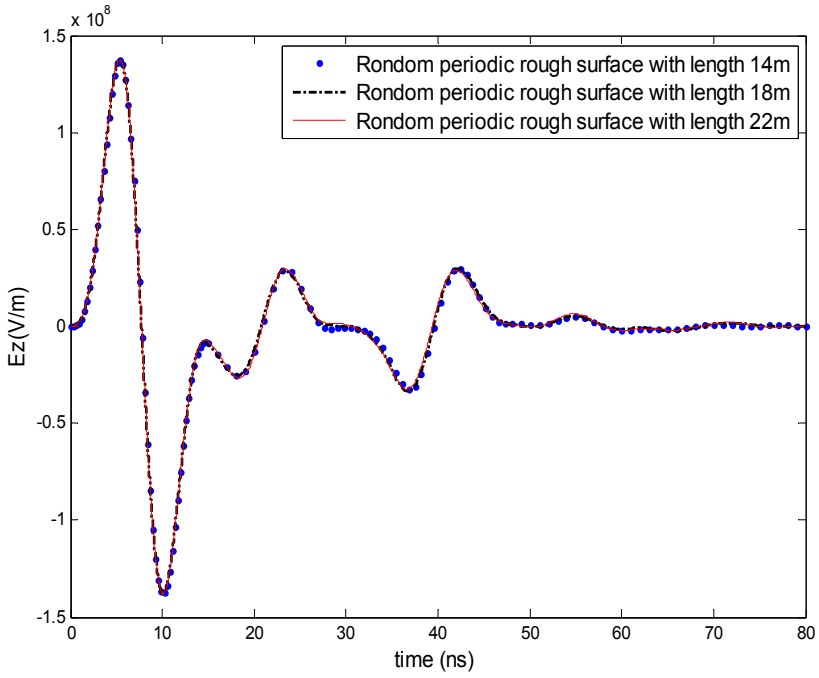
x 10^8
1.5
1
0.5
0
-0.5
-1
-1.5
Ez(V/m)
0
10
20
30
40
50
60
70
80
time (ns)
Rondom periodic rough surface with length 14m
Rondom periodic rough surface with length 18m
Rondom periodic rough surface with length 22m

(d)

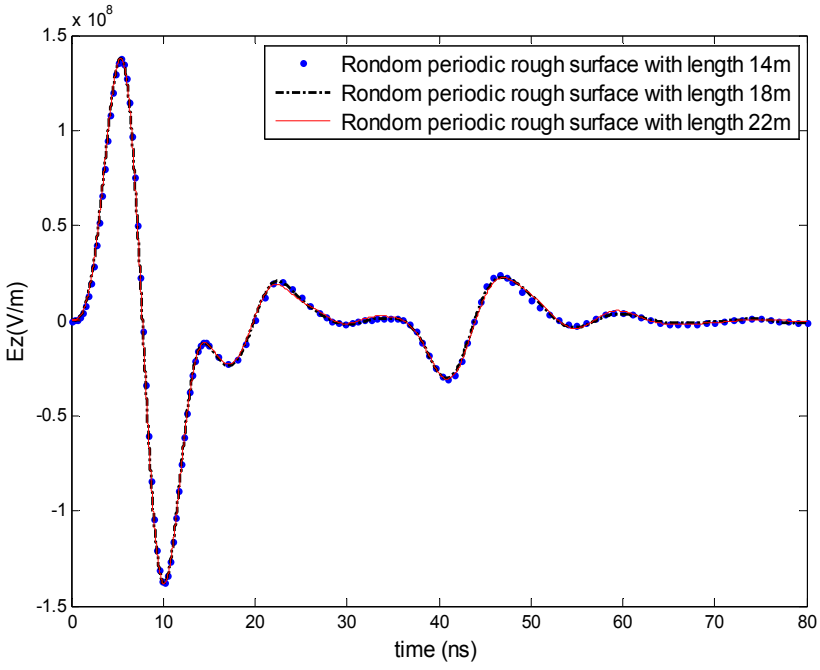
x 10^8
1.5
1
0.5
0
-0.5
-1
-1.5
Ez(V/m)
0
10
20
30
40
50
60
70
80
time (ns)
Rondom periodic rough surface with length 14m
Rondom periodic rough surface with length 18m
Rondom periodic rough surface with length 22m

(e)

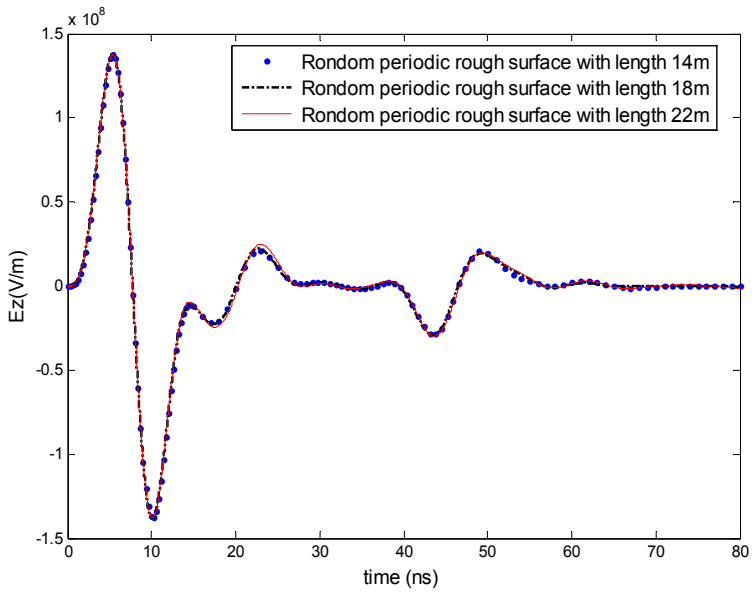

(f)

Fig. 4.11 Comparison of the numerical results for different computation domain lengths

(a) Computation domain of length of 14m, (b) 18m, (c) 22m,

(d) Comparison of the results at (0, 2), (e) at (-3, 2), (f) at (-4, 2).

In addition, numerical tests have been performed to verify the effectiveness of the two-step approach as L increases. The results of the numerical tests show that using a laptop with an Intel Core i3 CPU processor, the CPU time needed for one realization is 10 minutes for $L = 10m$ and is 14 minutes as L is increased to $14m$. From the limited CPU time increase, it is expected that the two-step MPSTD method can also effectively work well for larger L.

Then, the spatial distributions of the electric field, for the configuration depicted in Fig. 4.11(a), obtained at $t = 20ns$, $26ns$, and $50ns$ are shown in Figs. 4.12 (a), (c), and (e); and the corresponding magnetic field distributions are depicted in Figs. 4.12 (b), (d), and (f). It is of interest to observe that the electric field distribution obtained at $t = 20ns$

shown in Fig. 4.12(a) clearly illustrates the shape of the random rough surface but it only depicts a portion of the buried cylinder. This is due to the fact that the incident field hits the random rough surface first and then the buried cylinder; and at $t = 20ns$ only a portion of the cylinder is illuminated by the incident wave. But as time progresses, the incident wave travel farther in the lower half space. At $t = 26ns$, the scattering from the random rough surface as well as the buried cylinder appears in the left and right scattered field region. At $t = 50ns$, the incident field covers the whole buried cylinder and hence its complete shape is well illustrated in Figs. 4.12 (e) and (f), as expected.

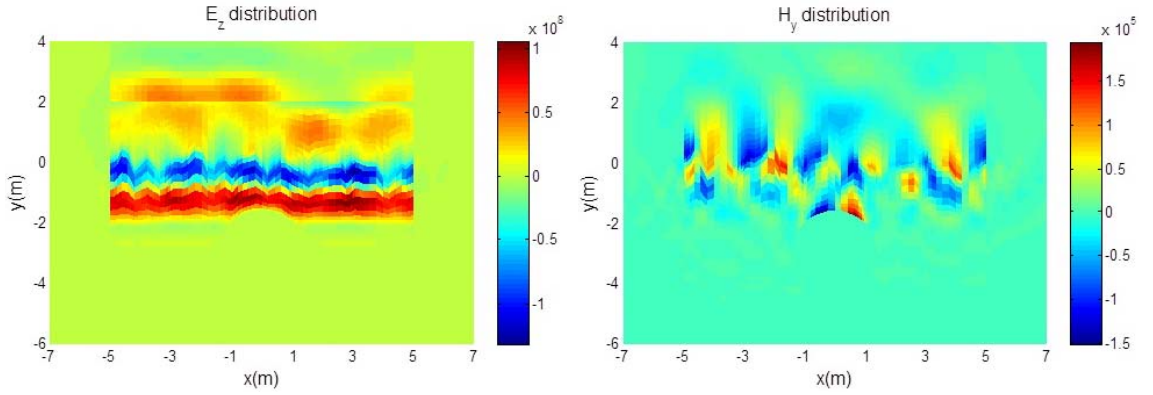

(a) (b)

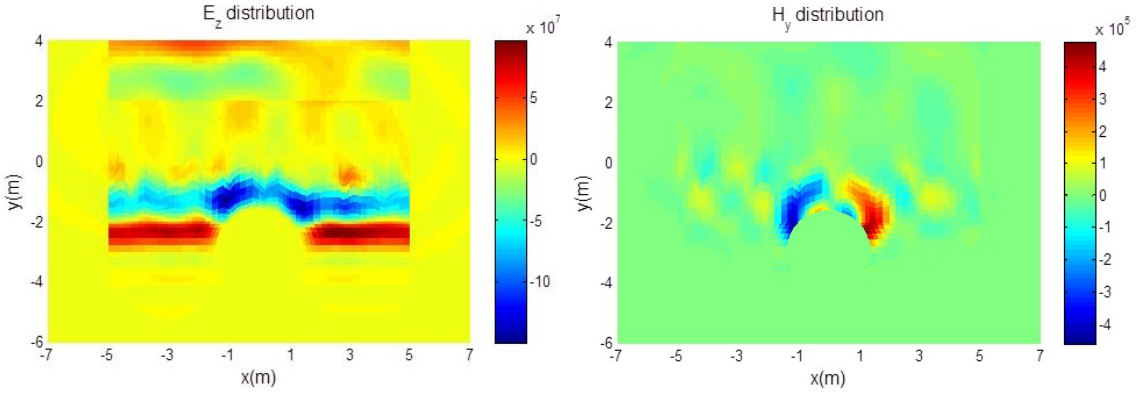

(c) (d)

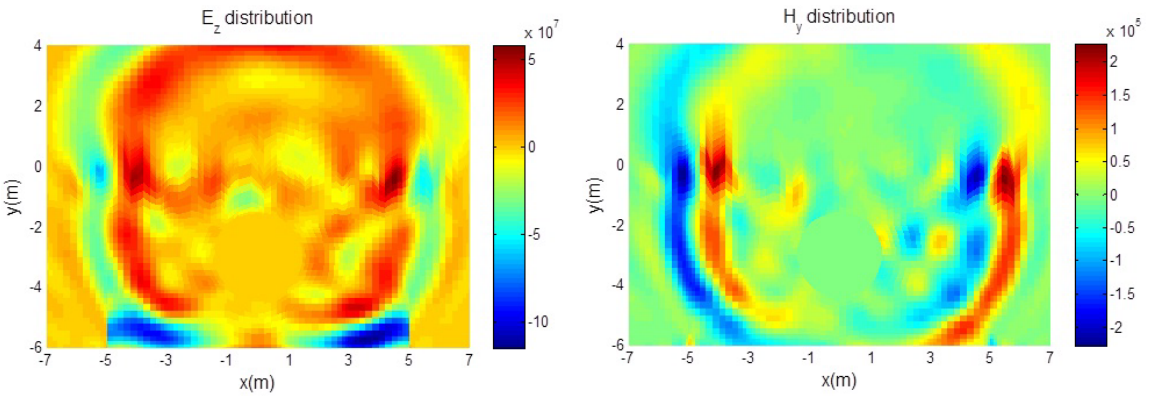

(e) (f)

Fig. 4.12 Spatial distribution of the fields obtained at different moments

(a) Geometry and computation domain,

(b) E_z at $t = 20ns$, (c) H_y at $t = 20ns$, (d) E_z at t = $26ns$,

(e) H_y at t = $26ns$, (f) E_z at $t = 50ns$, (g) H_y at t = $50ns$.

As a partial check, next, we present the numerical results of the scattering corresponding to different relative permittivity ε_{r2} of the lower half space. As shown in Fig. 4.13(a), ε_{r2} can significantly alter the scattering, and as it changes from 3, to 2, then to 1.01, and finally to 1, the result converges to that in free space, which perfectly matches the analytic result presented in Fig. 4.13(b), as it is supposed to be.

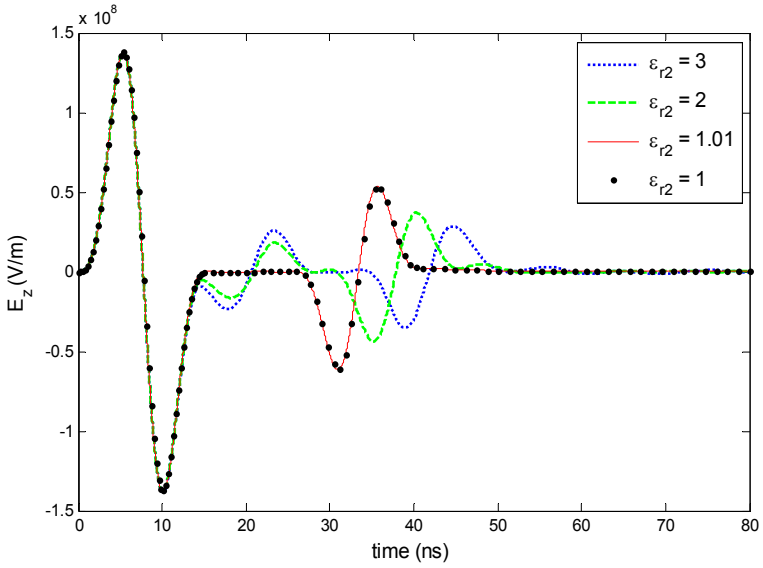

(a)

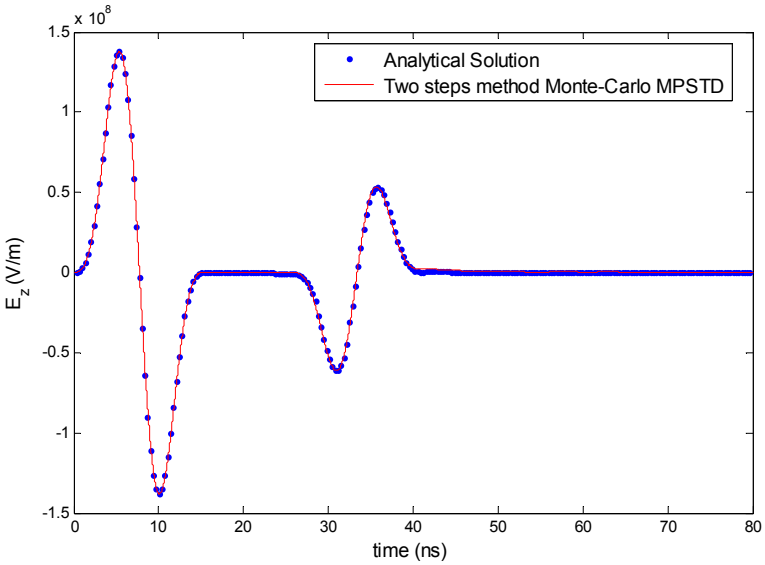

(b)

Fig. 4.13 Scattering of a circular PEC cylinder buried below a random peirodic rough surface of infinite length observed at (1, 2) for various ε_{r2}

(a) E_z observed for various ε_{r2} ,

(b) Comparison of the two step Monte-Carlo MPSTD result with analytical solution for $\varepsilon_{r2} = 1$.

Another partial check is performed by comparing the numerical result of the electric field obtained at (0, 2), which is in the middle of a period L of the random periodic rough surface with $L = 10m$ as depicted in Fig. 4.11(a), with that observed at the same point for a random rough surface of finite length L, beyond the two ends of which is a flat interface (x<-5 and x>5), that is not a periodic structure. For a sufficiently large L compared with the dimension of the buried cylinder, one would expect that the two results should be about the same. This is exactly what is illustrated in Fig. 4.14.

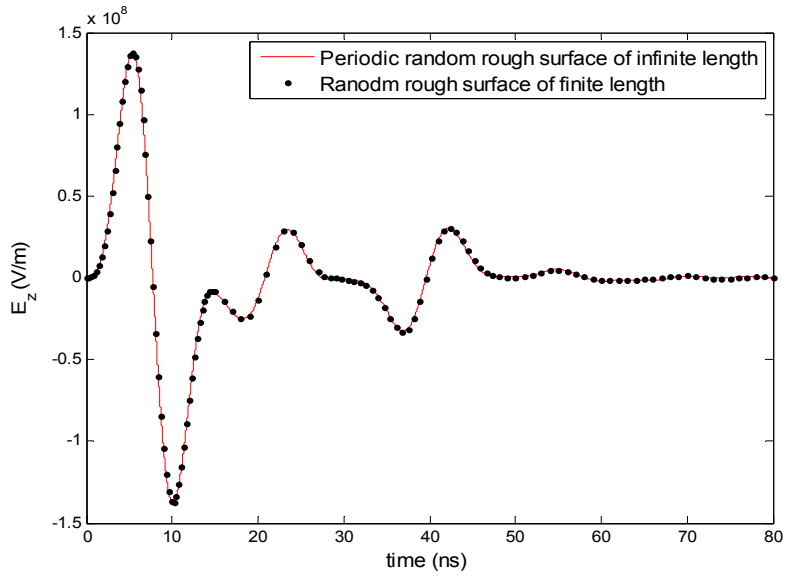

Fig. 4.14 Comparison of E_z at the middle point (0, 2) of a period of a random periodic rough surface with that for a random rough surface of finite length.

Next, we compare the two sets of data at a same point (4.434, 2), which is close to the right end of a period of the random periodic rough surface. The comparison presented in Fig. 15 shows a significance difference (the maximum difference is about 110%) of the scattering corresponding to the random periodic rough surface and that of finite length. This is due to the fact that the scattering observed at a point near the end of a period

contains the contribution from the adjacent period of the rough surface, which does not exist for a random rough surface of finite length. Such a significance difference between the two sets of numerical results indicates that it is necessary to extend the analysis of scattering involving a random rough surface of finite length to cover the more realistic case, in which a random periodic rough surface is considered.

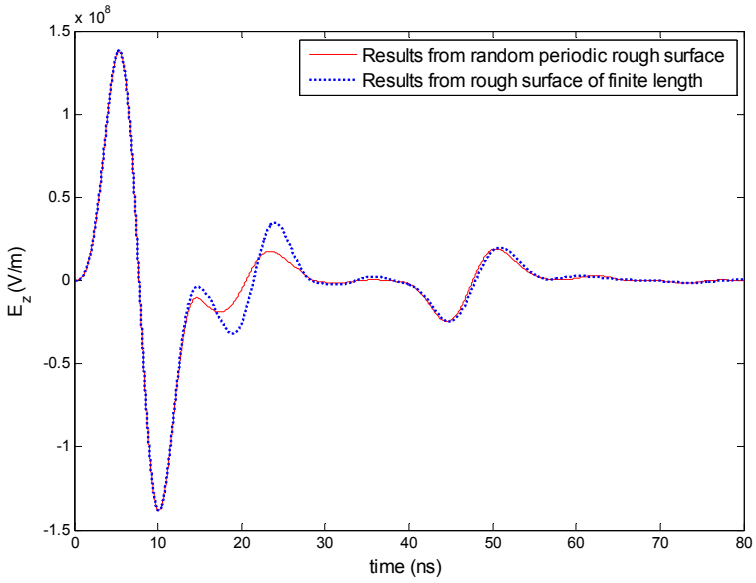

Fig. 4.15 Comparison of E_z at (4.434, 2) near the end point of a period of a random periodic rough surface with that for a random rough surface of finite length.

In Fig. 4.16, the numerical results of the electric field corresponding to various *rms* height σ_{rms} of the random rough surface are presented. As illustrated in Fig. 4.16(a), when σ_{rms} varies from 0.3, to 0.2, then to 0.1, and finally to 0, the result converges to that for a flat media interface. Furthermore, as shown in Fig. 4.16(b), the results obtained by the two-step approach for the flat interface is exactly the same as that got from the "regular" MPSTD technique presented in Chapter 3, as expected.

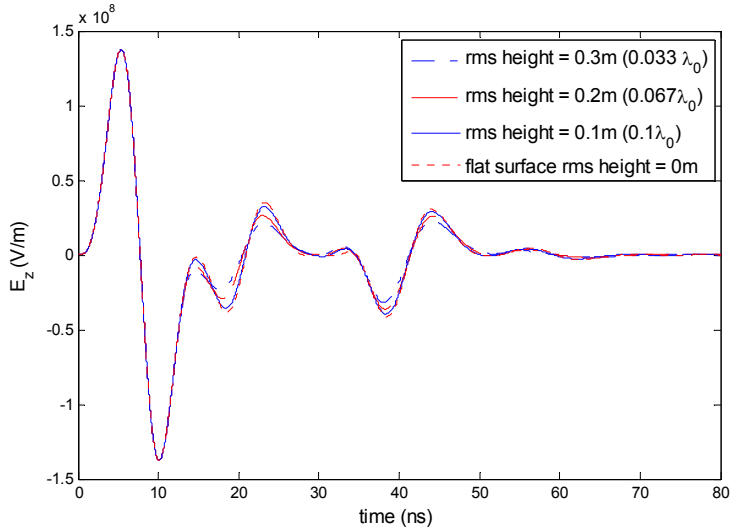

(a)

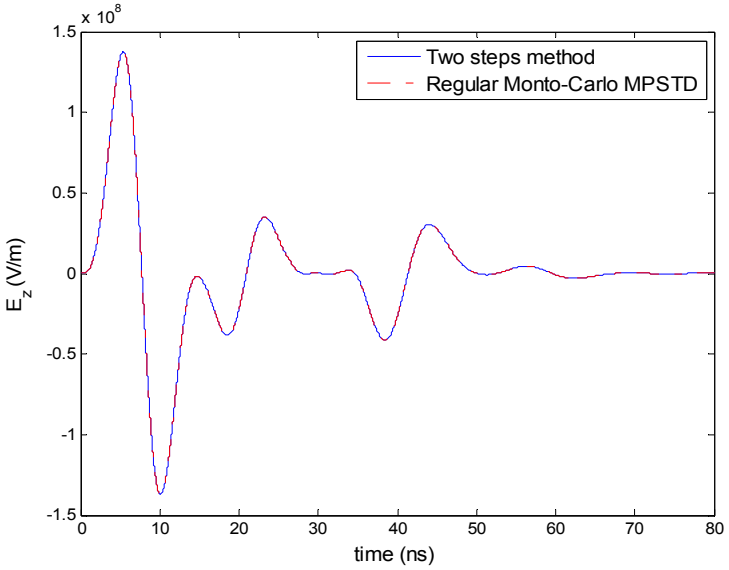

(b)

Fig. 4.16 Scattering of a circular PEC cylinder buried below a random peirodic rough surface of infinite length observed at (-3, 2) for various σ_{rms}

(a) E_z observed for various σ_{rms},

(b) Comparison of the results obtained by two different methods for a flat interface.

The two-step Monte-Carlo MPSTD numerical technique developed in this work can be employed for determining the scattering of a cylinder of arbitrary shape buried below a random periodic rough surface of infinite length. The last sample numerical result is for the scattering of a rectangular PEC cylinder of dimension $2m \times 2m$ $(0.67\lambda_0 \times 0.67\lambda_0)$ with its axis along (0, -3) buried below a random periodic rough surface of infinite length. The geometry and computation domain with grids are depicted in Fig. 4.17(a). In Figs. 4.17(b) and (c), the spatial distributions of E_z at two moments $t = 25ns$ and $t = 50ns$ are presented. Similar to what has been seen in Fig. 4.12, one observes that the electric field distribution obtained at $t = 25ns$ shown in Fig. 4.17(b) clearly illustrates the shape of the random rough surface but it only depicts a portion of the buried cylinder. This is due to the fact that the incident field hits the random rough surface first and then the buried cylinder; and at $t = 25ns$ only a portion of the cylinder is illuminated by the incident wave. But as time progresses, the incident wave travel farther in the lower half space. At $t = 50ns$, the incident field covers the whole buried cylinder and hence its complete shape is well illustrated in Fig. 4.17(c).

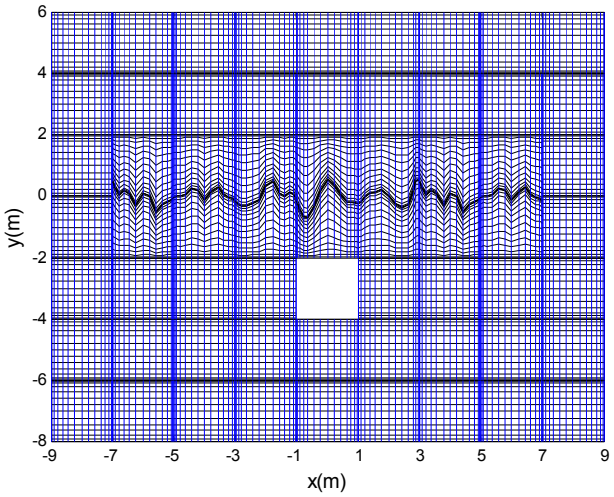

(a)

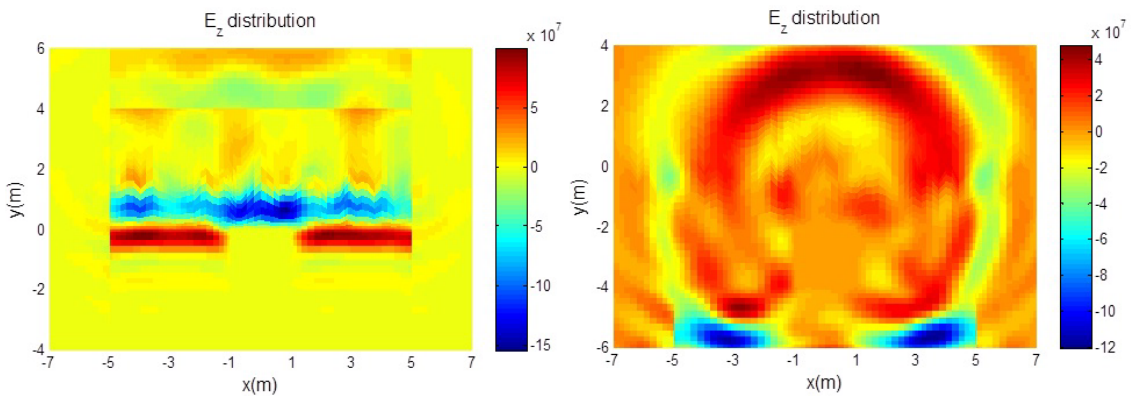

(b) (c)

Fig. 4.17 Spatial distribution of E_z obtained at different moments

(a) Geometry and computation domain, (b) E_z at t = 25ns, (c) E_z at t = 50ns.

The benefit of using the two-step approach is described as the follows. As shown in previous subsection 4.2, after placing a cylinder below the random periodic rough surface, the structure is no longer periodic and the periodic boundary condition (PBC) does not hold any more, hence it is hard to solve this problem within a finite computation domain. To overcome this difficulty, we decompose the solution of this complicated problem into two steps. In the first step, only the random rough surface is considered so that the PBC still holds and hence can be enforced to simulate the entire random periodic rough surface by only one period of the rough surface contained in a finite computation domain. Then, in the second step, the near-zone field obtained in the first step is used together with the incident field as the excitation source to the buried cylinder to determine the electromagnetic fields taking into account the scattering of the buried cylinder as well as the interaction between the buried cylinder and the rough surface.

CHAPTER FIVE

SCATTERING OF CYLINDERS EMBEDED IN LAYERED LOWER HALF SPACE WITH RANDOM ROUGH SURFACES

In the previous chapters, scattering of cylinder buried below a random rough surface has been studied. However, in reality, the lower half space may consist of stratified media. Therefore, in this chapter, the study is extended to the scattering of cylinders embedded in the lower half space of two layers, under plane wave incidence. The two-half-space interface is taken to be a random rough surface of finite length or with extensive periodic structure. The interface separating the two layers inside the lower half space is assumed to be planer surface or random rough surface of finite length. Correspondingly, the composite field in the layered structure driving the scattering of the buried cylinder is formulated and calculated. To validate this formulation, transmission-line theory is employed to simulate the wave propagation in the layered structure. The analysis of scattering of cylinders embedded in such a layered structure employs the Monte-Carlo MPSTD method presented in Chapter 3. In particular, for the analysis involving a random rough surface with extensive periodic structure, the two-step approach developed in Chapter 4 is used. Sample numerical results are presented and analyzed.

5.1 Formulation of the Incident Composite Field in the Layered Structure

As presented in Chapter 3, the incident wave driving the scattering of a buried cylinder is calculated by a "three-wave approach". The driving incident wave is the composite of the initial incident, reflected, and transmitted waves. However, different

from the model shown in Fig. 3.4, in this chapter, the lower half space consists of two layers separated by a planer surface or a random rough surface as illustrated in Fig. 5.1. The three regions depicted in this figure are all assumed to be lossless, nonmagnetic and homogeneous media characterized by (μ_0, ε_0), (μ_0, ε_1) and (μ_0, ε_2) respectively, where $\varepsilon_i = \varepsilon_{ri}\varepsilon_0$ $(i = 1,\ 2)$. Also shown in Fig. 5.1, two virtual planar interfaces are placed at $y = 0$ and $y = -d$ along the rough surfaces, respectively. The random rough surfaces just cause additional inhomogeneities above/below the virtual planar interfaces; and these inhomogeneities can be treated as "additional scatterers" touching the virtual planar surfaces, illuminated by the composite fields.

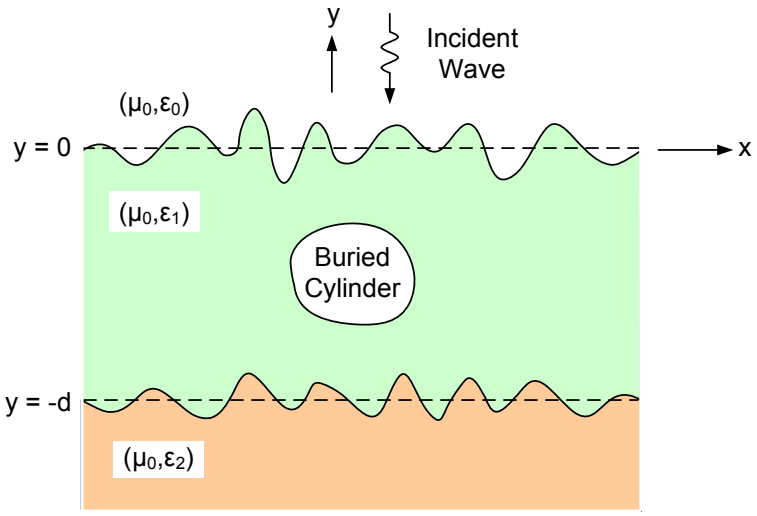

Fig. 5.1 Cylinder embedded in a layered half space.

This structure with two virtual planar surfaces at $y = 0$ and $y = -d$ is similar to a dielectric slab $(-d \le y \le 0)$, but the regions above and below it have different electromagnetic properties. Note that there are multiple reflections inside the slab $(-d \le y \le 0)$. However, as stated in [62], since the interfaces are planar surfaces, the fields within the slab can be considered as upward- and downward-propagating plane

waves, which accounts for the effect of multiple reflections inside the slab. This idea can be utilized for the formulation of the composite field in the layered region.

Fig. 5.2 shows a TM_z time-harmonic plane wave propagating in the layered structure. As illustrated in this figure, in the upper half space which is assumed to be air, where $y > 0$, the field is due to the incident wave and the reflected wave from the virtual planar interface at $y = 0$. In the first layer of the lower half space $(-d < y < 0)$, there are upward- and downward-propagating waves that accounts for the multi reflections within this layer; while in the second layer of the lower half space ($y < -d$), there is only downward transmitted wave.

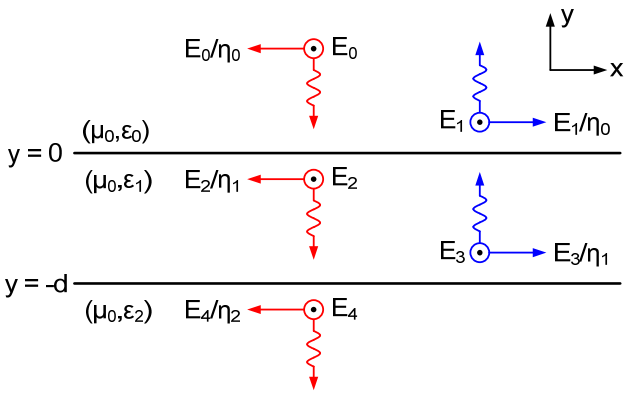

Fig. 5.2 A TM_z plane wave propagating in a layered structure.

Then, the frequency domain electric and magnetic field in each of the three regions can be expressed by

$$E_z = \begin{cases} E_0 e^{jk_0 y} + E_1 e^{-jk_0 y}, & y > 0 \\ E_2 e^{jk_1 y} + E_3 e^{-jk_1 y}, & -d < y < 0 \\ E_4 e^{jk_2 (y+d)}, & y < -d \end{cases} \tag{5.1}$$

$$H_x = \begin{cases} -\dfrac{E_0}{\eta_0} e^{jk_0 y} + \dfrac{E_1}{\eta_0} e^{-jk_0 y}, & y > 0 \\ -\dfrac{E_2}{\eta_1} e^{jk_1 y} + \dfrac{E_3}{\eta_1} e^{-jk_1 y}, & -d < y < 0 \\ -\dfrac{E_4}{\eta_2} e^{jk_2 (y+d)}, & y < -d \end{cases} \tag{5.2}$$

where E_0 is the complex amplitude of the incident plane wave, $k_0 = \omega\sqrt{\mu_0 \varepsilon_0} = \omega / c$ is the wave number in free space and $k_i = \sqrt{\varepsilon_{ri}} k_i \ (i = 1,\ 2)$ is the wave number in each layer of the earth. By enforcing the continuity of E_z and H_x at $y = 0$ and $y = -d$ and solving the resulting equations, the unknown field amplitudes $E_1,\ E_2,\ E_3$ and E_4 are determined as

$$E_1 = \frac{(n_1 - n_1 n_2)\cos(k_1 d) + j(n_2 - n_1^2)\sin(k_1 d)}{(n_1 + n_1 n_2)\cos(k_1 d) + j(n_2 + n_1^2)\sin(k_1 d)} E_0, \tag{5.3a}$$

$$E_2 = \frac{n_1 - 1}{2n_1} E_1 + \frac{n_1 + 1}{2n_1} E_0 \tag{5.3b}$$

$$E_3 = \frac{n_1 + 1}{2n_1} E_1 + \frac{n_1 - 1}{2n_1} E_0 \tag{5.3c}$$

$$E_4 = (\frac{n_1 - 1}{2n_1} e^{-jk_1 d} + \frac{n_1 + 1}{2n_1} e^{jk_1 d}) E_1 + (\frac{n_1 + 1}{2n_1} e^{-jk_1 d} + \frac{n_1 - 1}{2n_1} e^{jk_1 d}) E_0 \tag{5.3d}$$

where $n_i = \sqrt{\varepsilon_{ri}} \ (i = 1,\ 2)$ is the refractive index.

For the incident wave that is a function of time, such as the first derivative of Blackmann-Harris window function used in this research, the Fourier transform is used to find its spectrum. Then, using equation (5.3), the composite fields of each spectral component can be obtained. Finally, the time-domain composite fields are determined using the inverse Fourier transform.

The composite fields are calculated analytically at each grid point as needed [63] and validated prior to the execution of the Monte-Carlo MPSTD numerical technique.

5.2 Numerical Results and Discussion

For all the numerical results presented, the excitation is taken to be a normal TM_z plane wave incidence propagating in –y direction, the time domain function of which is the first derivative of Blackmann-Harris window function with central frequency $f = 100MHz$. A random rough surface of infinite length with extensive periodic structure is considered in parts (2) and (3). It has a period $L = 8m$ $(2.67\lambda_0)$ in part (2) and $L = 10m$ $(3.33\lambda_0)$ in part (3). In part (4), the two random rough surfaces are assumed to be of finite length $L = 10m$ $(3.33\lambda_0)$. All the random rough surfaces considered in the following examples have correlation length $l_c = 0.3m$ $(0.1\lambda_0)$, which satisfies the requirement $L \geq 15l_c$ and are of *rms* height $\sigma_{rms} = 0.3m$ $(0.1\lambda_0)$ unless otherwise specified.

(1) Validation of Formulation of the Incident Composite Field

To validate the formulation of the incident composite field, such calculated composite field is compared with the Advanced Design System (ADS) simulation results. The plane wave propagation with normal incidence in the layered structure, in which each layer is of infinite length, is a 1-*D* plane wave propagation problem. In this case, the wave equations have the same form as Telegraph equations of a lossless transmission line [64] with the following correspondence

$$(E, H) \leftrightarrow (V, I),$$
$$(\varepsilon, \mu) \leftrightarrow (C, L), \tag{5.4}$$

$$\beta \leftrightarrow \beta,$$

$$\eta \leftrightarrow Z,$$

where V and I are the voltage and current along the transmission line (TL), C and L are the capacitance and inductance per unit length, β is the propagation constant, and Z is the characteristic impedance of the transmission line. Therefore, the layered structure of infinite length can be transformed into a multi-section transmission-line model that can be simulated by a microwave circuit simulator, Agilent Advanced Design System (ADS) or AWR Microwave Office.

As shown in Fig. 5.3, the thickness of each of the three layers from top to bottom in the computation domain is taken to be $2m$, $6m$ and $2m$, respectively. The two-half-space interface is located at $y = 0$ and the interface separating the two layers in the lower half space is at $y = -6$. The observation points are on $y = 1$, $y = -1$ *and* $y = -7$ planes in each of the three layers, marked in red dash lines. The composite fields calculated at these observation points using the formulas derived above are compared with the corresponding ADS results in Fig. 5.4. The comparison shows a perfect match between these two sets of data, which validates the correctness of the formulation of the composite field in the layered structure.

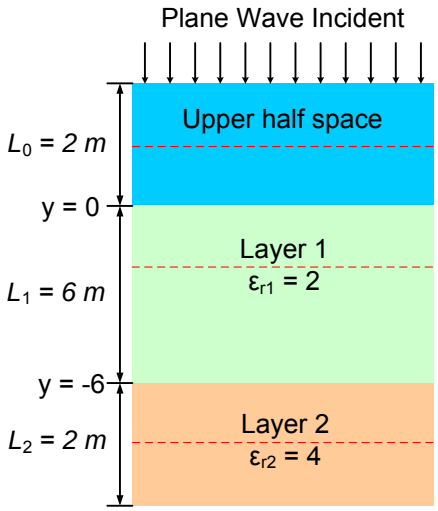

Fig. 5.3 Three-layer structure illustration.

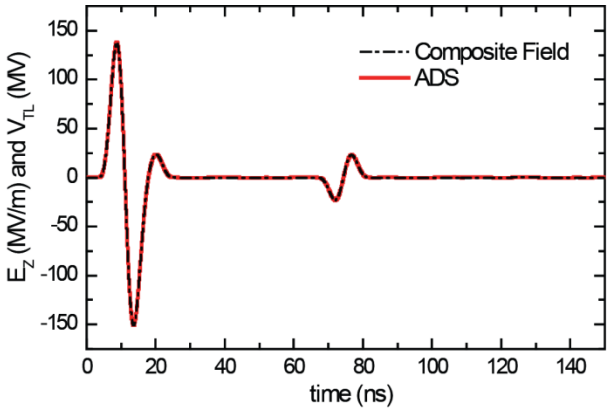

(a)

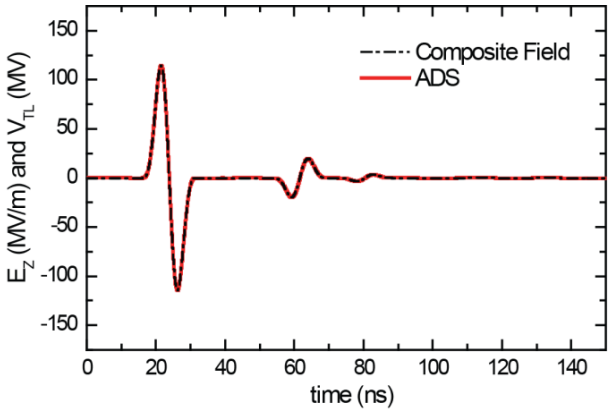

(b)

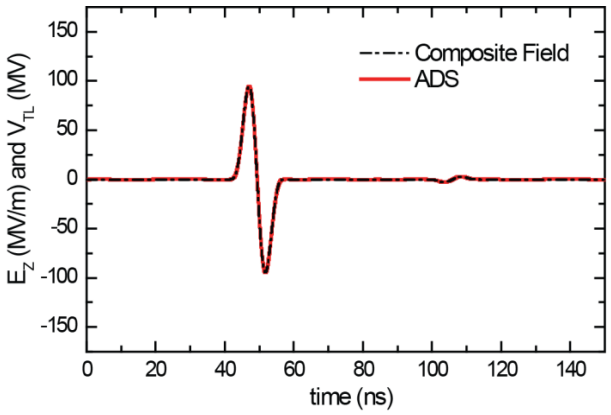

(c)

Fig. 5.4 Comparison of the calculated composite fields E_z in a layered structure with the corresponding ADS results of transmission line (TL) voltage

(a) At $y = 1$, (b) At $y = -1$, (c) At $y = -7$.

(2) Results of Scattering by the Layered Structure without Buried Object

To further validate the incident composite fields formulated above, it is used in the Monte-Carlo MPSTD analysis for determining the scattering by the layered structure in absence of embedded object. The computation domain is shown in Fig. 5.5(a). The first media interface is a random rough surface along $y = 0$ and the second interface is a planar interface at $y = -6$. The scattered field (SF) region is the region where $2 \le y \le 4$ and the total field (TF) region is $-8 \le y \le 2$, which contains three layers. In the first example, we choose $\varepsilon_{r1} = 1.04$, $\varepsilon_{r2} = 1.02$ for the two layers in the earth so that the whole space is very close to a homogeneous free space region characterized by $\varepsilon_r = 1$. For such a layered structure, the MPSTD computation results of the total fields observed at (5, 2) and (-1, -7) are compared with that obtained in free space. The comparison is presented in Figs. 5.5(b) and (c) where an excellent agreement is observed.

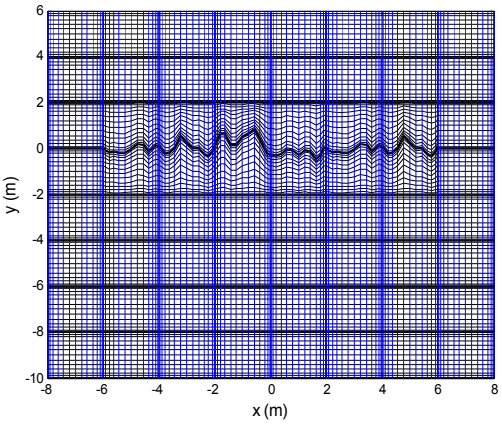

(a)

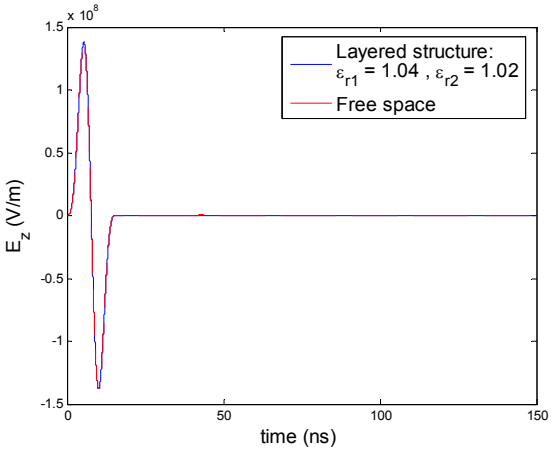

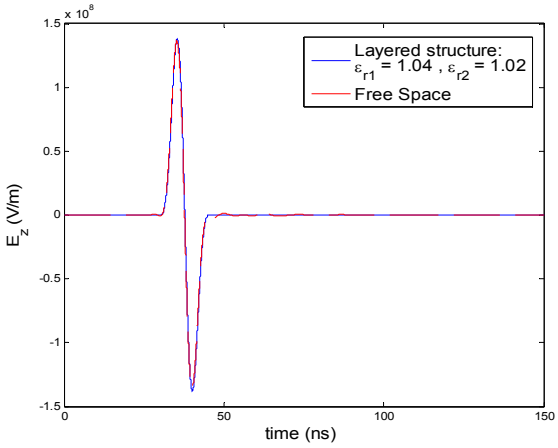

(b) (c)

Fig. 5.5 The total fields in a layered structure with $\varepsilon_{r1} = 1.04,\ \varepsilon_{r2} = 1.02$

(a) The computation domain, (b) E_z at (5, 2) compared with the free space result,

(c) E_z at (-1, -7) compared with the free space result.

(3) Results of Scattering by a Circular PEC Cylinder Embedded in a Layered Lower Half Space with a Random Periodic Rough Surface and a Planar Interface

In this section, results of the scattering of a circular PEC cylinder buried in the upper layer of the lower half space, as shown in Fig. 5.6(a), are presented. The random

rough surface is with extensive periodic structure. Hence the two-step Monte-Carlo MPSTD approach formulated in Chapter 4 is employed. The TF and SF regions used in the MPSTD approach are the same as that specified in the previous subsection (2).

First, we consider the cylinder embedded in a layered earth with $\varepsilon_{r1} = 3$ and ε_{r2} varying from 2, to 2.5 and then 2.9. Results of the total field observed at (0, 2) corresponding to the varying ε_{r2} are plotted in Fig. 5.6 (b) and compared with the results obtained for the cylinder buried in a two-half-space region where $\varepsilon_{r\_upper} = 1,\ \varepsilon_{r\_lower} = 3$. To clearly illustrate the trend of the change of the field as ε_{r2} varies, the plot in the vicinity of *t = 86ns* is enlarged in Fig. 5.6 (c). From these two figures, one observes that as ε_{r2} varies from 2, to 2.5 and then 2.9, the computation results of the field gradually approach to the two-half-space results for $\varepsilon_{r\_lower} = 3$, as expected.

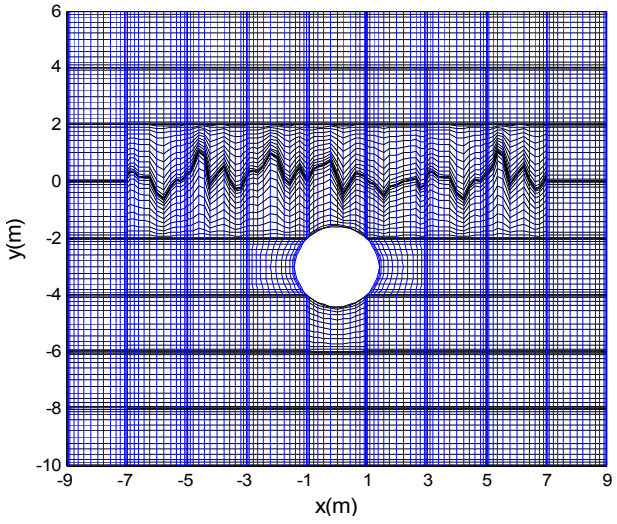

(a)

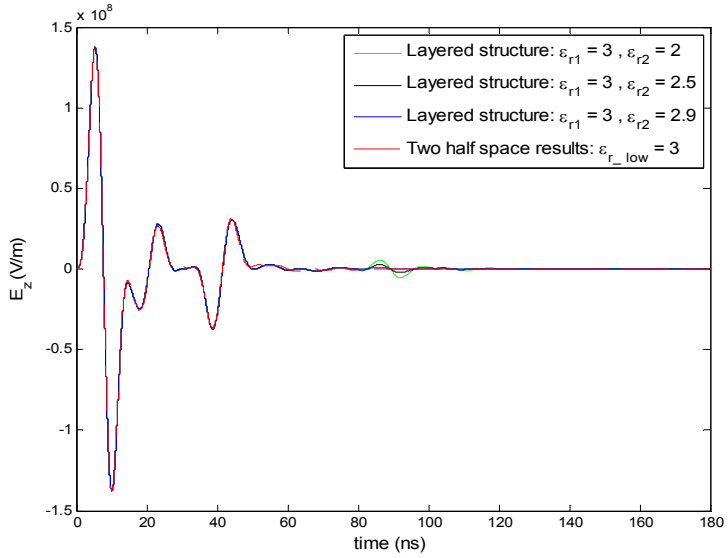

(b)

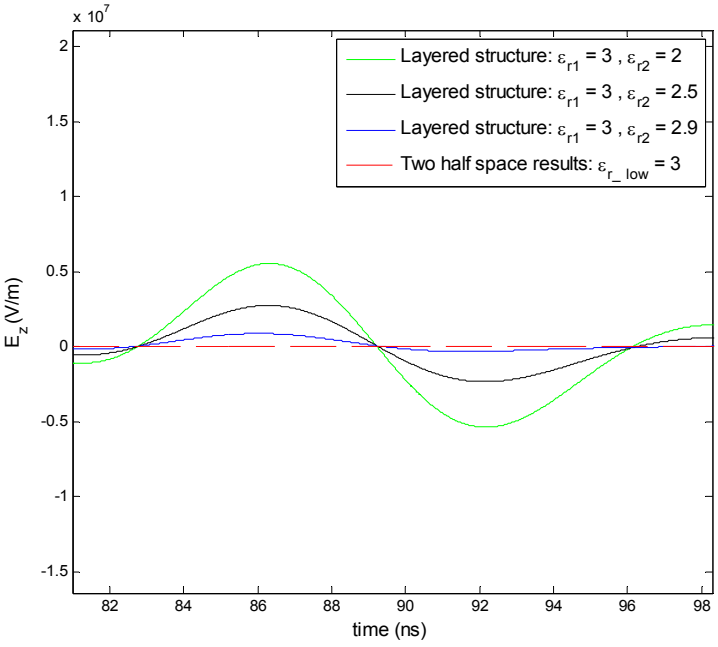

(c)

Fig. 5.6 Scattering of a circular PEC cylinder embedded in the first layer of the lower half space with a random periodic rough surface and a planar interface, for various ε_{r2}

(a) Computation domain and geometry,

(b) E_z at (1, 2) compared with the two-half-space result,

(c) Close-up view of (b) in the vicinity of $t = 86ns$.

Next, we consider scattering of the cylinder embedded in a layered lower half space with $\varepsilon_{r1} = 4$ and $\varepsilon_{r2} = 1.5$. The computation domain and geometry are the same as that shown in Fig. 5.6(a), the observation point is located at (1, 2). The result is compared with the two-half-space case in which $\varepsilon_{r\_upper} = 1$, $\varepsilon_{r\_lower} = 3$, and the comparison is illustrated in Fig 5.7. The difference between the two sets of data shown in this figure represents a significant influence from the layered structure of the lower half space on the scattering.

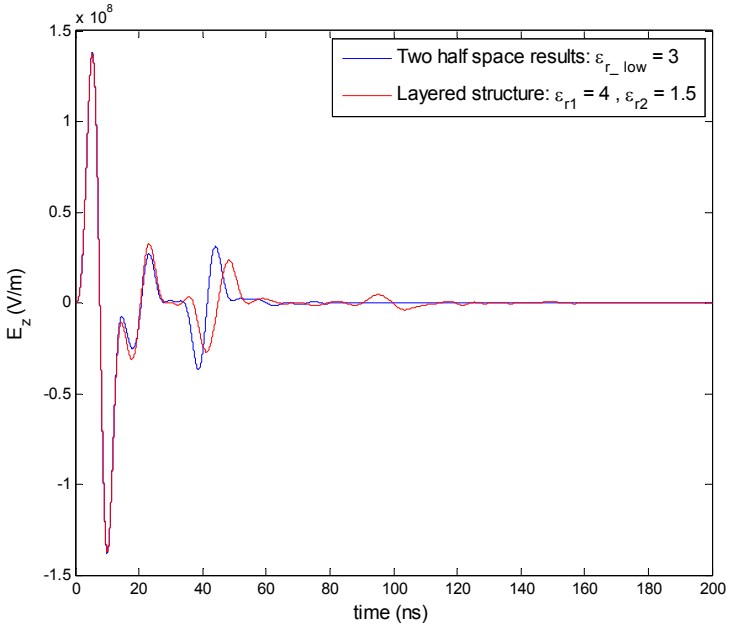

Fig. 5.7 Scattering of a circular PEC cylinder embedded in the first layer of the lower half space with a random periodic rough surface and a planar interface compared with two-half-space result.

(4) Results of Scattering of Cylinders Embedded in a Layered Lower Half Space Involving Two Random Rough Surfaces of Finite Length

In this section, the two-half-space interface is taken to be a random rough surface of finite length *L=10m*. And the interface separating the two layers of the lower half space is assumed to be a random rough surface of the same length. The permittivities of the two layers are set to be $\varepsilon_{r1} = 4$ and $\varepsilon_{r2} = 2$. In the first example, the Monte-Carlo MPSTD is applied to obtain the scattering from the two random rough surfaces alone. The geometry and computation domain are depicted in Fig 5.8 (a). In Figs. 5.8 (b) and (c), the spatial distributions of E_z at two moments *t=20ns* and *t=55ns* are presented. One observes that the field distribution at *t=20ns* illustrates the shape of the upper rough surface. As time progresses, the incident wave travel farther in the lower half space. Then, both the scattering from the upper rough surface and the incident wave illuminate the lower rough interface. At *t=55ns*, the shape of the lower rough surface can be clearly seen.

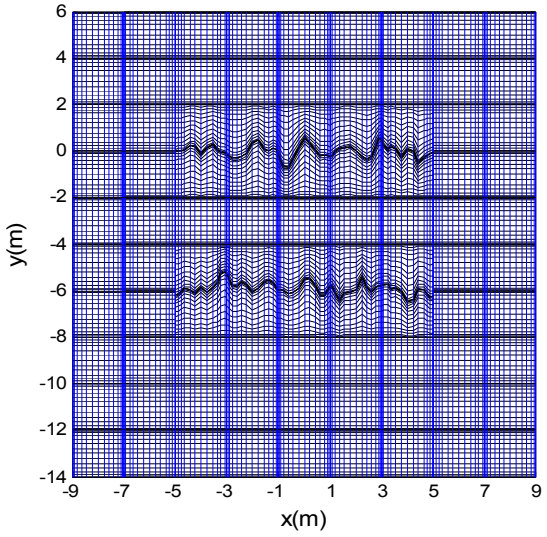

(a)

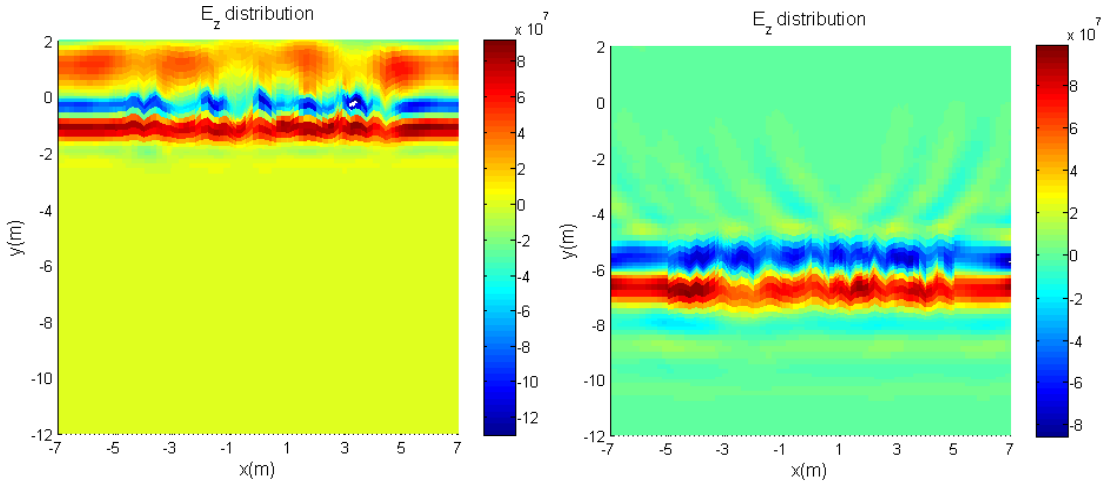

(b) (c)

Fig. 5.8 Scattering from a layered lower half space involving two random rough surfaces of finite length at different moments

(a) Geometry and computation domain,

(b) Spatial distribution of E_z at *t=20ns*, (c) Spatial distribution of E_z at *t=55ns*.

Next, the results of scattering from a cylinder buried in different layers are presented. In the first case, a circular PEC cylinder is placed in the first layer of the lower half space (between the two rough surfaces). The computation domain is given in Fig. 5.9 (a). Numerical results of spatial distribution of E_z obtained at three different moments *t=20ns*, *t=30ns,* and *t=55ns* are shown in Figs. 5.9 (b), (c), and (d). It is of interest to note that the field distribution at *t=20ns* well represents the shape of the rough surface and a small portion of the buried circular cylinder. As the incident wave travel farther in the lower half space, the field distribution at *t=30ns* illustrates the shape of PEC cylinder more clearly in Fig. 5.9 (c). At *t=55ns*, the incident field covers the whole buried cylinder and hence its complete shape is well shown in Fig. 5.9 (d), as expected.

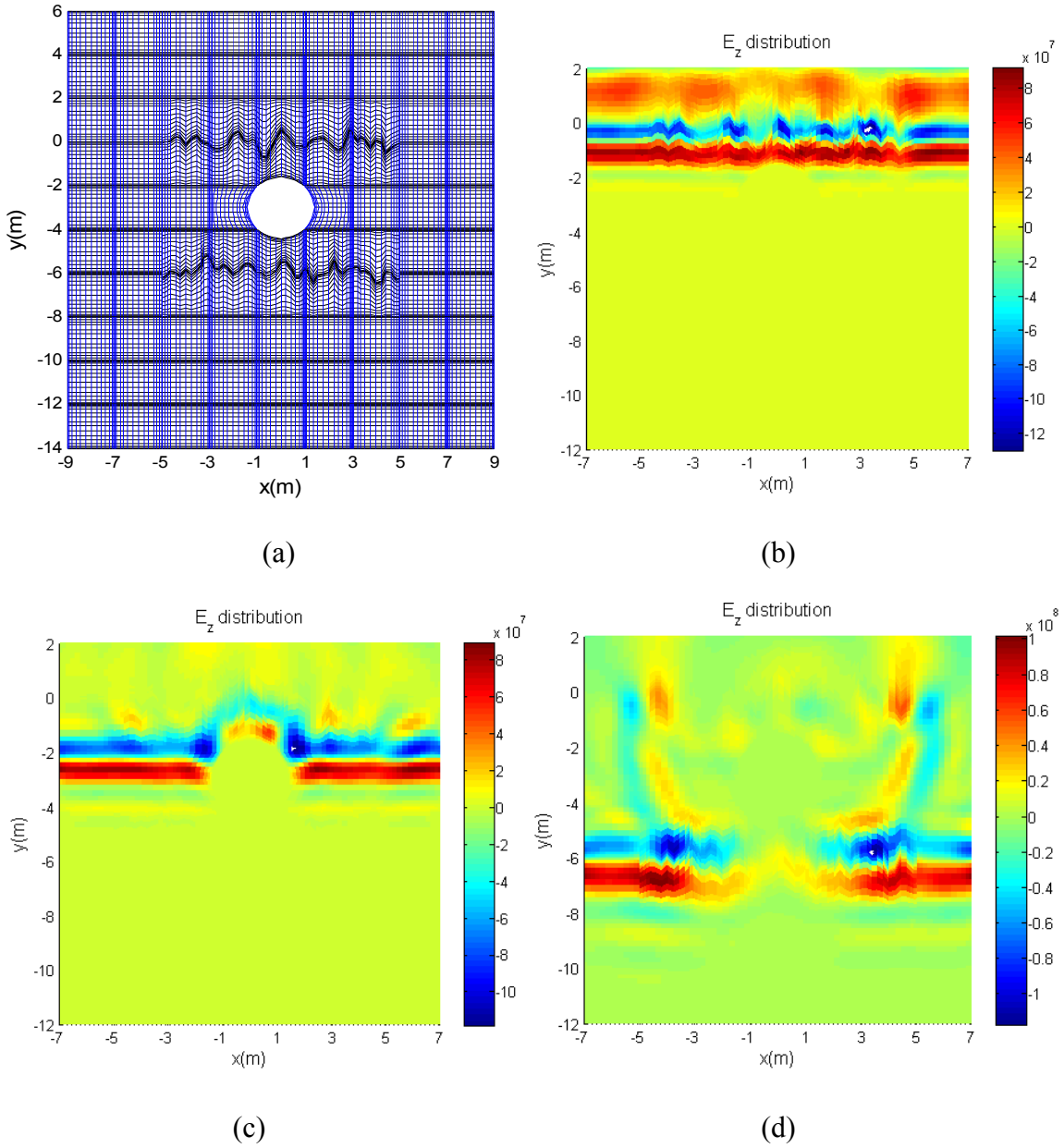

(a) (b)

(c) (d)

Fig. 5.9 Scattering from a circular PEC cylinder embedded in the first layer of the lower half space involving two random rough surfaces of finite length at different moments (a) Geometry and computation domain, (b) Spatial distribution of E_z at $t=20ns$, (c) Spatial distribution of E_z at $t=30ns$, (d) Spatial distribution of E_z at $t=55ns$.

Then, we consider a square PEC cylinder located in the second layer of the lower half space, the computation domain of which is depicted in Fig. 5.10 (a). In Figs. 5.10 (b), (c), and (d), the spatial distribution of E_z at three different moments *t=20ns*, *t=60*ns, and *t=70*ns are presented. It is of interest to note that the field distribution at *t=20ns* shown in Fig. 5.10 (b) is the same as the results given in Fig. 5.8(b), since there is no buried object in the first layer of the lower half space, the scattering at this moment attributes solely to the upper random rough surface. As time progresses, the incident wave propagates farther and illuminates the lower rough surface and the square PEC cylinder. At *t=60*ns, only a small portion of the square PEC cylinder is illustrated by the field distribution. At *t=70ns*, the incident field covers the whole buried cylinder and hence its complete shape is well shown in Fig. 5.10 (d), as expected.

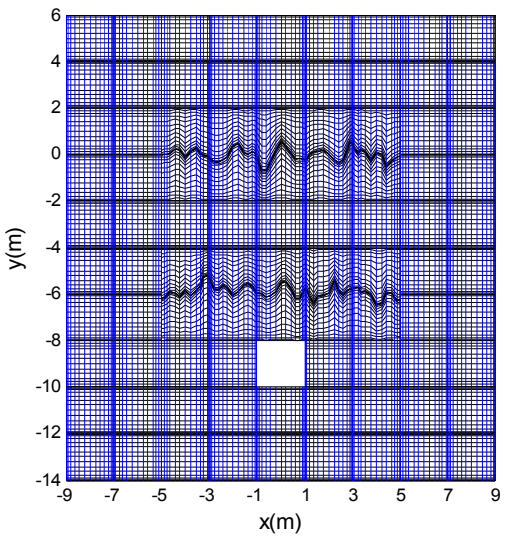

(a)

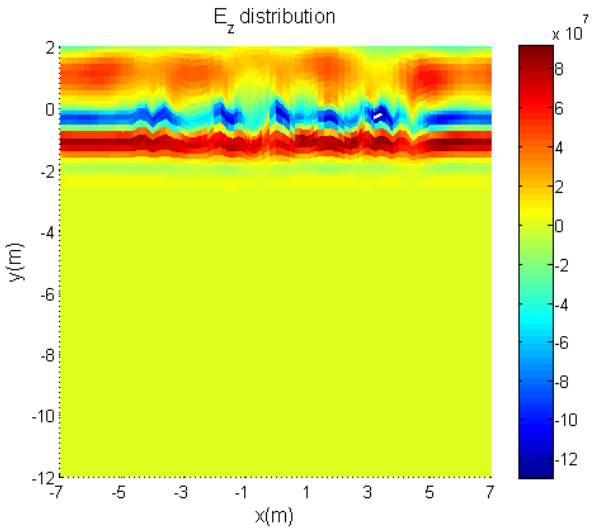

(b)

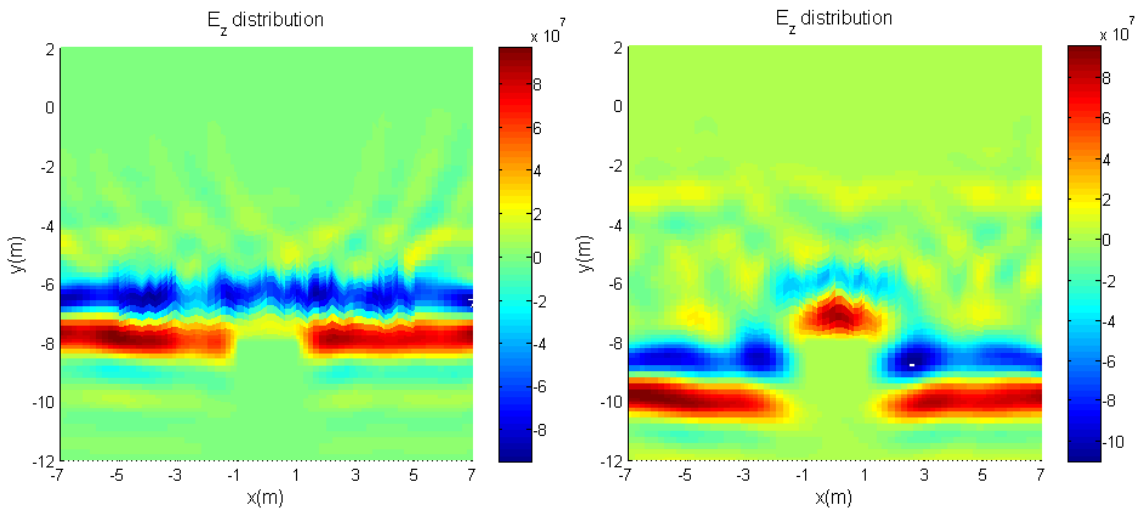

(c) (d)

Fig. 5.10 Scattering from a square PEC cylinder embedded in the second layer of the lower half space involving two random rough surfaces of finite length at different moments

(a) Geometry and computation domain, (b) Spatial distribution of E_z at *t=20ns*, (c) Spatial distribution of E_z at *t=60ns*, (d) Spatial distribution of E_z at *t=70ns*.

In the last example, a circular PEC cylinder and a square PEC cylinder are placed in the first and second layer of the lower half space, respectively. The geometry and computation domain are depicted in Fig. 5.11 (a). In Fig. 5.11(b), the spatial distribution of the electric field at *t=85ns* is illustrated, in which the shapes of these two buried cylinder can be observed clearly, as expected.

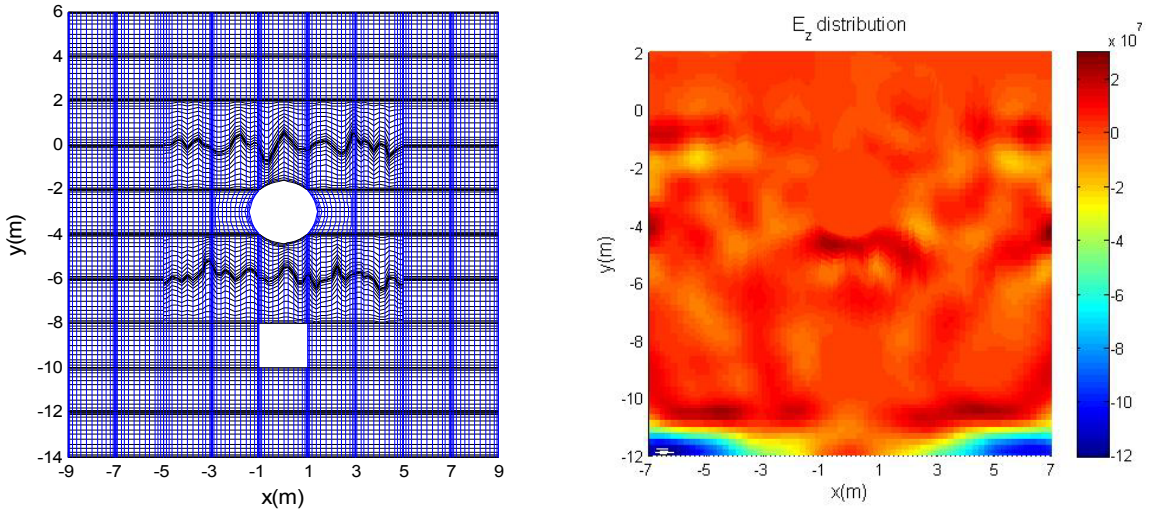

(a) (b)

Fig. 5.11 Scattering from a circular PEC cylinder and a square PEC cylinder embedded in the first and second layer of the lower half space involving two random rough surfaces of finite length at at $t=85ns$

(a) Geometry and computation domain, (b) Spatial distribution of E_z.

CHAPTER SIX

NEAR-ZONE FIELD TO FAR-ZONE FIELD TRANSFORMATION

In the previous chapters, the Monte-Carlo multidomain PSTD (MPSTD) algorithm has been developed to study the near-zone field of the scattering from a cylinder buried below a random rough surface. Based on knowledge of the near-zone field, the far-zone field pattern can be determined, which has many practical applications including remote sensing. In this chapter, a near-field to far-field transformation technique is developed and presented. The equivalence principle is employed first to model a random rough surface of finite length and buried objects in terms of the equivalent electric and magnetic currents. Then, computation of the far-zone field radiated by these equivalent currents is formulated using reciprocity and duality theorem.

6.1 General Idea and Formulation of the Equivalent Model

In Fig. 6.1(a) is shown a two-dimensional object buried below a random rough surface of finite length, separating two semi-infinite homogeneous spaces characterized by (μ_o, ε_o) and $(\mu_o, \varepsilon_{r1}\varepsilon_o)$. To model this structure, first, we introduce a virtual planar surface located at $y = 0$ separating regions *a* and *b,* as illustrated in Fig. 6.1 (b). The inhomogeneity above and below the virtual planar interface caused by the random rough surface can be viewed as additional scatterers, which are bounded by the random rough surface and the virtual planar interface. Now, the problem becomes determination of the scattering from a 2D object buried below a planar interface as well as that from the additional scatteres above/below the planar interface.

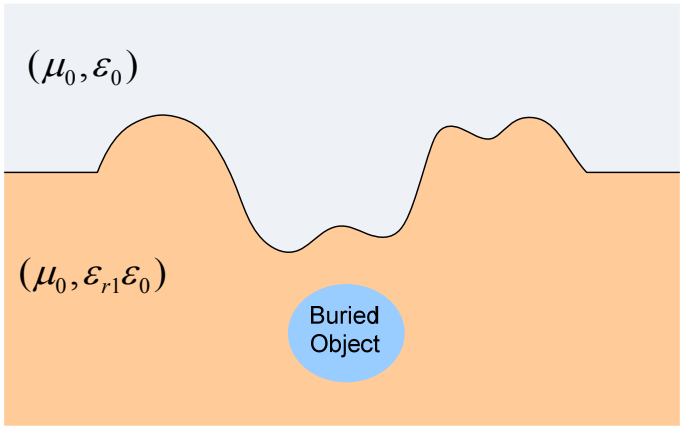

(a)

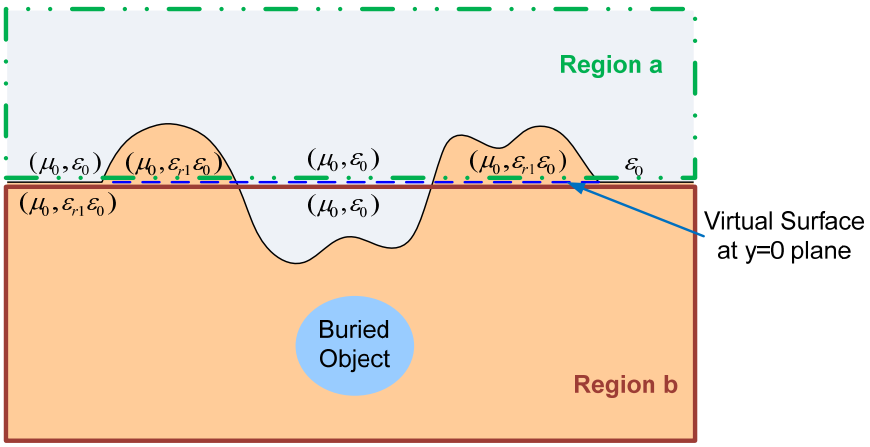

(b)

Fig. 6.1 An object buried below a random rough surface of finite length

(a) Geometry; (b) Illustration of a virtual planar interface.

Then, the equivalence principle [46] is used to construct the equivalent model, shown in Fig. 6.2, in the region external to the buried cylinder and the inhomogeneity caused by the random rough surface. In the equivalent model, the buried cylinder is removed by placing the equivalent electric surface current $\vec{J}_s$ and magnetic surface current $\vec{M}_s$ on its surface. The inhomogeneity enclosed by the random rough surface and

the virtual planar interface, some of them are above and some of them are below the virtual interface, can also be removed by placing the equivalent electric surface current $\vec{J}_{sn}$ and magnetic surface current $\vec{M}_{sn}$ ($n = 1, 2\ldots$) on their boundaries.

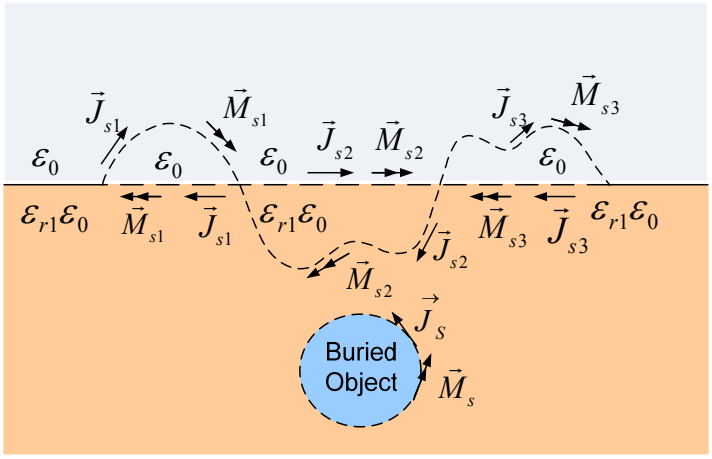

Fig. 6.2 The equivalent model.

Now, in the equivalent model, all the equivalent surface currents radiate in a two-half-space region with a planar interface. The values of $\vec{J}_s$ and $\vec{M}_s$ can be determined by

$$\vec{J}_s = \hat{n} \times \vec{H}, \tag{6.1}$$

$$\vec{M}_s = \vec{E} \times \hat{n}, \tag{6.2}$$

where $\vec{E}$ and $\vec{H}$ are the total fields on the surface of the buried object, calculated by the Monte-Carlo MPSTD approach, and $\hat{n}$ is the outward unit vector normal to its surface. Note that the MPSTD results of the fields are obtained in the time domain, but the far-zone fields will be calculated in the frequency domain. Therefore, the fast Fourier transform (FFT) will be used first to determine the spectrum of the frequency components of the fields. Then, the far-zone field pattern can be determined.

For the TM_z polarization, the electric and magnetic field can be expressed as

$$\vec{E} = E_z \hat{z} \tag{6.3}$$

$$\vec{H} = H_x\hat{x} + H_y\hat{y} \tag{6.4}$$

By substituting (6.3) and (6.4) into (6.1) and (6.2), $\vec{J}_s$ and $\vec{M}_s$ become

$$\vec{J}_s = \hat{n} \times \vec{H} = \hat{n} \times (H_x\hat{x} + H_y\hat{y}) = J_z\hat{z} \tag{6.5}$$

$$\vec{M}_s = \vec{E} \times \hat{n} = E_z\hat{z} \times \hat{n} = M_{sx}\hat{x} + M_{sy}\hat{y} \tag{6.6}$$

where J_z is a z-directed electric line source, M_{sx} and M_{sy} are x- and y-directed magnetic line dipoles.

6.2 Formulation of the Far-Zone Field Equations

The next step is to calculate the far-zone field radiated by these equivalent currents. The equations for the far-zone electric field due to an electric line source have been derived in [65], using reciprocity [46]. Fig. 6.3 depicts a cross-sectional view of a line source near a planar interface separating two half spaces.

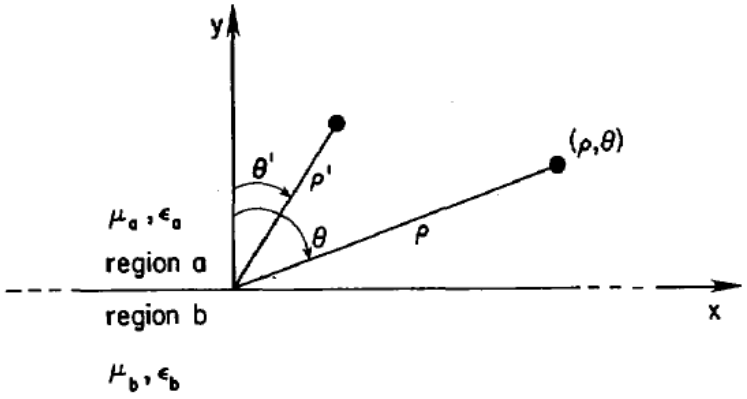

Fig. 6.3 A cross-sectional view of a line source near a planar interface.

The far-zone electric fields observed at $(\rho,\ \theta)$ due to an electric line source of unity strength $\vec{J} = \delta(x - x')\,\delta(y - y')\hat{z}$ at $(\rho',\ \theta')$ are given as the follows. For an electric line source in region a,

$$e_z^{aa}(\rho,\theta) \xrightarrow[|k_a\rho|\to\infty]{} -\frac{k_a\eta_a}{4}\sqrt{\frac{2}{\pi}}e^{j\frac{\pi}{4}}\frac{e^{-jk_a\rho}}{\sqrt{k_a\rho}}e^{jk_ax'\sin\theta}\left\{e^{jk_ay'\cos\theta}+\Gamma_a e^{-jk_ay'\cos\theta}\right\},$$

$$-\frac{\pi}{2}<\theta<\frac{\pi}{2} \qquad (6.7a)$$

$$e_z^{ba}(\rho,\theta) \xrightarrow[|k_b\rho|\to\infty]{} -\frac{k_b\eta_b}{4}\sqrt{\frac{2}{\pi}}e^{j\frac{\pi}{4}}\frac{e^{-jk_b\rho}}{\sqrt{k_b\rho}}\tau_a e^{jk_bx'\sin\theta}e^{-j\sqrt{{k_a}^2-{k_b}^2sin^2\theta}y'}.$$

$$\frac{\pi}{2}<\theta<\frac{3\pi}{2} \qquad (6.7b)$$

And for an electric line source in region b,

$$e_z^{ab}(\rho,\theta) \xrightarrow[|k_a\rho|\to\infty]{} -\frac{k_a\eta_a}{4}\sqrt{\frac{2}{\pi}}e^{j\frac{\pi}{4}}\frac{e^{-jk_a\rho}}{\sqrt{k_a\rho}}\tau_b e^{jk_ax'\sin\theta}e^{j\sqrt{{k_b}^2-{k_a}^2sin^2\theta}y'},$$

$$-\frac{\pi}{2}<\theta<\frac{\pi}{2} \qquad (6.8a)$$

$$e_z^{bb}(\rho,\theta) \xrightarrow[|k_b\rho|\to\infty]{} -\frac{k_b\eta_b}{4}\sqrt{\frac{2}{\pi}}e^{j\frac{\pi}{4}}\frac{e^{-jk_b\rho}}{\sqrt{k_b\rho}}e^{jk_bx'\sin\theta}\left\{e^{jk_by'\cos\theta}+\Gamma_b e^{-jk_by'\cos\theta}\right\}.$$

$$\frac{\pi}{2}<\theta<\frac{3\pi}{2} \qquad (6.8b)$$

In the equations above, the first superscript of e_z indicates the region where the observation point is located, while the second is for the region where the source point is. In these equation, Γ_a and τ_a are defined by

$$\Gamma_a=\frac{\eta_b\cos\theta-\eta_a\cos\theta_a^t}{\eta_b\cos\theta+\eta_a\cos\theta_a^t}, \qquad (6.9a)$$

and

$$\tau_a = 2\frac{\eta_a \cos\theta}{\eta_a \cos\theta - \eta_b \cos\theta_b^t}, \tag{6.9b}$$

in which $\cos\theta_a^t$ is given by

$$\cos\theta_a^t = \sqrt{1 - \frac{\mu_a \varepsilon_a}{\mu_b \varepsilon_b} sin^2\theta} \tag{6.9c}$$

Γ_b and τ_b can be obtained by interchanging *a* and *b* in (6.9a) and (6.9b), and then changing the sign in front of η_a; and $\cos\theta_b^t$ can be found from (6.9c) also by interchanging *a* and *b*. Using these equations, one can determine the far-zone electric fields due to each segment of the equivalent currents J_z on the surface of the buried object as well as that on the surface of the "additional scatterers".

The far-zone electric field radiated by magnetic line dipoles can be derived from [66]. In [66], the expressions of the far-zone magnetic fields due to the horizontal and vertical electric line dipoles are given. By employing duality [46], the far-zone electric field e_z generated by the magnetic line dipoles M_{sx} and M_{sy} of unity strength are obtained as shown below.

For a horizontal unity strength magnetic line dipole M_{sx} in region a,

$$e_h^{aa}(\rho,\theta) \xrightarrow[|k_a\rho|\to\infty]{} -\frac{k_a}{4}\sqrt{\frac{2}{\pi}} e^{j\frac{\pi}{4}} \frac{e^{-jk_a\rho}}{\sqrt{k_a\rho}} \cos\theta\, e^{jk_a x' \sin\theta} \left\{ e^{jk_a y' \cos\theta} - \Gamma_a e^{-jk_a y' \cos\theta} \right\},$$

$$-\frac{\pi}{2} < \theta < \frac{\pi}{2} \tag{6.10a}$$

$$e_h^{ba}(\rho,\theta) \xrightarrow[|k_b\rho|\to\infty]{} \frac{\mu_b}{\mu_a}\frac{k_b}{4}\sqrt{\frac{2}{\pi}} e^{j\frac{\pi}{4}} \frac{e^{-jk_b\rho}}{\sqrt{k_b\rho}} \cos\theta_b^t\, \tau_a e^{jk_b x' \sin\theta} e^{-j\sqrt{k_a{}^2 - k_b{}^2 sin^2\theta}\, y'}.$$

$$\frac{\pi}{2} < \theta < \frac{3\pi}{2} \tag{6.10b}$$

And for a horizontal unity strength magnetic line dipole M_{sx} in region b,

$$e_h^{ba}(\rho,\theta) \xrightarrow[|k_a\rho|\to\infty]{} -\frac{\mu_a}{\mu_b}\frac{k_\mathrm{a}}{4}\sqrt{\frac{2}{\pi}}e^{j\frac{\pi}{4}}\frac{e^{-jk_a\rho}}{\sqrt{k_a\rho}}\cos\theta_\mathrm{a}^\mathrm{t}\,\tau_b e^{jk_a x'\sin\theta}e^{j\sqrt{{k_\mathrm{b}}^2-{k_\mathrm{a}}^2 sin^2\theta}y'},$$

$$-\frac{\pi}{2}<\theta<\frac{\pi}{2} \qquad (6.10c)$$

$$e_h^{bb}(\rho,\theta) \xrightarrow[|k_b\rho|\to\infty]{} -\frac{k_b}{4}\sqrt{\frac{2}{\pi}}e^{j\frac{\pi}{4}}\frac{e^{-jk_b\rho}}{\sqrt{k_b\rho}}\cos\theta\, e^{jk_b x'\sin\theta}\left\{e^{jk_b y'\cos\theta}-\Gamma_b e^{-jk_b y'\cos\theta}\right\}.$$

$$\frac{\pi}{2}<\theta<\frac{3\pi}{2} \qquad (6.10d)$$

For a vertical unity strength magnetic line dipole M_{sy} in region a,

$$e_v^{aa}(\rho,\theta) \xrightarrow[|k_a\rho|\to\infty]{} \frac{k_a}{4}\sqrt{\frac{2}{\pi}}e^{j\frac{\pi}{4}}\frac{e^{-jk_a\rho}}{\sqrt{k_a\rho}}\sin\theta\, e^{jk_a x'\sin\theta}\left\{e^{jk_a y'\cos\theta}+\Gamma_a e^{-jk_a y'\cos\theta}\right\},$$

$$-\frac{\pi}{2}<\theta<\frac{\pi}{2} \qquad (6.11a)$$

$$e_v^{ba}(\rho,\theta) \xrightarrow[|k_b\rho|\to\infty]{} \frac{\mu_b}{\mu_a}\frac{k_\mathrm{b}}{4}\sqrt{\frac{2}{\pi}}e^{j\frac{\pi}{4}}\frac{e^{-jk_b\rho}}{\sqrt{k_b\rho}}\sin\theta\,\tau_a e^{jk_b x'\sin\theta}e^{-j\sqrt{{k_a}^2-{k_b}^2 sin^2\theta}y'}.$$

$$\frac{\pi}{2}<\theta<\frac{3\pi}{2} \qquad (6.11b)$$

And for a vertical unity strength magnetic line dipole M_{sy} in region b,

$$e_v^{ba}(\rho,\theta) \xrightarrow[|k_a\rho|\to\infty]{} \frac{\mu_a}{\mu_b}\frac{k_\mathrm{a}}{4}\sqrt{\frac{2}{\pi}}e^{j\frac{\pi}{4}}\frac{e^{-jk_a\rho}}{\sqrt{k_a\rho}}\sin\theta\,\tau_b e^{jk_a x'\sin\theta}e^{j\sqrt{{k_\mathrm{b}}^2-{k_\mathrm{a}}^2 sin^2\theta}y'},$$

$$-\frac{\pi}{2}<\theta<\frac{\pi}{2} \qquad (6.11c)$$

$$e_v^{bb}(\rho,\theta) \xrightarrow[|k_b\rho|\to\infty]{} \frac{k_b}{4}\sqrt{\frac{2}{\pi}}e^{j\frac{\pi}{4}}\frac{e^{-jk_b\rho}}{\sqrt{k_b\rho}}\sin\theta\, e^{jk_b x'\sin\theta}\left\{e^{jk_b y'\cos\theta}+\Gamma_b e^{-jk_b y'\cos\theta}\right\}.$$

$$\frac{\pi}{2}<\theta<\frac{3\pi}{2} \qquad (6.11d)$$

In (6.10) and (6.11), the subscripts *h* and *v* stand for horizontal and vertical to denote the direction of the line dipoles. In these equations Γ, τ, and $\cos\theta^t$ are given in (6.9).

Using the equivalent surface currents given in equations (6.5) and (6.6) based on knowledge of the near-zone field and equations (6.7) – (6.11) for the far-zone fields due to the equivalent electric line current and magnetic line dipoles of unity strength, the far-zone fields everywhere can be obtained as the superposition of the fields due to the unity-strength surface currents. The superposition can be realized in a similar way as that presented in equation (4) in [66] and equation (11) in [67].

6.3 Numerical Results and Discussion

In this section, the formulation presented in the previous section is implemented into computer codes, and the scattering of a 2D PEC cylinder buried in the lower half space with a planar or random rough surface is considered and sample results of the far-zone field patterns in the upper half space are presented and discussed. For all the numerical results presented, the excitation is taken to be a normal TM_z plane wave incidence propagating in –y direction, the time domain function of which is the first derivative of Blackmann-Harris window function with central frequency $f = 100MHz$. The random rough surface considered is of finite length $L = 10m$ $(3.33\lambda_0)$ and correlation length $l_c = 0.3m$ $(0.1\lambda_0)$, which satisfies the requirement $L \geq 15l_c$. The region

above the rough surface is assumed to be free space and the region below the rough surface is taken to be an isotropic, lossless medium with $\mu_r = 1$ and $\varepsilon_r = 4$, unless otherwise indicated.

(1) Far-Zone Field Pattern Due to the Scattering by a Circular PEC Cylinder Under Planar Interface

To validate the formulation, in the first numerical example, we consider a circular PEC cylinder placed below a planar media interface along y = 0. The geometry of the computation region is shown in Fig. 6.4. The circular cylinder is of radius $r = 0.35\lambda_b$, and is centered by (0, -0.35λ_b).

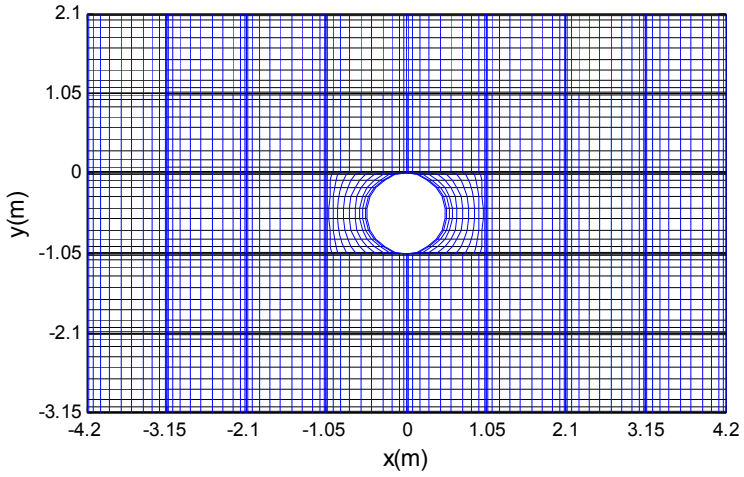

Fig.6.4 Geometry of the computation domain.

The far-zone electric field pattern in the upper half space is illustrated in Fig. 6.5, and is compared with the results obtained from the Method Of Moments (MOM) [68]. As shown in this figure, the two sets of data have a perfect match, which validates the correctness of the formulation derived in the previous section. Note that the field pattern

exhibits symmetry, which is due to the fact that the cylinder is subjected to normally incident illumination.

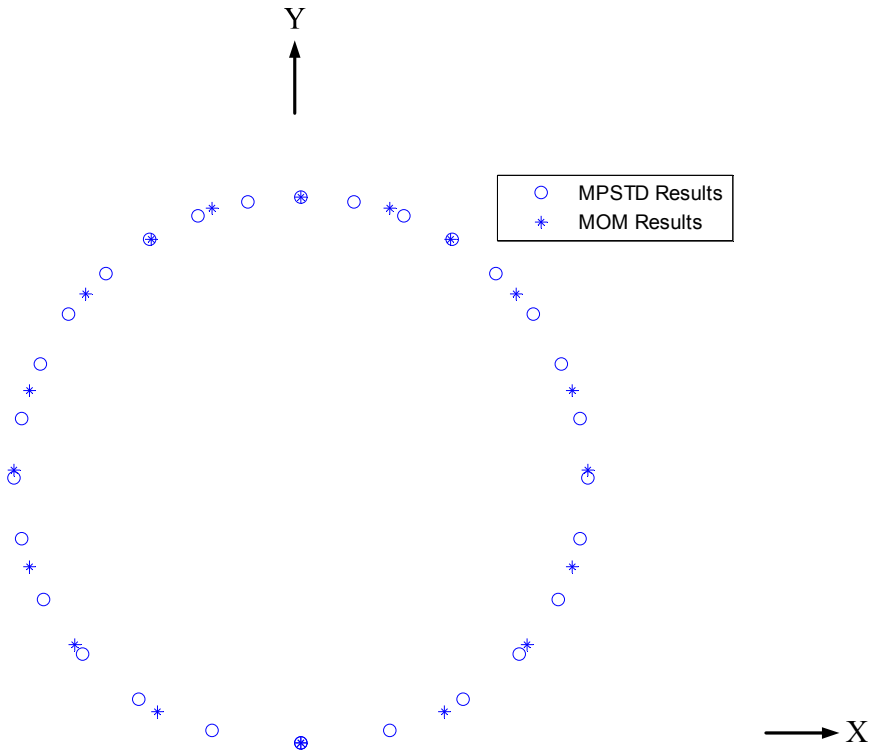

Fig. 6.5 Far-zone electric field pattern in the upper half space for a circular PEC cylinder buried below a planar media interface.

(2) Far-Zone Field Pattern Due to the Scattering by a Circular PEC Cylinder Buried Below a Random Rough Surface of Finite Length

When a random rough surface is included, the computation is carried out tens of times and in each of them, the technique developed earlier in this chapter is employed to obtain the far-zone radiation pattern. Then, the Monte-Carlo statistic average is taken to obtain the final result of the far-zone field pattern. It is noted that the number of average times increases as the height of the random rough surface grows.

In the following numerical examples, a random rough surface of finite length is placed between $-5 \le x \le 5$ along $y = 0$. The geometry of the computation domain is illustrated in Fig. 6.6. The radius of the circular PEC cylinder is $r = \sqrt{2}m$.

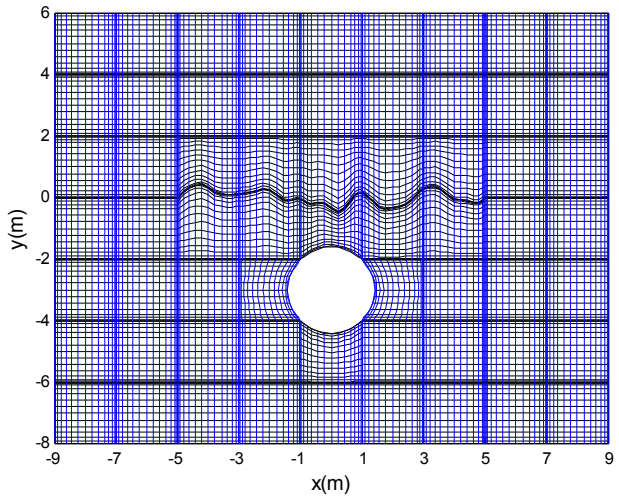

Fig. 6.6 Geometry of the computation domain.

Different from the previous numerical example for a planar media interface, the far-zone field pattern now is contributed by the scattering of both the circular PEC cylinder and the random rough surface, which causes "additional scatterers". The results of the far-zone field pattern scattered by a circular PEC cylinder buried below a random rough surface of different *rms* heights are presented in Fig. 6.7. Under the normal plane wave incidence, the far-zone field patterns are almost symmetric as they should be. One notes that when the random rough surface is of very small *rms* height $h_{rms} = 0.01m$, the field pattern is almost the same as that for a flat surface because the contribution from the random rough surface with such a small *rms* height is negligible . But as the *rms* height increases from 0.01m to 0.05m, 0.1*m* and finally to 0.2m, it can be seen that the field pattern becomes more and more different from that for a flat surface, due to the fact that the rougher random rough surface, which causes larger "additional scatterers" would

contribute more to the field pattern. In particular, one observes that the fields in the vertical direction (y-direction) becomes weaker as the *rms* height increases. This is because for a flat media interface, the waves reflected by the whole interface all propagate in the same direction, the vertical direction. But the waves scattered by different parts of a random rough surface would be in random directions, so that the superposition of the scattering in the vertical direction should be weaker compared with the flat-surface case, and it becomes weaker and weaker as the random rough surface gets rougher. This phenomenon is similar to the behavior of the near-zone field results presented in the previous chapters showing that the roughness of the random rough surface has a significant influence on the scattering of the buried object.

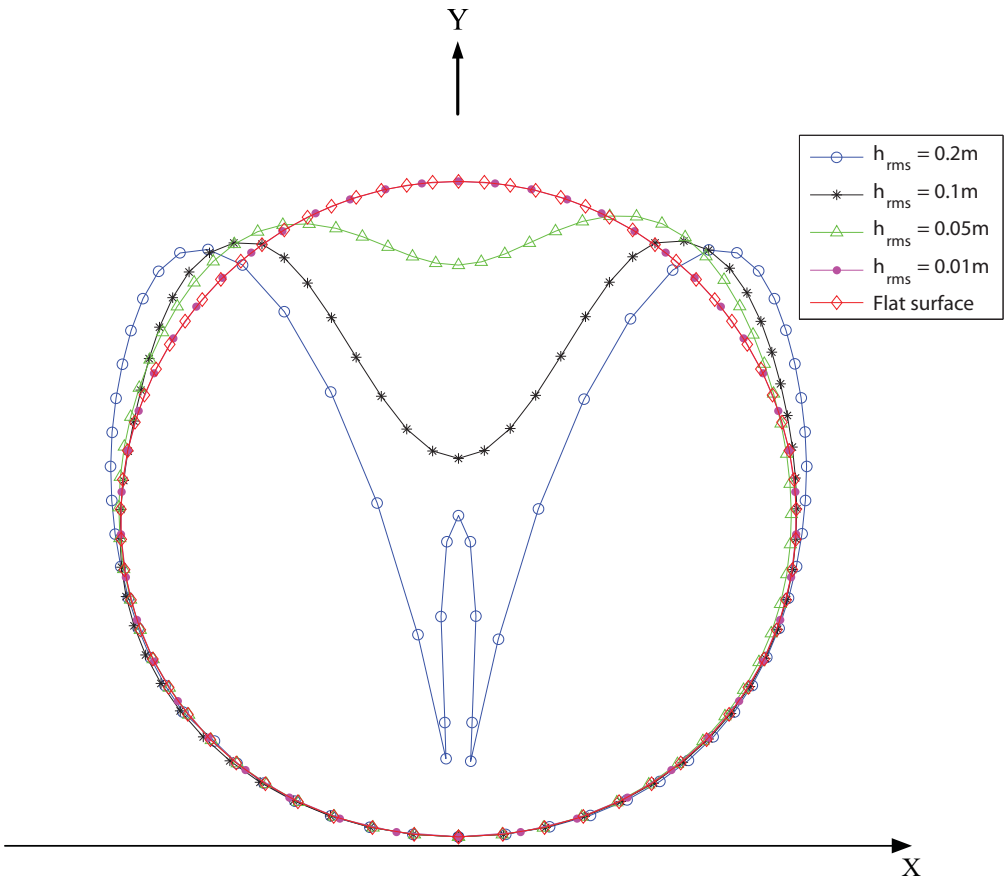

Fig.6.7 Far-zone field patterns in the upper half space scattered by a circular PEC cylinder buried below a random rough surface of different *rms* heights.

In the last example, the far-zone field patterns for various lower half space relative permittivity ε_{r2} are presented. The geometry remains the same as the previous example. The roughness of the surface is chosen to be $0.2m$. From the data presented in Fig. 6.8, one notes that as ε_{r2} changes from 4, to 2, to 1.01 and finally to 1, the results gradually reduce to that for the circular PEC cylinder located in free space, as expected.

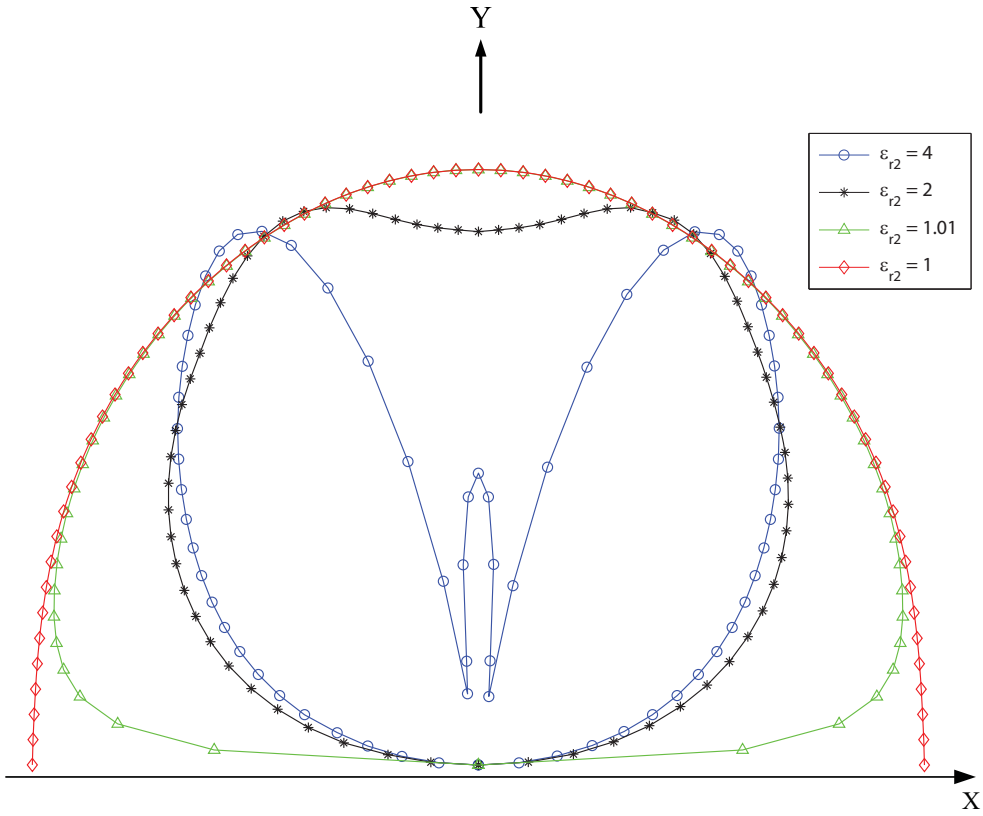

Fig. 6.8 Far-zone field patterns in the upper half space scattered by a circular PEC cylinder buried below a random rough surface for various ε_{r2}.

References

1. D. Holliday *et al.*, "Forward backward: A new method for computing low grazing angle scattering," *IEEE Trans. Antennas Propag.*, vol. 44, no. 2, pp. 722–729, 1996.

2. M. R. Pino, L. Landesa, J. L. Rodriguez, F. Obelleiro, and R. J. Burkholder, "The generalized forward-backward method for analyzing the scattering from targets on ocean-like rough surfaces," *IEEE Trans. Antennas Propag.*, vol. 47, no. 6, pp. 961–969, 1999.

3. Y. Q. Jin and Z. Li, "Numerical simulation of radar surveillance for the ship target and oceanic clutters in two-dimensional model," *Radio Sci.*, vol. 38, no. 3, pp. 1045–1050, 2003.

4. Z. Li and Y. Q. Jin, "Bistatic scattering and transmitting through a Fractal rough surface with high permittivity using the PBTGFBM/SAA method," *IEEE Trans. Antennas Propag.*, vol. 50, no. 9, pp. 1323–1326, 2002.

5. P. Liu and Y. Q. Jin, "Numerical simulation of the Doppler spectrum of a flying target above dynamic oceanic surface by using the FEM-DDM method," *IEEE Trans. Antennas Propag.*, vol. 53, no. 2, pp. 825–832, 2005.

6. P. Liu and Y. Q. Jin, "Numerical simulation of bistatic scattering from a target at low altitude above rough sea surface under an EM wave incidence at low grazing angle by using the finite element method," *IEEE Trans. Antennas Propag.*, vol. 52, no. 5, pp. 1205–1210, 2004.

7. G. Zhang, L. Tsang, and K. Pak, "Angular correlation function and scattering coefficient of electromagnetic waves scattering by a buried object under a two-dimensional rough surface," *Journal of Optical Society America, A*, vol. 15, no. 12, pp. 2995-3002, Dec. 1998.

8. J.T. Johnson and R.J. Burkholder, "Coupled canonical grid/discrete dipole approach for computing scattering from objects above or below a rough interface," *IEEE Transactions on Geoscience and Remote Sensing*, vol. 39, pp. 1214-1220, June 2001.

9. J.T. Johnson, "A numerical study of scattering from an object above a rough surface," *IEEE Transactions on Antennas and Propagation,* vol. 48, pp. 1361-1367, Oct. 2002.

10. C.-H Kuo and M. Moghaddam, "Electromagnetic scattering from a buried cylinder in layered media with rough interfaces," *IEEE Transactions on Antennas and Propagation*, vol. 54, no. 8, pp. 2392 – 2401, August 2006.

11. M. El-Shenawee, C. Rappaport, E. Miller, and M. Silevitch, "3-D subsurface analysis of electromagnetic scattering from penetrable/PEC objects buried under rough surface: use of the steepest descent fast multipole method (SDFMM)", *IEEE Transactions on Geoscience and Remote Sensing*, vol. 39, pp. 1174-1182, June 2001.

12. M. El-Shenawee, C. Rappaport, and M. Silevitch, "Mote Carlo simulations of electromagnetic scattering from random rough surface with 3-D penetrable buried objects: mine detection application using the SDFMN", *Journal of Optical Society America, A*, Dec. 2001.

13. M. El-Shenawee, "Scattering from multiple objects buried beneath two-dimensional random rough surface using the steepest decent fast multipole method," *IEEE Transactions on Antennas and Propagation*, vol. 51, no. 4, pp. 802-809, April 2003.

14. M. EL-Shenawee, "Polarimetric scattering from two-layered two-dimensional random rough surfaces with and without buried objects," *IEEE Transactions on Geosciences and remote sensing*, vol. 42, no. 1, pp. 67 – 76, January 2004.

15. F.D. Hastings, J.B. Schneider, and S.L. Broschat, "A Monte-Carlo FDTD technique for rough surface scattering," *IEEE Transactions on Antennas and Propagation*, vol. 43, no. 11, pp. 1183-1191, November 1995.

16. L. Kuang and Y-Q Jin, "Bistatic scattering from a three-dimensional object over a randomly rough surface using the FDTD algorithm," *IEEE Transactions on Antennas and Propagation*, vol. 55, no. 8, pp. 2302-2312, August 2007.

17. J. Li, L. X. Guo, and H. Zeng, "FDTD investigation on electromagnetic scattering from the PEC cylinder above two-layered rough surfaces," *Proc. International Conference on Microwave and Millimeter Wave Technology*, vol. 2, pp. 531-534, Apr. 2008.

18. K.H. Dridi, J.S. Hesthaven, and A. Ditkowski, "Staircase-Free finite-difference time-domain formulation for general materials in complex geometries," *IEEE Transactions on Antennas and Propagation*, vol. 49, no. 5, pp.749 – 756, May 2001.

19. G.X. Fan, Q. H. Liu, and J. S. Hesthaven, "Multidomain pseudospectral time-domain simulations of scattering by objects buried in lossy media," *IEEE Transactions on Geoscience and Remote sensing*, vol. 40, no. 6, pp. 1366 - 1373, June 2002.

20. A. Taflove and S.C. Hagness, Computational Electrodynamics The Finite-Difference Time-Domain Method, Third Edition, Chapter 17 Advances in PSTD Techniques, by Q. H. Liu and G. Zhao, 2005 Artech House, Inc., Norwood, MA.

21. B. Yang, D. Gottlieb, and J.S. Hesthaven, "Spectral simulation of electromagnetic wave scattering," *Journal of Computational Physics*, vol. 134, pp. 216 -230, 1997.

22. B. Yang and J.S. Hesthaven, "A pseudospectral method for time-domain computation of electromagnetic scattering by bodies of revolution," *IEEE Transactions on Antennas and Propagation*, vol. 47, no. 1, pp. 132 – 141, January 1999.

23. G. Zhao and Q.H. Liu, "The 2.5-D multidomain pseudospectral time-domain algorithm," *IEEE Transactions on Antennas and Propagation*, vol. 51, no. 3, pp. 619 – 627, March 2003.

24. G. Zhao and Q.H. Liu, "The 3-D multidomain pseudospectral time-domain algorithm for inhomogeneous conductive media," *2003 IEEE International Antennas and Propagation Symposium,* Volume 2, 2003 Digest, pp. 559-562, June 22-27, 2003.

25. Y. Shi and C.-H. Liang, "A strongly well-posed PML with unsplit-field formulations in cylindrical and spherical coordinates," *Journal of Electromagnetic Waves and Applications*, vol. 19, no. 13, pp. 1761 – 1776, 2005.

26. Y. Shi and C.-H. Liang, "Two dimensional multidomain pseudospectral time-domain algorithm based on alternating-direction implicit method," *IEEE Transactions on Antennas and Propagation*, vol. 54, no. 4, pp. 1207 - 1214, April 2006.

27. Y. Shi and C.-H. Liang, "Multidomain pseudospectral time domain algorithm using a symplectic integrator," *IEEE Transactions on Antennas and Propagation*, vol. 55, no. 2, pp. 433 - 439, February 2007.

28. Y. Shi and C.-H. Liang, "Characteristic variables patching conditions in multidomain pseudospectral time domain," *IEEE Antennas and Wireless Propagation Letters*, vol. 6, pp. 353 - 356, 2007.

29. Q.H. Liu, "The PSTD algorithm: a time-domain method requiring only two cells per wavelength," *Microwave and Optical Technology Letters,* vol. 15, no. 3, pp. 158 – 165, June 20, 1997.

30. W.J. Gordan and C.A. Hall, "Transfinite element method: blending-function interpolation over arbitrary curved element domains", *Numerical Math*, vol. 21, pp. 109-129, 1973.

31. S.P. Walker and Markku J. Vartiainen, "Hybridzation of curvlinear time-domain integral equation and time-domain optical methods of electromagnetic scattering analysis', *IEEE Transactions on Antennas and Propagation*, vol. 46, no. 3, pp. 318 - 324, March 1998.

32. J.S. Hesthaven, "High-Order accurate methods in time-domain computational electromagnetic: a review," *Advances in Imaging and Electron Physics*, Vol. 127, pp. 59-117, 2003.

33. J.P. Berenger, "A perfectly matched layer for the absorption of electromagnetic waves," *Journal of Computational Physics*, Vol. 114, pp. 185-200, 1994.

34. W. C. Chew and W.H. Weedon, "A 3D perfectly matched medium from modified Maxwell's equation with stretched coordinates," *Microwave and Optical Technology Letters*, Vol. 7, No. 3, pp. 599-604, 1994.

35. Q.H. Liu, "An FDTD Algorithm with perfectly matched layers for conductive media," *Microwave and Optical Technology Letters*, Vol. 14, No. 2, pp. 134-137, 1997.

36. G. -X. Fan and Q.H. Liu, "A well-posed PML absorbing boundary condition for lossy media," *Proceedings of IEEE Antennas and Propagation Society International Symposium*, Vol. 3, pp. 2-5, 2001.

37. G. -X. Fan and Q.H. Liu, "A strongly well-posed PML in lossy media," *IEEE Antennas and Wireless Propagation Letters*, Vol. 2, pp. 97-100, 2003.

38. X. Gao, M.S. Mirotznik, and D.W. Prather, "A method for introducing soft sources in the PSTD algorithm," *IEEE Transactions on Antennas and Propagation*, Vol. 52, No. 7, pp. 1665-1671, July 2004.

39. Q. Li, Y. Chen, and D. Ge, "Comparison study of the PSTD and FDTD methods for scattering analysis," *Microwave and Optical Technology Letters*, Vol. 25, No. 3, pp. 220-226, May 5 2000.

40. X. Liu and Y. Chen, "Applications of transformed-space non-uniform PSTD (TSNU-PSTD) in scattering analysis without the use of the non-uniform FFT," *Microwave and Optical Technology Letters,* Vol. 38, No. 1, pp. 16-21, July 5 2003.

41. M.H. Carpenter and C.A. Kennedy, "Fourth order 2N-storage Runge-Kutta schemes," *NASA Technical Memorandum 109112*, 1994.

42. D.W. Zingg and T.T. Chrisholm, "Runge-Kutta methods for linear orfinary differential equations," *Applied Numerical Mathematics*, Vol. 31, Issue 2, pp. 227-238, October 1999.

43. J.S. Heathaven, P.G. Dinesen, and J.P. Lynov, "Spectral collocation time-domain modeling of diffractive optial elements," *Journal or Computational Physics*, Vol. 155, pp. 287-306, 1999.

44. H. Vandeven, "Family of spectral filters for discontinuous problems," *Journal of Scientific Computing*, Vol. 6, No. 2, pp. 159 – 192, 1991.

45. Q. Cao, F. Zhao, and L. Li, "Applications of the multidomain pseudospectral time-domain algorithm for waveguide structures," *IET Microwaves, Antennas & propagation*, Vol. 4, Issue 10, pp. 1626 – 1631, 2010.

46. R. F. Harrington, Time-Harmonic Electromagnetic Fields, IEEE Press, 2001.

47. A Papoulis, Probability, Random Variables, and Stochastic Processes, Second Edition, McGraw-Hill Book Company, New Youk, 1984.

48. L. Tsang, J.A. Kong, K.H. Ding, and C.O. Ao, Scattering of Electromagnetic Waves, (Volume II) Numerical Simulations, John Wiley & Sons Inc. New York, 2001.

49. P. Bill Wong, G. Leonard Tyler, and John E. Baron etc., "A three-wave FDTD approach to surface scattering with application to remote sensing of geophysical surfaces," *IEEE Transactions on Antennas and Propagation*, Vol. 44, No. 4, pp. 504-514, April 1996.

50. Yun Yi, Bin Chen, Da-Gang Fang and Bi-Hua Zhou, "A new 2-D FDTD method applied to scattering by infinite object with oblique incidence," *IEEE Transactions on Electromagnetic Compatibility*, Vol. 47, No. 4, pp. 756-762, November 2005.

51. Xianyang Zhu, Lawrence Carin, "Multiresolution time-domain analysis of plane-wave scattering from general three-dimensional surface and subsurface dielectric targets," *IEEE Transactions on Antennas and Propagation,* Vol. 49, No. 11, pp. 1568-1578, November 2001.

52. M. N. O. Sadiku, Numerical Techniques in Electromagnetics, CRC Press, 1992.

53. H. Ye and Y.Q. Jin, "Parameterization of the tapered incident wave for numerical simulation of electromagnetic scattering from rough surface," *IEEE Transactions on Antennas and Propagation*, Vol. 53, No. 3, pp. 1234-1237, March 2005.

54. C. H. Chan, S.H. Lou, L. Tsang and J.A. Kong, "Electromagnetic scattering of waves by random rough surface: a finite-difference time-domain approach," *Microwave and Optical Technology Letters*, Vol. 4, No. 9, pp. 355-359, August 1991.

55. M. E. Veysoglu, R.T. Shin and J.A. Kong, "A finite-difference time-domain analysis of wave scattering from periodic surface: oblique incidence case," *Journal of Electromagnetic Waves and Applications*, vol. 7, no. 12, pp. 1595-1607, 1993.

56. W. J. Tsay and David M. Pozar, "Application of the FDTD technique to periodic problems in scattering and radiation," *IEEE Microwave and Guided Wave Letters*, Vol. 3, No. 8, pp. 250-252, August 1993.

57. F. Yang, J. Chen, R. Qiang and Atef Elsherbeni, "FDTD analysis of periodic structures at arbitrary angles: a simple and efficient implementation of the periodic boundary conditions," *Proceedings of IEEE Antennas and Propagation Society International Symposium*, pp. 2715-2718, 2006.

58. P.B. Wong, G. L. Tyler, J.E. Baron, E.M. Gurrola, and R.A. Simpson, "A three-wave FDTD approach to surface scattering with applications to remote sensing of geophysical surfaces," *IEEE Transactions on Antennas and Propagation*, Vol. 44, No. 4, pp. 504-514, April 1996.

59. X. Zhu and L. Carin, "Multiresolution time-domain analysis of plane-wave scattering from general three-dimensional surface and subsurface dielectric targets," *IEEE Transactions on Antennas and Propagation*, Vol. 48, No. 11, pp. 1568-1578, November 2001.

60. Y. Yi, B. Chen, D.-G. Fang, and B.-H. Zhou, "A new 2-D FDTD method applied to scattering by infinite objects with oblique incidence," *IEEE Transactions on Electromagnetic Compatibility*, Vol. 47, No. 4, pp. 756-762, November 2005.

61. W. Liu, Y. Dai, H. Yang, and X.-B. Xu, "Scattering of object buried below random rough surface --- a Monte-Carlo pseudospectral time-domain approach," *Electromagnetics*, Vol. 32, Issue 6, pp. 330-344, August, 2012.

62. R.W. Scharstein, "Transient electromagnetic plane wave reflection from a dielectric slab," *IEEE Transactions on Education*, Vol.35, No.2, pp. 170-175, May 1992.

63. Z. Huang, "A numerical ground-penetrating radar simulator," PH.D. dissertation, The University of Kansas.

64. David M. Pozar, "Microwave Engineering", John Wiley & Sons Inc. New York, 1998.

65. C. M. Butler and X.-B. Xu, "A simple method for determining the far-zone field due to line sources near media surface," *Dig. USNC/URSI Nat. Radio Sci. Meet.*, Boulder, CO, pp. 69, Jan. 1987.

66. C. M. Butler and X.-B. Xu, "TE scattering by partially buried and coupled cylinders at the interface between two media," *IEEE Transactions on Antennas and Propagation,* Vol. 38, No. 11, pp. 1829-1834, November 1990.

67. X.-B. Xu and C. M. Butler, "Scattering of TM excitation by coupled and partially buried cylinders at the interface between two media," *IEEE Transactions on Antennas and Propagation,* Vol. AP-35, No. 5, pp. 529-538, May 1987.

68. X.-B. Xu, "Analysis of TM- and TE-excited cylinders in a region comprising two semi-infinite half spaces separated by a planar interface," Ph.D. Dissertation, University of Mississippi, 1985.